Photoemission spectra of nanostructured solar cell interfaces from first principles

Christopher E. Patrick

Hertford College, University of Oxford

A thesis submitted for the Degree of
Doctor of Philosophy in Materials

Trinity Term 2013

Contents

Contents i

Abstract vii

1 Introduction 1
- 1.1 Solar Photovoltaics . . . 1
  - 1.1.1 Renewables and the global energy demand . . . 1
  - 1.1.2 Principles of solar PV . . . 3
  - 1.1.3 Characterising solar cells . . . 4
  - 1.1.4 Cost vs. efficiency . . . 5
  - 1.1.5 Length-scales in molecular devices . . . 6
- 1.2 Dye-sensitized solar cells . . . 7
  - 1.2.1 Operating principle of the DSC . . . 7
  - 1.2.2 Device optimisation . . . 8
  - 1.2.3 Basic materials . . . 9
  - 1.2.4 The N3/TiO_2 interface . . . 12
- 1.3 Characterisation of interfaces through PES . . . 13
  - 1.3.1 Basic principles . . . 13
  - 1.3.2 Calculating the photocurrent . . . 15
  - 1.3.3 Valence and core-level photoemission . . . 15
- 1.4 Outline and organization of the thesis . . . 16

2 Electronic structure in DFT 19
- 2.1 Density-functional theory . . . 20
  - 2.1.1 The electronic equation . . . 20
  - 2.1.2 Hohenberg-Kohn/Kohn-Sham description . . . 21
  - 2.1.3 The exchange-correlation potential . . . 22
  - 2.1.4 The LDA and the exchange-correlation hole . . . 23
- 2.2 Practical calculations . . . 25
  - 2.2.1 Pseudopotentials . . . 25
  - 2.2.2 Basis sets . . . 27
  - 2.2.3 Coulomb interactions in periodic boundary conditions . . . 29
- 2.3 First-principles molecular dynamics . . . 32

2.3.1 Forces and Born-Oppenheimer molecular dynamics 32
2.3.2 Car-Parrinello MD 33
2.3.3 Temperature control with thermostats 35
2.4 Correlated electrons: LDA + Hubbard U 36
2.4.1 The LDA and fractional occupations 36
2.4.2 Introducing U corrections 37
2.4.3 DFT+U kept simple 38
2.5 Excitations in DFT 40
2.5.1 The ΔSCF method 40
2.5.2 Benchmarking ΔSCF for ionisation potentials 41
2.5.3 ΔSCF and core-level shifts 42
2.5.4 Practical calculation of core-level shifts 43
2.5.5 ΔSCF and the derivative discontinuity 48
2.6 Conclusions 50

3 Electronic structure of excited states in the GW approach 53
3.1 Green's functions 55
3.1.1 Definition of the Green's function 55
3.1.2 Energy structure of the Green's function 56
3.1.3 The non-interacting Green's function 59
3.1.4 Equation of motion 60
3.1.5 Introducing the self-energy 62
3.2 The quasiparticle equation 63
3.2.1 Energy-space representation 63
3.2.2 Matrix element representation 65
3.3 Constructing the self-energy 67
3.3.1 The dielectric function and screened Coulomb interaction . 67
3.3.2 Hedin's equations 68
3.3.3 The GW approximation 69
3.4 The G_0W_0 method 70
3.4.1 Reciprocal space and matrix element representations of Hedin's equations 70
3.4.2 Σ_X and Σ_C 72
3.4.3 Plasmon pole models 73
3.4.4 Obtaining quasiparticle energies 76
3.4.5 Technical limitations: empty states and plane-wave cutoffs 76
3.5 Photoemission 77
3.5.1 The spectral function 78
3.5.2 The spectral function in the diagonal approximation 79
3.5.3 Expression for photoemission 80
3.5.4 Extrinsic losses 81
3.6 Conclusions 82

4 The structure of TiO_2, the N3 dye and the N3/TiO_2 interface 85
4.1 Titanium dioxide . . . 86
4.1.1 Crystal structure . . . 86
4.1.2 Calculation of structural parameters . . . 87
4.1.3 Modelling mesoporous films . . . 88
4.1.4 Details of the anatase (1 0 1) slab . . . 90
4.2 The N3 dye . . . 91
4.2.1 Molecular structure . . . 91
4.2.2 Calculation of structural parameters . . . 92
4.3 Adsorption models of isolated N3 dyes on the anatase (101) surface 93
4.3.1 Computational details . . . 94
4.3.2 The adsorption energy . . . 94
4.3.3 Carboxylates on metal surfaces . . . 95
4.3.4 Interface models—description of structure . . . 96
4.3.5 Interface models—adsorption energies . . . 99
4.4 O 1*s* core-level shifts at the N3/TiO_2 interface . . . 100
4.4.1 Experimental data—general overview . . . 100
4.4.2 Previous assignment of the O 1*s* spectrum . . . 102
4.4.3 Calculation of O 1*s* spectra—general principles . . . 103
4.4.4 O 1*s* spectra of interface models . . . 105
4.4.5 Conclusions from calculations on single-molecule interface models . . . 108
4.5 Beyond single-molecule interface modules . . . 110
4.5.1 External contaminants . . . 110
4.5.2 Intermolecular H-bonding . . . 111
4.5.3 Long-range intermolecular interactions . . . 113
4.5.4 Escape depth effects . . . 115
4.5.5 H-bonding and exchange-correlation functionals . . . 116
4.6 Conclusions . . . 118

5 Electronic properties of bulk TiO_2 and the N3 molecule 121
5.1 The electronic structure of anatase in DFT . . . 122
5.1.1 Introduction and computational approach . . . 122
5.1.2 Band structure and partial density-of-states . . . 122
5.2 *GW* corrections to the DFT bandstructure . . . 124
5.2.1 Computational methodology . . . 124
5.2.2 Quasiparticle corrections in the G_0W_0 approximation . . . 125
5.2.3 Convergence behaviour . . . 126
5.2.4 Comparison to previous calculations and experiment . . . 127
5.3 Inclusion of Hubbard U corrections; *GWU* . . . 129
5.3.1 Introduction to the procedure . . . 129
5.3.2 GWU . . . 130
5.3.3 Electronic structure at the optimum U . . . 131

5.3.4 Convergence of quasiparticle corrections in GWU 133
5.3.5 Summary for TiO_2 134
5.4 Electronic structure of N3 135
5.4.1 DFT 135
5.4.2 ΔSCF 136
5.4.3 The importance of the Coulomb truncation 137
5.5 Conclusions 139

6 Energy-level alignment at the N3/TiO_2 interface 141
6.1 Photoemission spectroscopy at the N3/TiO_2 interface—basic considerations 142
6.1.1 Experimental measurements 142
6.1.2 The simplest approximation to the photocurrent 143
6.1.3 Valence photoemission spectra in DFT and DFT+U . . . 143
6.2 Theory of PES at molecule/semiconductor interfaces 146
6.2.1 Practical considerations 146
6.2.2 Partitioning the photocurrent 147
6.2.3 Calculating the HOMO/VBT offset 150
6.3 Image-charge corrections 151
6.3.1 Classical description 151
6.3.2 ΔSCF and the image-charge effect 152
6.3.3 The nanocluster model 152
6.3.4 Electronic structure of the bare nanocluster 154
6.3.5 ΔSCF ionisation potential of the nanocluster model 154
6.3.6 Screening charge 155
6.3.7 Comparison with the classical model 157
6.4 Finite slab correction 157
6.4.1 Choosing a reference level 157
6.4.2 The 12-layer anatase slab 159
6.4.3 The slab correction for interface models 160
6.5 Δ_{int} for I2b 162
6.6 Broadening of the photoemission spectrum 162
6.6.1 Thermal motion 163
6.6.2 Configurational disorder 165
6.7 Relative intensities 166
6.8 The quasiparticle spectrum 168
6.8.1 Computational details 168
6.8.2 Comparison with experiment 168
6.9 Conclusions 170

7 Core-level shifts beyond N3/TiO_2 173
7.1 The clean anatase (101) slab . . . 174
7.1.1 O 1*s* binding energies . . . 175
7.1.2 The infinite slab . . . 176
7.2 Obtaining the bulk peak in the presence of adsorbates . . . 178
7.3 The adsorption of water on anatase (1 0 1) . . . 180
7.3.1 Introduction . . . 180
7.3.2 Constructing interface models . . . 181
7.3.3 Geometries and energetics of interface models . . . 182
7.3.4 Calculation of O 1*s* spectra . . . 183
7.3.5 Calculated stabilities vs. spectroscopy . . . 186
7.4 Bi-isonicotinic acid on anatase (1 0 1) . . . 187
7.4.1 Introduction . . . 187
7.4.2 Construction of interface models . . . 188
7.4.3 Energetics of interface models . . . 189
7.4.4 O 1*s* spectra of interface models . . . 189
7.4.5 BINA on TiO_2—outlook . . . 191
7.5 Conclusions . . . 191

8 Semiconductor-sensitized solar cells 193
8.1 Introduction . . . 194
8.2 Atomistic and electronic structure of bulk stibnite . . . 195
8.2.1 The X_2Y_3 compounds . . . 195
8.2.2 Electronic structure . . . 196
8.3 Interface model of the Sb_2S_3/TiO_2 interface . . . 197
8.3.1 Constructing an interface model . . . 197
8.3.2 Relaxing the structure . . . 199
8.3.3 Adsorption energetics . . . 200
8.4 Electronic structure of the interface . . . 201
8.4.1 Local and projected densities-of-states . . . 201
8.4.2 Structure of KS orbitals . . . 203
8.4.3 Energy-level alignment . . . 204
8.5 Extending to other X_2Y_3 sensitizers . . . 205
8.5.1 Introduction . . . 205
8.5.2 Relaxing new interface models . . . 205
8.5.3 Electronic structure and energy-level alignments . . . 206
8.5.4 Device performance—open-circuit voltage . . . 206
8.5.5 Comparison to experiment . . . 207
8.6 Conclusions and outlook . . . 208

9 Conclusions **211**
9.1 General overview 211
9.2 Core-level PES and atomistic structure 212
9.3 Valence PES and electronic structure 213
9.4 Beyond dye-sensitized solar cells 214

Bibliography **217**

Acknowledgements **I**

List of papers **III**

Abstract

Photoemission spectra of nanostructured solar cell interfaces from first principles

Christopher E. Patrick, Hertford College

A thesis submitted for the Degree of Doctor of Philosophy in Materials, Trinity Term 2013

Photovoltaic (PV) technologies could provide abundant, clean and secure energy through the conversion of sunlight into electricity, but currently are too expensive to compete with conventional sources of power. Novel PV devices incorporating nanostructured materials, such as the dye-sensitized solar cell (DSC), have been identified as viable, low-cost alternatives to traditional solar cell designs. In spite of technological progress in the field over the last twenty years, the underlying physics governing DSC operation is still not well understood. In this thesis, first-principles (i.e. parameter-free) calculations are performed with the aim of connecting experimentally-measured photoemission data to the underlying atomistic and electronic structure of interfaces found in DSCs. The principal system under study is the interface between anatase titanium dioxide (TiO_2) and the "N3" dye molecule, one of the most widely-investigated device designs in DSC research. Atomistic models of the interface are determined within density-functional theory. Core-level spectra of these interface models are then calculated using a ΔSCF approach. Comparison of the calculations to published experimental data finds that intermolecular interactions have a significant effect on the spectra. Next, the electronic structure of bulk TiO_2 and of isolated N3 molecules is calculated using the *GW* approximation and ΔSCF method respectively. For the former, it is shown that including Hubbard U corrections in the initial Hamiltonian reduces the *GW* gap by 0.4 eV. These calculations are then used to determine the valence photoemission spectrum of the full interface. By including image-charge effects, thermal broadening and configurational disorder, quantitative agreement with experimentally-measured spectra is demonstrated. In addition to the N3/TiO_2 system, calculations of the core-level spectra of the interfaces between TiO_2 and H_2O and bi-isonicotinic acid are also presented. The thesis concludes with a study of the X_2Y_3/TiO_2 interfaces (X=Sb, Bi; Y=S, Se) found in recently-developed semiconductor-sensitized solar cells.

Chapter 1

Introduction

1.1 Solar Photovoltaics

1.1.1 Renewables and the global energy demand

Meeting the environmental and economic cost of powering an ever-developing world must surely be the scientific challenge of the 21st century. The astounding technological progress achieved from the industrial revolution onwards has been fuelled by burning coal, oil and natural gas, releasing CO_2 (among other compounds) into the atmosphere [1]. The realisation that an increased concentration of greenhouse gases could lead to a dangerous rise in global temperatures prompted governments across the world to pledge to manage their CO_2 emissions such that the aforementioned rise might be limited to below 2°C by 2100 [2]. Yet Ref. 3 reports that, in the decade 2000–2010, the average year-on-year rise in CO_2 emissions was 3.1%, compared to 1.0% in the 1990s. The authors point out that this trend corresponds to the most pessimistic predictions of the world's ability to curb emissions, and is more consistent with climate models which predict a rise of 4°C by 2100 [3].

Aside from the threat of irreversible climate change, issues of economic and political uncertainty also motivate a rethink of energy policy. To take a local example, the UK's largest single source of electricity is natural gas, in spite of domestic production being in decline since 2000 [4]; consequently consumers are heavily exposed to price fluctuations in international markets. Cheap (and polluting) coal is the next largest source of electricity, leaving 18% and 9% of the total supply to be accounted for by nuclear and renewables respectively in 2011 [4]. Nuclear energy is considered low-carbon, in the sense that once the plants are operational they do not contribute to net CO_2 emissions; thus in spite of its negative population perception, nuclear is likely to play an important role in the intermediate term [5].

Renewable energy—that is, generating useful power without depleting natural resources—seems an elegant method of avoiding both emissions and having to rely on imported energy. Again focusing on the UK, it is instructive to consider the "back-of-the-envelope" calculations of Ref. 5 which highlight two key practical points, namely that (a) even making optimistic assumptions (like covering 10% of the country with windmills) the potential supply from renewables could only just balance projected demand, and (b) there is no single renewable technology which provides a solution to the energy problem. Instead, realistic energy policies suppose that a mix of renewable sources could account for a significant fraction of total energy generation.

The focus of this thesis is on emerging solar photovoltaic (PV) technologies. In the UK, PV contributes to the overall electricity market through rooftop installations; the 2011 axing of favourable "feed-in" tariffs by the UK government [6] seemed to make it clear that solar PV is not currently considered part of a renewable energy solution. Yet in the same year the United States Department

of Energy launched the "SunShot Initiative", with the goal of making solar energy "cost-competitive with other forms of energy by the end of the decade" [7]. A recent report [8] found that achieving this goal, which corresponds to a cut in 75% of the current price of solar energy, could lead to solar providing 14% of the United States' electricity requirements by 2030. Meanwhile the Chinese government are firmly pushing the manufacture of green energy solutions, with the country leading the world in solar panel production [9]. As such solar PV technology is a subject of global interest and importance.

1.1.2 Principles of solar PV

The fundamental goal of solar photovoltaics is to convert energy from the sun into electricity. Upon the absorption of a photon in a PV device, an excited electron-hole pair is generated. In order to split this bound pair into free charge carriers, PV devices incorporate some element of asymmetry, which drives the particles apart. Without this process the electron-hole pair would simply recombine, re-emitting a photon and thus losing the incident energy. The potential difference between the separated electrons and holes can then be used to power an external load.

A number of PV device concepts have been developed employing different classes of materials and charge separation processes. The most widely-used technologies are based on microscopic homojunctions between p and n-type semiconductors, where the ionised dopants form an electric field across the active layer [10]. Typical materials used in such devices are silicon or III-V compounds like GaAs or InP [11]. Building layers of such materials forms multijunction solar cells (e.g. InGaP/GaAs/InGaAs), which can harvest a greater proportion of the solar spectrum. More complicated heterojunction structures form the basis

of thin-film photovoltaics, which employ sandwiches of different semiconductors chosen to combine optimal properties (e.g. CdS and Cu(In,Ga)Se_2, CIGS [12]).

As an alternative to semiconductor devices one can instead consider organic and molecular light absorbers. In such materials the electron-hole pairs are too strongly bound to be split by electric fields [13]. Instead the energy barrier is overcome precisely at the interface of the light absorber with a substrate or acceptor molecule. The difference in energy between the quantum mechanical states located on the absorber and substrate provides the driving force to split the electron-hole pair and produce a current. All-organic, "bulk heterojunction" devices generally combine conjugated polymers such as MEH-PPV with films of acceptor molecules like C_{60} to form an interpenetrating network [14]. Alternatively, employing semiconductors as substrates forms the basis of dye-sensitized [15], quantum dot and semiconductor-sensitized [16; 17], and hybrid organic-inorganic [18] solar cells. Such devices are generally cheaper and easier to produce, at the expense of a much-reduced performance compared to conventional designs (see below).

1.1.3 Characterising solar cells

When comparing different solar cells, a popular figure-of-merit is the power conversion efficiency η. This is the dimensionless ratio of outgoing power obtained from a device to incoming solar radiation. A solar cell's performance will generally depend on the wavelength of the incident light, so it is standard practice to report the efficiency of the device when illuminated with "AM (air mass) 1.5 radiation". This is a synthetic spectrum which has an integrated intensity of 1000 Wm^{-2} and takes into account the atmospheric absorption of certain wavelengths [13]. Experimental subtleties associated with efficiency measurements can sometimes

hamper the reproducibility of results made by individual laboratories [19], which motivates the use of standardised tests performed by central laboratories like the National Renewable Energy Laboratory (NREL [20]).

Apart from the power conversion efficiency it is important to determine a device's current-voltage characteristic behaviour. Two key quantities are the short-circuit current density J_{SC} and the open-circuit voltage V_{OC}. For an optimal cell the current and voltage delivered are independent of each other; deviation from this behaviour is quantified through the fill factor f, which is related to η through [13]:

$$\eta = f \, \frac{J_{SC} V_{OC}}{P_s} \tag{1.1}$$

where P_s is the power density for the incident radiation. Therefore f, J_{SC} and V_{OC} are the essential quantities which determine η.

1.1.4 Cost vs. efficiency

Every six months sees the publication of solar cell efficiency tables (Ref. 11 is the November 2012 version), which compare the performance of the latest solar cell designs. At the high-performance end of the table sit devices based on GaAs; the world leader is a multi-junction cell InGaP/GaAs/InGaAs with η=37.7%, while a thin-film GaAs cell is the best performing device based on a single material with η=28.8%. The last two years also saw GaAs overtake Si in the performance tables for photovoltaic modules, i.e. arrays of cells which deliver a practically useful voltage.

The record efficiencies of dye-sensitized and all-organic cells are somewhat less impressive in comparison, at 11.9% (9.9%) and 10.7% (6.8%) respectively (the numbers in brackets are for modules) [11]. Yet the reason that these novel

devices continue to be investigated in spite of their relatively poor performance is found in economics. Firstly, molecular devices tend to perform better both in low-light conditions and at high temperatures which allows greater flexibility in siting the modules [21]. On the manufacturing side, organic devices are generally produced in ambient conditions without requiring high vacuum [22]; indeed photovoltaic films can be printed onto large-scale, flexible substrates via roll-to-roll processing [23]. Also, most of the raw materials used to construct these devices are cheap, abundant and of low purity in contrast to more conventional solar cell designs [13]. Combined, these factors reduce the cost per unit area of the cell, which helps to offset the low η. Indeed the target laboratory efficiency for commercially-viable dye-sensitized solar cells is usually quoted in the literature to be just 15% [21; 24].

1.1.5 Length-scales in molecular devices

From the point of view of fundamental science, devices based on organic or molecular light absorbers present a challenge to theories of the nanoscale. Depletion layers in silicon *p*-*n* junctions are generally a few micrometres in size, allowing charge separation to be treated with electrostatic models [10]. By contrast in molecular devices the electron-hole separation occurs on sub-nanometre length-scales, where classical models can be expected to break down. Any theoretical attempt to understand the underlying physical processes occuring in these devices must therefore start from a quantum mechanical description of the electrons.

1.2 Dye-sensitized solar cells

Of the various molecular PV designs, dye-sensitized solar cells (DSCs) currently hold the highest value of η [11]. DSC research is predominantly an experimental field with a strong emphasis on device optimisation, but there is also scope for an investigation of the basic physics which underpins DSC operation. The materials and interfaces studied in this work are some of the most well-known DSC systems, in the sense that they have been the subject of decades of experimental and theoretical investigation. However, there is still plenty of work to be done to understand the range of physical phenomena which determine the behaviour of the DSC, and how such knowledge might be used to push future devices towards η=15%.

1.2.1 Operating principle of the DSC

Figure 1.1 shows schematic illustrations of a standard dye-sensitized solar cell and its photovoltaic operation. Fundamentally there are three key components, capped by transparent electrodes:

- *S*, a semiconducting substrate which typically has a wide band gap
- *D*, a light-absorbing dye molecule adsorbed on *S*
- *HT*, a hole-transporting medium in the form of a liquid electrolyte or a solid-state hole conductor

The process of coating *S* with *D* is known as sensitization.

The first step in the DSC operating cycle is the absorption of a photon by the dye molecule *D*. The photoexcited dye has sufficient energy to inject an electron into the conduction band of the semiconductor *S*. However thanks to the

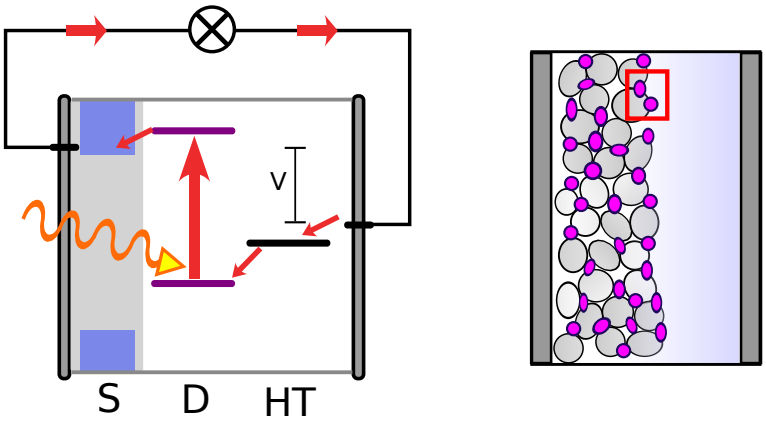

Figure 1.1: Schematic illustrations of a dye-sensitized solar cell (DSC). The left diagram (based on Fig. 1 of Ref 15) shows how an electrical current is generated (red arrows) by the absorption of a photon by a dye molecule D, electron injection into the substrate S and regeneration of the dye by a hole transporter HT. The difference in quasi-Fermi levels at the electrodes gives rise to a photovoltage V. The right picture illustrates a typical device based on a nanostructured semiconductor film sensitized with dye molecules (grey and purple ovals), with the interface identified in the red rectangle.

type-II (staggered gap) alignment of the molecular energy levels and semiconductor bands, the hole remains on the dye. Thus the energy-level alignment at the dye/semiconductor interface takes the role of the electrostatic field in a conventional solar cell of driving the electron and hole apart. The electron is then transported through the semiconductor to the external load, while the circuit is completed when the oxidised dye is regenerated by the hole transporter. The difference in quasi-Fermi levels at the electrodes gives rise to a photovoltage V.

1.2.2 Device optimisation

The partitioning of the system into components as above illustrates a primary strength of the DSC concept, which is that each ingredient has a specific function which can be optimised independently. For instance one can choose S to have optimal electron transport properties while D can be chosen to maximise the ab-

sorption of the solar spectrum. This is in contrast to conventional devices where a single material must simultaneously have good transport and light absorption properties [13].

The work in this thesis focuses on the interface formed between the sensitizing molecule and the semiconductor, i.e. D and S, with particular emphasis on the energy-level alignment. The alignment plays a crucial role in device operation and performance. The excited state of the dye molecule must be sufficiently energetic for the electron to be able to access the semiconductor conduction band. Yet an excited-state energy which is far higher than the conduction band edge results in an overpotential, where a large fraction of the initial energy provided by the photon is lost when the electron relaxes to the quasi-Fermi level of the semiconductor. Schematically this is illustrated in Fig. 1.1; applying an upward shift to the energy levels of S reduces V, which in turn reduces the power conversion efficiency (equation 1.1). As such it would be desirable to engineer the band offsets such that there was an optimum matching of energy levels across the interface.

1.2.3 Basic materials

In O'Regan and Grätzel's original DSC reported in 1991 [15], nanoparticles of titanium dioxide (TiO_2) deposited on flourine-doped tin oxide (FTO) were employed as the semiconductor. The light-absorbing dye molecule was a ruthenium-based complex, and a liquid iodide/triiodide electrolyte and a platinum-coated counterelectrode completed the circuit. The resulting cell had a power conversion efficiency of η=7.1%. Since then attempts have been made to improve device performance through variation of the materials used in the three components.

Semiconductors

Titanium dioxide has remained the most popular choice for the wide-gap semiconductor in DSCs. More generally TiO_2 can be considered one of the most important transition metal oxides thanks to its applicability to a range of fields including photocatalysis [25], energy storage [26] and even medicine [27]. Arguably the pivotal breakthrough made by O'Regan and Grätzel was to use nanostructured films of TiO_2, composed of particles of a few tens of nanometres in diameter [15]. By using such films, they increased the surface area available for dye adsorption by a factor of 780 compared to a flat TiO_2 sheet of the same macroscopic size; the increased light absorption achieved through the higher dye loading dramatically enhanced the photocurrent. Synthesising TiO_2 nanostructures such as nanotubes, nanowires and nanosheets has become a large research field in its own right [28; 29] and there is a growing number of examples where these more exotic structures have been used to construct DSCs [30; 31]. Nonetheless the nanoparticle film is still the most widely-used structure in device fabrication [21].

Aside from TiO_2, other possible choices for the semiconductor substrate are ZnO or SnO_2, which exhibit enhanced electron mobilities [32; 33] However such devices still lag behind TiO_2-based DSCs in terms of overall performance, with a top η of 7.5% for a ZnO device [34].

Sensitizing molecules

While the number of potential sensitizers is extremely large (c.f. the 214 examples in Ref. 21), ruthenium-based dyes like N3 [36], N719 [35] and black dye [37] (Figure 1.2) have dominated DSC research. These molecules belong to a wider class of metal-organic dyes, which exhibit the best performance among sensitizers. However since these dyes contain metals which might be rather expensive and/or

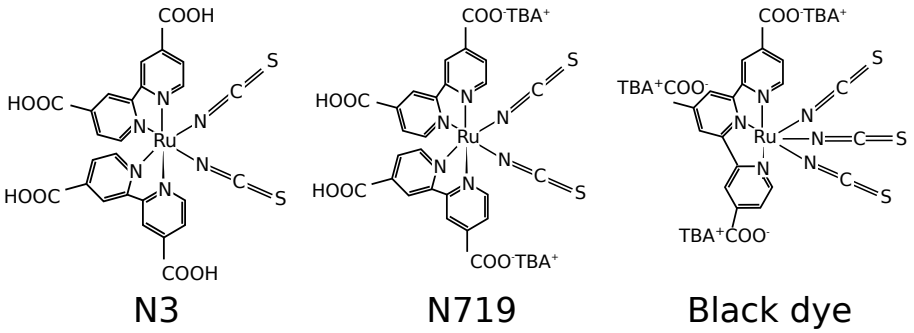

Figure 1.2: Diagrams of the Ru-based dyes N3, N719 and black dye. Note the similarity of N3 and N719, differing only in the replacement of two protons with tetrabutylammonium counterions [35].

toxic, there have been efforts to use all-organic dyes [38]. These dyes have the added advantage of an enhanced extinction coefficient, making them particularly suitable for solid-state devices (see below).

Hole transporters

The most widely-used method of regenerating the oxidised dye is via a liquid electrolyte, as used in O'Regan and Grätzel's 1991 design [15]. Here, iodide salts are dissolved in a (generally) organic solvent like acetonitrile [21]. However a breakthrough in efficiency was recently achieved in a device employing a Co-based electrolyte combined with a porphyrin dye, breaking all previous records with a reported η of 12.3% [39].

While giving the best cell performance, the high volatility of standard electrolytes makes them less attractive for practical applications, as they have to be totally sealed to prevent evaporation [40]. One approach is to employ ionic liquids [41], although a higher viscosity hinders dye regeneration. An even more attractive prospect is to dispense with the liquid altogether and employ a solid-state hole transporter [42]. Both organic [43] and inorganic [44] materials are viable options. The principle difficulty with solid-state devices is that the hole

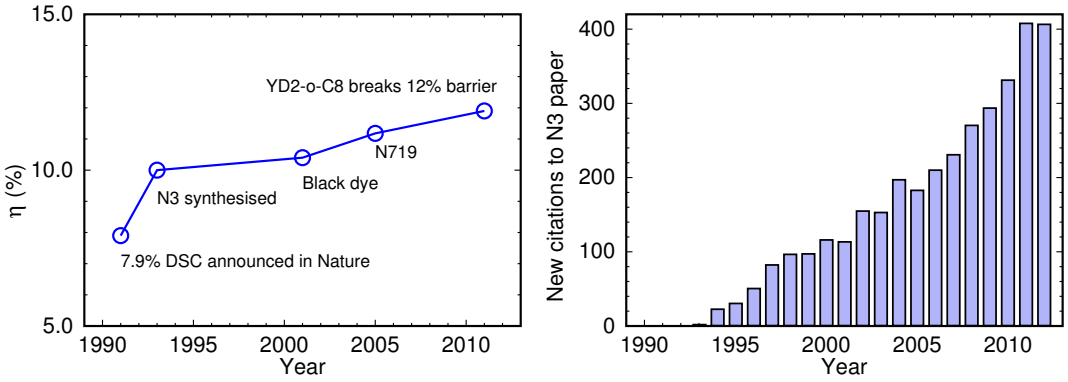

Figure 1.3: Data illustrating the important role of the N3 molecule in DSC research. The left plot charts the highest power conversion efficiencies reported for DSCs, starting with O'Regan and Grätzel's Nature paper in 1991 [15], and then subsequent improvements [35–37; 39; 45] The right plot shows the number of new citations received each year by the paper describing the synthesis of N3 since its publication in 1993 [36], according to the Web of Science biblographic database (`http://wok.mimas.ac.uk/`).

transporter cannot easily penetrate the mesoporous network of semiconductor nanoparticles, preventing the necessary intimate contact with the photoexcited dye; a partial solution is to employ organic sensitizers with high extinction coefficients, so that light absorption is efficient even for a monolayer [40].

1.2.4 The N3/TiO_2 interface

Out of all of the various sensitizer/semiconductor combinations, one particular system—the Ru-based dye $Ru(dcbpyH_2)_2(NCS)_2$ (also known as N3 [36]) adsorbed on mesoporous TiO_2—has dominated DSC research. Figure 1.3 charts some of the milestones in the evolution of DSC performance. In 1993 a 10% power conversion efficiency was demonstrated for N3/TiO_2/liquid electrolyte cells [36]. Gradual improvements in efficiency were realised by modifying the original structure of N3 by introducing counterions [35] or substituting ligands [37] (N719 and black dye; Fig. 1.2). But it was only in 2011 that a totally different design concept

took the efficiency record from the N3 family [39]. Indeed, charting the number of citations per year to the original 1993 N3 paper [36] (Fig. 1.3) shows the continued interest in this dye.

Thanks to its technological importance, the N3/TiO_2 interface is one of the most studied systems in DSC research. Alongside device optimisation various studies have addressed more fundamental questions concerning the atomistic structure, energy-level alignment and electron injection properties at the interface. Yet the inherent complexity of the system makes describing even its most basic properties rather difficult, and there remain a number of unanswered questions. Consequently the N3/TiO_2 interface represents a rich system for theorists, not least because there is a decent amount of experimental data that can be used to validate models.

1.3 Characterisation of interfaces through PES

1.3.1 Basic principles

Photoemission or photoelectron spectroscopy (PES) can provide valuable insight into the atomistic and electronic structure of interfaces. The basic concept is illustrated in Figure 1.4. A sample is illuminated by a beam of photons of fixed energy E_γ. Absorption of a photon can result in the emission of an electron through the photoelectric effect. The kinetic energy E_{kin} of the photoelectron is then measured, for instance by tracking its deflection by an electrostatic field [46]. Adjusting the electron energy analyser allows the full range of the kinetic energy to be sampled, constructing a photocurrent spectrum like that shown in blue in the figure. The theoretical challenge is to understand how the underlying electronic structure of the sample (orange area) relates to the observed spectrum.

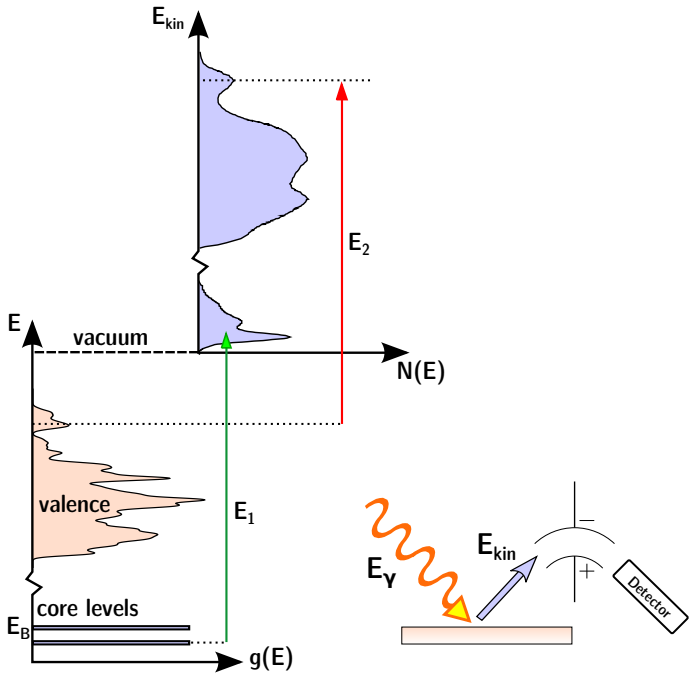

Figure 1.4: Schematic illustrations of the principles of photoelectron spectroscopy (based on Figs. 1.4 and 1.5 of Ref. 46). A sample is illuminated with photons of energy E_γ, which causes the liberation of electrons of energy E_{kin} via the photoelectric effect. Measuring the intensity as a function of E_{kin} constructs a spectrum (blue shaded area). Depending on the energies used (E_1, E_2) one can access core or valence states (orange area). The blue photoemission spectra were obtained experimentally and reported in Refs. 47 and 48.

1.3.2 Calculating the photocurrent

The energy dependence of the photocurrent I has a deceptively simple form from Fermi's golden rule [46]:

$$I(E_{\text{kin}}) \propto \frac{2\pi}{\hbar} \sum_f |\langle \Psi_f | \Delta | \Psi_i \rangle|^2 \, \delta[E_f(E_{\text{kin}}) - E_i - E_\gamma] \tag{1.2}$$

This equation describes a system, initially in state $|\Psi_i\rangle$ with energy E_i, absorbing a photon of energy E_γ in a transition mediated by the dipole operator Δ. The transition rate sums over all possible new states $|\Psi_f\rangle$ with energy E_f, which incorporate a photoelectron of energy E_{kin}. The δ-function describes conservation of energy $E_f = E_i + E_\gamma$. The difficulty with the above is that both the states Ψ and energies E are many-body quantities; that is, they are the solutions of a Hamiltonian which contains a multitude of interacting electrons, and consequently extremely complicated objects. Turning equation 1.2 into a soluble expression requires the techniques of many-body pertubation theory described in Chapter 3.

1.3.3 Valence and core-level photoemission

Figure 1.4 demonstrates the important concept that one can access different energy scales depending on the energy of the incident photons and the range of kinetic energies considered. For instance, illuminating the sample with ultraviolet or soft X-ray radiation (E_γ ∼100–500 eV, e.g. Refs. 48 and 49) extracts the most weakly-bound electrons (E_2 in Fig. 1.4). These states correspond to the edge of the valence band for solid-state systems and the highest occupied orbital in the case of molecules. In the context of solar cells, these valence photoemission spectroscopy experiments provide information about the alignment of the frontier orbitals, which was shown in Fig. 1.1 to affect the voltage delivered by a device.

Increasing the photon energy further (E_γ ∼1 keV, e.g. Ref. 47) allows the most tightly-bound electrons to be liberated from the sample (E_1 in Fig. 1.4). In this case, the electronic states are atomic-like orbitals, e.g. the 1s shell, which do not directly participate in bonding. However the binding energy of these core electrons is sensitive to the chemical environment of their parent atom. For instance the binding energy of the 1s electron in atomic Na is 1079.0 eV, while for the Na atom in NaCl it is 1077.4 eV [46]. Constructing an entire spectrum of these core-level shifts in principle allows the identification of bonds which have formed at the interface.

A further point to note is that through variation of the photon energy, it is possible to sample electrons emitted only from within a few Å of the surface of the sample. Therefore synchrotron X-ray photoelectron spectroscopy, which allows access to a wide range of photon frequencies, is highly surface sensitive and ideally suited to the study of interfaces.

1.4 Outline and organization of the thesis

The aim of this thesis is to form a connection between experimentally-measured photoemission spectra and an atomistic description of interfaces relevant to dye-sensitized solar cells, by means of first-principles calculations. "First-principles" here refers to a theoretical description which is free from empirical parameters. As noted above many key processes in DSCs occur at sub-nanometre length-scales, so it is essential to employ a theory based on quantum mechanics. Density-functional theory (DFT) fulfils this requirement and is well-suited to describe these interfaces. Chapter 2 provides an overview of DFT and describes some of the less-standard techniques used in this thesis, including the ΔSCF method and

Coulomb truncation schemes. In describing photoemission experiments, which probe the excited states of the system, it is necessary to go beyond the ground-state description of DFT and employ a perturbation theory approach in the so-called *GW* approximation, which is the subject of Chapter 3.

Chapters 4–6 contain the principal results of this thesis, which form an investigation of the N3/TiO_2 interface introduced above. Chapter 4 considers the atomistic structure of the dye molecule adsorbed on the TiO_2 surface through total energy calculations and comparison of calculated core-level spectra with experimental measurements. Chapter 5 moves to the electronic structure of bulk TiO_2 in the *GW* approximation and of isolated N3 molecules through the ΔSCF method. In particular it is shown that incorporating Hubbard U corrections into the *GW* approach has a sizeable effect on the calculated band gap of TiO_2. Chapter 6 brings everything together in the calculation of the valence photoemission spectrum of the N3/TiO_2 interface, including image charge effects, thermal broadening and configurational disorder. As in Chapter 4, the calculated spectrum is compared to experiment.

The final two chapters move beyond the N3/TiO_2 interface. Chapter 7 extends the method of calculating the core-level shifts used in Chapter 4 so that it might be applied to other TiO_2-based interfaces. The systems investigated are water and the bi-isonicotinic acid molecule; in both cases, comparison of experimental and theoretical spectra produces results which challenge current understanding of these interfaces. Finally, Chapter 8 considers a novel design of solar cell, based on the DSC, which replaces the dye molecule with a semiconductor sensitizer. An atomistic model of this new interface is proposed and a simple method used to calculate the energy-level alignment at the interface.

Chapter 2

Electronic structure in DFT

This is the first of two chapters devoted to the theory behind the calculations performed in this thesis. Here I focus on density-functional theory, a powerful tool for obtaining an ab initio description of solids and molecules. This chapter is not intended to provide a comprehensive survey of the theory, but rather cover the specific techniques which will be used in later chapters. For instance all calculations in this thesis employ periodic boundary conditions, plane-wave basis sets and pseudopotentials, so I briefly review these aspects, and pay particular attention to spurious interactions that can occur between periodic replicas of molecules. Since the atomistic structures of dye-sensitized solar cell interface models are obtained in a damped first-principles molecular dynamics approach, and the temperature dependence of energy-level alignments is also investigated, I discuss Car-Parrinello MD. For TiO_2, the prototype transition metal oxide, it is useful to consider also the DFT+U approach which has emerged as a popular tool for dealing with strongly-correlated systems. Finally in the context of photoemission it is particularly interesting to study the ΔSCF method, which allows access to certain excited-state properties within standard DFT.

2.1 Density-functional theory

2.1.1 The electronic equation

A first-principles approach to determining the electronic structure of a solid (ignoring relativistic effects) requires solving the Schrödinger equation for the joint electron-nuclei system:

$$\left[\sum_j \hat{\mathbf{T}}_e(\mathbf{r_j}) + \sum_j V_{ie}(\mathbf{r_j}, \mathbf{R}) + \sum_{j \neq k} V_{ee}(\mathbf{r_j}, \mathbf{r_k}) + \hat{\mathbf{T}}_i(\mathbf{R}) + V_{ii}(\mathbf{R})\right] \Phi(\{\mathbf{r}\}, \mathbf{R}) = E\ \Phi(\{\mathbf{r}\}, \mathbf{R}) \quad (2.1)$$

Here, $\{\mathbf{r}\}$ and $\mathbf{R}$ represent the entire set of electron and nuclei positions, respectively (e.g. $\mathbf{R} \equiv \mathbf{R_1}, \mathbf{R_2}, \mathbf{R_3}, ...$). The $\hat{\mathbf{T}}$'s are kinetic energy operators (e.g. $-\frac{\nabla^2}{2}$), and the three potentials account for electron-nuclei, electron-electron and nuclei-nuclei interactions.

Throughout this thesis the nuclei are treated as classical objects. The electronic part of the above is taken to define a $\mathbf{R}$-dependent "potential energy surface" $E^{\mathbf{R}}$ on which the nuclei move, through:

$$\left[\sum_j \hat{\mathbf{T}}_e(\mathbf{r_j}) + \sum_j V_{ie}^{\mathbf{R}}(\mathbf{r_j}) + \sum_{j \neq k} V_{ee}(\mathbf{r_j}, \mathbf{r_k})\right] \Psi^{\mathbf{R}}(\{\mathbf{r}\}) = E^{\mathbf{R}}\ \Psi^{\mathbf{R}}(\{\mathbf{r}\}) \quad (2.2)$$

where the inter-nuclei repulsion $V_{ii}(\mathbf{R})$ has been absorbed into $V_{ie}^{\mathbf{R}}$.

The major problem with equation 2.2 is the electron repulsion term $V_{ee}(\mathbf{r_j}, \mathbf{r_k}) = \frac{1}{|\mathbf{r_j} - \mathbf{r_k}|}$, which couples the behaviour of one electron to all of its neighbours. As a result even just writing down the many-electron wavefunction $\Psi^{\mathbf{R}}(\{\mathbf{r}\})$, let alone solving for it, becomes a problem of formidable complexity for realistic systems.

2.1.2 Hohenberg-Kohn/Kohn-Sham description

In order to circumvent the difficulty of the many-electron wavefunction, Hohenberg and Kohn [50] reformulated the problem in terms of the density of electrons, $\rho(\mathbf{r})$. In particular, they introduced a functional of the density $E_v^{\mathbf{R}}[\rho]$ which has a minimum value when $\rho(\mathbf{r})$ coincides with the electron density of the system in its ground state for a given ionic configuration. The corresponding value of $E_v^{\mathbf{R}}$ at this density is precisely the ground-state solution of equation 2.2. This approach is the foundation of density-functional theory (DFT). The energy functional can be written as [51]:

$$E_v^{\mathbf{R}}[\rho] = \int V_{ie}^{\mathbf{R}}(\mathbf{r})\rho(\mathbf{r})d\mathbf{r} + T_s[\rho] + \frac{1}{2}\int \frac{\rho(\mathbf{r})\rho(\mathbf{r}')}{|\mathbf{r}-\mathbf{r}'|}d\mathbf{r}d\mathbf{r}' + E_{XC}[\rho] \tag{2.3}$$

The first term is the interaction of the density with the ionic potential. $T_s[\rho]$ is the kinetic energy of a gas of non-interacting electrons whose density is ρ, and the next term is the classical Hartree energy of a charge density interacting with itself. The remaining exchange-correlation energy $E_{XC}[\rho]$ contains all of the many-body effects not covered by the other terms. Unfortunately an exact expression for $E_{XC}[\rho]$ is not known, and instead must be approximated.

Starting from equation 2.3, Kohn and Sham [51] constructed the density as a sum over single-particle orbitals $\psi_m(\mathbf{r})$:

$$\rho(\mathbf{r}) = \sum_m^N |\psi_m(\mathbf{r})|^2 \tag{2.4}$$

where N is the number of electrons in the system. Performing the functional derivative of equation 2.3 subject to the correct normalisation $\int \rho(\mathbf{r})d\mathbf{r} = N$

yields the so-called Kohn-Sham equations with eigenvalue solutions ε_m:

$$\left[-\frac{\nabla^2}{2} + V_{ie}(\mathbf{r}) + V_H(\mathbf{r}) + V_{XC}(\mathbf{r})\right]\psi_m(\mathbf{r}) = \varepsilon_m\psi_m(\mathbf{r}) \tag{2.5}$$

where for clarity the parametric $\mathbf{R}$ dependence has been dropped. Here the Hartree potential $V_H(\mathbf{r})$ has been introduced:

$$V_H(\mathbf{r}) = \int \frac{\rho(\mathbf{r}')d\mathbf{r}'}{|\mathbf{r} - \mathbf{r}'|} \tag{2.6}$$

and also the exchange-correlation potential

$$V_{XC}(\mathbf{r}) = \frac{\delta E_{XC}[\rho]}{\delta\rho(\mathbf{r})} \tag{2.7}$$

Since both V_H and V_{XC} depend on ρ, the Kohn-Sham equations must be solved self-consistently.

Comparing equations 2.3 to 2.4 and 2.5 gives the ground-state energy E in terms of the Kohn-Sham eigenvalues ε_m:

$$E = \sum_m^N \varepsilon_m - \frac{1}{2}\int \frac{\rho(\mathbf{r})\rho(\mathbf{r}')}{|\mathbf{r} - \mathbf{r}'|}d\mathbf{r}d\mathbf{r}' + E_{XC}[\rho] - \int V_{XC}(\mathbf{r})\rho(\mathbf{r})d\mathbf{r} \tag{2.8}$$

2.1.3 The exchange-correlation potential

Of course the usefulness of the above critically depends on finding a reasonable approximation for V_{XC}. Arguably DFT owes its success to the remarkable power of the local-density approximation (LDA) whereby

$$E_{XC}^{\mathrm{LDA}}[\rho] = \int \epsilon_{XC}(\rho(\mathbf{r}))\rho(\mathbf{r})d\mathbf{r}, \tag{2.9}$$

$$V_{XC}^{\mathrm{LDA}}(\mathbf{r}) = \frac{\delta}{\delta\rho}\left[\epsilon_{XC}(\rho(\mathbf{r}))\rho(\mathbf{r})\right] \equiv \mu_{XC}(\rho(\mathbf{r})) \tag{2.10}$$

and $\epsilon_{XC}(\rho(\mathbf{r}))$ is the exchange-correlation energy per particle of the homogeneous electron gas of density $\rho^{HEG} = \rho(\mathbf{r})$. As emphasised by equation 2.10, in the LDA the exchange-correlation potential at a given point depends only on the electronic density at that same point. The calculation of ϵ_{XC} by Ceperley and Alder [52] and subsequent parameterisations (e.g. Ref. 53) allowed the practical realisation of DFT calculations employing the LDA.

The LDA would be exact if the system under study was indeed the homogeneous electron gas, and might be expected also to hold in the limit of slowly-varying or very high density. An intuitive next step would be to suppose that the exchange-correlation potential at a point $\mathbf{r}$ depends on both the density and its derivative at that same point, called the generalised-gradient approximation:

$$E_{XC}^{\mathrm{GGA}}[\rho] = \int \epsilon_{XC}^{\mathrm{GGA}}(\rho(\mathbf{r}), |\nabla\rho(\mathbf{r})|)\rho(\mathbf{r})d\mathbf{r}, \tag{2.11}$$

Different parameterisations of this expansion have led to a number of GGA functionals, e.g. PBE [54], PW91 [55] and BLYP [56; 57]. Interestingly the improvement on moving from LDA to GGA is by no means universal; indeed there are many systems where the LDA description is superior. A possible explanation is provided in the following section.

2.1.4 The LDA and the exchange-correlation hole

In spite of the apparent simplicity of the LDA, it has been applied successfully to a wide class of materials [58]. In this context it is interest to restate the LDA invoking the concept of an "exchange-correlation hole", $\rho_{XC}(\mathbf{r}, \mathbf{r}')$. $\rho_{XC}(\mathbf{r}, \mathbf{r}')$ is

defined in a rather abstract way through the pair-correlation function $g_\lambda(\mathbf{r}, \mathbf{r}')$ (c.f. Ref. 58 pg. 143), but it allows E_{XC} to be written as [59]:

$$E_{XC}[\rho] = \frac{1}{2} \int \frac{\rho(\mathbf{r})}{|\mathbf{r} - \mathbf{r}'|} \rho_{XC}(\mathbf{r}, \mathbf{r}') d\mathbf{r} d\mathbf{r}' \tag{2.12}$$

According to equation 2.12 the contribution to the total exchange-correlation energy from a density element $\rho(\mathbf{r})$ is the Hartree energy of that element and the associated exchange-correlation hole. Furthermore $\rho_{XC}(\mathbf{r}, \mathbf{r}')$ obeys the sum rule

$$\int \rho_{XC}(\mathbf{r}, \mathbf{r}') d\mathbf{r}' = -1 \tag{2.13}$$

The LDA amounts to replacing the exact exchange-correlation hole of the real system with the exact exchange-correlation hole of the homogeneous electron gas, ρ_{XC}^{HEG}. Being exact, ρ_{XC}^{HEG} automatically satisfies equation 2.13. The Coulomb interaction between two distributions which determines E_{XC} in equation 2.12 depends more strongly on the integrated charge of the distributions rather than precise details of their shape. Therefore the fact that the LDA exchange-correlation hole integrates to the correct value of -1 is a major advantage of the method. Conversely, modifications to the LDA to account for particular effects (e.g. LDA+U, see below) may improve certain aspects of the theory, but will weaken the generality of the functional by violating the sum rule.

2.2 Practical calculations

2.2.1 Pseudopotentials

In principle the electron-nuclear interaction $V_{ie}(\mathbf{r})$ could be decomposed into a sum over the attractive Coulomb potentials of each nucleus. However describing the divergent $\frac{1}{\mathbf{r}}$ potential is rather expensive. Furthermore the most tightly-bound electrons of an atom tend not to play a large role in determining the properties of a condensed matter system. Indeed, the bonding between atoms is determined by the structure of the electronic wavefunctions at a few Bohr radii from the nucleus.

These considerations motivate the use of the pseudopotential method. Here the effects of the core electrons are combined with those of their parent nucleus to construct a new ionic pseudopotential. The pseudopotential generation method is engineered to yield pseudo-wavefunctions for the valence electrons which match the "true" single-particle states obtained in an all-electron calculation, outside of a given core radius. Within this radius the pseudo-wavefunction is smoother than its all-electron counterpart, containing no nodes, and is thus easier to deal with computationally.

A key property of a pseudopotential is that it is transferable. That is, although it is generated by solving the Schrödinger equation of an isolated atom, the pseudopotential must also provide a good approximation for the full potential in different environments. A standard criterion is norm-conservation [60–62], where the integrals of the squared pseudo and all-electron-wavefunctions match within the core region. Then, most electronic structure codes use pseudopotentials expressed in Kleinman-Bylander form [63; 64], where the potential consists of a local part $V_{loc}(r)$ and a short-ranged, non-local, angular momentum-dependent

part determined by projector functions χ:

$$V^{NC}(\mathbf{r})\psi_i(\mathbf{r}) = V_{l_{loc}}(r)\psi_i(r) + \sum_{l \neq l_{loc}} \sum_m \chi_{lm}(\mathbf{r}) E_l \int \chi^*_{lm}(\mathbf{r}')\psi_i(\mathbf{r}')d\mathbf{r}' \tag{2.14}$$

There is a free choice in selecting which angular momentum part is the local channel. Generally it makes sense to use the largest l channel, since this reduces the number of projector functions ($m = -l, -l+1, ..., l$). However sometimes it is necessary to choose a different channel in order to eliminate "ghost states", that is, solutions of the Schrödinger equation which are artefacts of the separated pseudopotential rather than physical quantities [64].

While removing the nodes of the pseudo-wavefunction in the core region leads to smoother functions, for first-row elements (with small core regions) the norm-conservation condition can still lead to sharply peaked orbitals. Vanderbilt ultrasoft pseudopotentials [65] relax the norm-conservation condition, instead augmenting the density so that the correct charge is contained in the core region. Ultrasoft pseudopotentials take the form

$$V^{US}(\mathbf{r})\psi_i(\mathbf{r}) = V_{loc}(r)\psi_i(r) + \sum_{nn'} \beta_n(\mathbf{r}) D_{nn'} \int \beta^*_{n'}(\mathbf{r}')\psi_i(\mathbf{r}')d\mathbf{r}' \tag{2.15}$$

where the expression for the density (equation 2.4) acquires a new term

$$\rho(\mathbf{r}) = \sum_i^N |\psi_i(\mathbf{r})|^2 + \sum_{nn'I} Q^I_{nn'}(\mathbf{r}) \langle \psi_i | \beta^I_n \rangle \langle \beta^I_{n'} | \psi_i \rangle \tag{2.16}$$

β^I_n and $Q^I_{nn'}$ are functions centred on a particular ion I, which vanish outside the core region, while the $D_{nn'}$'s are coefficients. n and n' are composite indices standing for angular momentum quantum numbers, but also label reference energies used to construct the pseudopotential. Normally two such energies are chosen,

which results in twice as many projector functions than for norm-conserving pseudopotentials. However a significant computational saving is achieved by having far smoother pseudo-wavefunctions. The hard part of the density is localised in small volumes, which can be efficiently treated in reciprocal-space codes (see below).

Although the ultrasoft scheme has been widely implemented in standard DFT codes, it is not always found in codes employing post-DFT methodology (e.g. the *GW* approximation, Chapter 3). This is because in the ultrasoft formalism pseudo-wavefunctions are not orthonormal, so computing matrix elements between orbitals (which often arise in post-DFT work) becomes more involved. As a consequence both norm-conserving and ultrasoft pseudopotentials play important roles in current calculations.

2.2.2 Basis sets

The Kohn-Sham equations are conveniently solved by decomposing the states into sums of basis functions and diagonalising the resulting matrix. A number of codes employ periodic boundary conditions and use plane waves as a basis set. Then, the Kohn-Sham states are described in terms of a Bloch wavevector $\mathbf{k}$ and a periodic function which can be decomposed into a Fourier sum over reciprocal lattice vectors $\mathbf{G}$:

$$\psi_{n,\mathbf{k}}(\mathbf{r}) = \sum_{\mathbf{G}}^{\mathbf{G}_{\max}} C_{n,\mathbf{k}}(\mathbf{G}) e^{i(\mathbf{k}+\mathbf{G})\cdot\mathbf{r}} \tag{2.17}$$

The magnitude of the largest reciprocal space vector used to describe the wavefunction $|\mathbf{G}_{\max}|$ is known as the plane wave cutoff which, together with the number of $\mathbf{k}$-points employed, must be converged numerically. The density is also expanded in plane waves; for norm-conserving pseudopotentials the required

density cutoff is $4 \times |\mathbf{G}_{\max}|$, while the presence of the augmentation charge in equation 2.16 requires a higher value for ultrasoft calculations. However since the augmentation charge is localised around the ions, a significant computational saving can be achieved in the double-grid technique [66], where the fine-grid Fourier transform is only performed on a small volume of real space.

The reciprocal-space formalism of DFT is detailed in Ref. 67. Some terms like the exchange correlation potential in the LDA are evaluated in real space, while other contributions (like the Hartree energy) have a simpler form in reciprocal space. Fast Fourier transforms allow switching between the two representations. One important aspect is that the Fourier transform of the Hartree potential diverges at $\mathbf{G} = 0$:

$$V_H(\mathbf{G}) = \frac{4\pi\rho(\mathbf{G})}{G^2} \tag{2.18}$$

which physically corresponds to the energy of an infinite array of charged objects being infinite. For a neutral system the divergences in the electron-electron, ion-ion and electron-ion potentials all cancel so the total energy is well-defined. However in calculating the potential the $V(\mathbf{G} = 0)$ components are always set to zero, which means that for periodic systems, the Kohn-Sham eigenvalues are only determined up to an arbitrary constant which depends on the number of ions and geometry of the simulation cell. As such, incorporating the results from one bulk calculation into another requires establishing a well-defined reference level (Chapter 6).

2.2.3 Coulomb interactions in periodic boundary conditions

As pointed out above the electrostatic energy of an infinite, neutral system is well-defined. In the case that a simulation cell has a net charge, the energy will diverge. Practically the divergence is removed by introducing a uniform compensating background (equivalent to setting $V(\mathbf{G} = 0) = 0$). Even so, the slow-decaying $1/R$ Coulomb potential leads to charged periodic images interacting with each other over large distances.

This problem is especially important when using plane waves and periodic boundary conditions to simulate charged molecules (c.f. Section 2.5). Ideally, the spurious interactions between periodic replicas should be removed by using a very large simulation cell. However since the number of plane waves in a calculation scales with the volume of the cell, it is desirable to find an alternative means of removing the effect.

Makov-Payne corrections

The Makov-Payne expansion [68] considers the convergence behaviour of a charged molecule in a vacuum with the length of a cubic simulation cell L. The resulting expression for the total energy E is:

$$E = E_0 + \frac{A_1}{L} + \frac{A_2}{L^3} + O(L^{-5}) \tag{2.19}$$

where the coefficients A_1 and A_2 can be expressed in terms of the Madelung constant of the lattice and quadrupole moment of the molecule [68]. The energy can be corrected either by calculating A_1 and A_2 directly, or by performing a set of calculations for different values of L and fitting to the polynomial above, thus

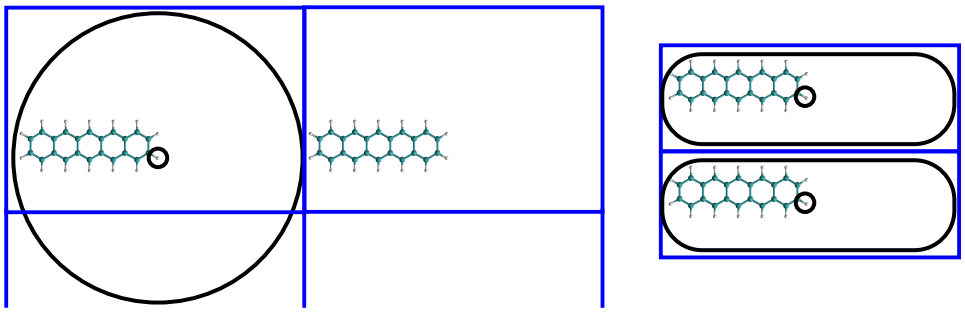

Figure 2.1: The concept of Coulomb truncation illustrated with the example of the pentacene molecule. The black line represents the range of the truncated Coulomb interaction, and the blue lines represent the simulation cell boundaries. The left-hand plot shows a spherical truncation. A large amount of empty space is needed to prevent periodic replicas interacting with each other. The right hand plot shows the Martyna-Tuckerman truncation [69]. Here the truncated interaction reflects the shape of the molecule, allowing for a more economical unit cell.

obtaining the limit of $L \to \infty$, E_0.

Coulomb truncation schemes

Correcting for the Coulomb interaction with the Makov-Payne approach is a post-processing step. An alternative is to self-consistently remove the spurious interactions from the outset by truncating the Coulomb interaction. For instance, supposing that the Coulomb interaction acts only within a sphere of radius R_C gives a new expression for its Fourier transform:

$$v^s(G) = \frac{4\pi}{G^2}\left[1 - \cos(GR_C)\right] \tag{2.20}$$

which no longer diverges at $G = 0$.

The procedure for choosing R_C is illustrated in Figure 2.1 for the pentacene molecule. In order that periodic images do not interact, the length of the simulation cell must be of order $2R_C$. Furthermore R_C must be large enough that

electrons at extremal edges of the molecule interact with each other. In practical calculations this quantity should be converged, but generally it is found to be around $D + 5$ Å, where D is the maximum distance between two atoms in the molecule.

Fig. 2.1 illustrates a shortcoming of the spherical truncation when it is applied to non-spherical molecules. Pentacene is long and planar; its length determines the value of R_C, but most of the simulation cell is empty space. A preferable truncation scheme would take into account the shape of the molecule. Further analytical expressions corresponding to cylindrical or sheetlike truncations are given in Ref. 70. Alternatively a general truncation scheme for an orthorhombic unit cell of sides L_x, L_y, L_z can be achieved simply by performing the Fourier transform numerically:

$$v^T(\mathbf{G}) = \int_{-\frac{L_x}{2}}^{+\frac{L_x}{2}} dx \int_{-\frac{L_y}{2}}^{+\frac{L_y}{2}} dy \int_{-\frac{L_z}{2}}^{+\frac{L_z}{2}} dz \times \frac{e^{-i\mathbf{G}\cdot\mathbf{r}}}{r} \tag{2.21}$$

This approach is the essence of the Martyna-Tuckerman truncation scheme [69]. As for the spherical case the simulation cell needs to be converged. As shown in the right diagram of Fig. 2.1 this method yields a considerable saving in the volume of the unit cell. Even so it is worth remembering that even here, 7/8 of the unit cell is empty.

The dipole correction for slab geometries

The final point to make about spurious Coulomb interactions concerns calculations on periodic slabs. Here there is periodicity in the xy plane, and a vacuum region along the z direction separating parallel slabs. Even if the slabs are charge neutral, they may still possess a dipole moment μ. On moving from one side

of the slab to another, there is a jump in potential energy of $\frac{4\pi\mu}{L_x L_y}$. This step is incommensurate with periodic boundary conditions. Consequently a spurious electric field arises across the unit cell, such that the correct planar-averaged potential $V(z)$ is modified by a linear term

$$V_{\text{code}}(z) = V(z) - \frac{4\pi\mu}{\Omega}\left(z - \frac{L_z}{2}\right), \quad 0 \leq z \leq L_z \tag{2.22}$$

where $\Omega = L_x L_y L_z$ and the middle of the slab lies at $z = \frac{L_z}{2}$.

The correction scheme of Ref. 71 removes the spurious field by introducing a compensating potential

$$V_{\text{corr.}}(z) = \frac{4\pi\mu}{\Omega}\left(z - L_z\left[\frac{1}{2} + \theta(z - z_0)\right]\right)$$

where the θ-function ensures that the correction is periodic; the position of the discontinuity z_0 must lie in the vacuum region. In addition to correcting the potential in the Kohn-Sham equations, it is also necessary to modify the expressions for total energy and the forces on the ions [71].

2.3 First-principles molecular dynamics

2.3.1 Forces and Born-Oppenheimer molecular dynamics

The fundamental idea of molecular dynamics (MD) is to calculate how the positions of the ions in a system evolve in time, so that thermodynamic averages of various quantites can be calculated. A first approach to MD could be to treat the ions classically and electrons quantum mechanically. The force on a particular

ion J, $\mathbf{F_J}$ is found through

$$\mathbf{F_J} = -\frac{\partial E_{\text{tot}}}{\partial \mathbf{R_J}} = -\langle\Psi|\frac{\partial H_{\text{el}}}{\partial \mathbf{R_J}}|\Psi\rangle - \frac{\partial E_{II}}{\partial \mathbf{R_J}} \tag{2.23}$$

where the total energy E_{tot} is the sum of the inter-ionic repulsion E_{II} and the electronic energy (equation 2.8). The second equality above is an example of the Hellmann-Feynman theorem, where the derivative of the total energy is in fact determined by the derivative of the Hamiltonian [72].

Given the forces on the ions at time t, the positions and velocities of the ions at $t + \delta t$ can be obtained by integrating the Newtonian equations of motion, for instance with the Verlet algorithm [73]. The new ionic positions are used to recalculate the forces, allowing a trajectory to be constructed. This approach is known as Born-Oppenheimer molecular dynamics. The intuitive interpretation is that the electrons move on a far faster timescale than the nuclei, such that they can always be considered in their ground state.

2.3.2 Car-Parrinello MD

The disadvantage of Born-Oppenheimer molecular dynamics is that for each timestep in the MD run, a fully-converged self-consistent electronic calculation must be performed. The forces must be determined to a sufficiently high accuracy that no errors are introduced in determining the trajectory [72]. The idea of Car-Parrinello molecular dynamics (CPMD) [74] is to simultaneously evolve the electrons and ions in time. The quantum states of the electrons are treated as classical variables $\phi_m(\mathbf{r})$ and $\dot{\phi}_m(\mathbf{r})$ with a fictitious mass μ, which allows the

formulation of the following Lagrangian:

$$\begin{aligned}\mathcal{L} &= \mu \sum_m \int d\mathbf{r} \left|\dot{\phi}_m(\mathbf{r})\right|^2 + \sum_J \frac{1}{2} M_J \dot{R}_J^2 - E_{\rm tot}(\{\phi_m, \mathbf{R_J}\}) \\ &\quad + \sum_{lm} \Lambda_{lm} \left(\int \phi_l^*(\mathbf{r}) \phi_m(\mathbf{r}) d\mathbf{r} - \delta_{lm} \right) \end{aligned} \tag{2.24}$$

The corresponding equations of motion are

$$\mu \ddot{\phi}_m(\mathbf{r}, t) = -\frac{\delta E}{\delta \phi_m^*(\mathbf{r}, t)} + \sum_l \Lambda_{ml} \phi_l(\mathbf{r}, t) \tag{2.25}$$

$$M_J \ddot{\mathbf{R}}_\mathbf{J} = -\frac{\partial E_{\rm tot}}{\partial \mathbf{R_J}} \tag{2.26}$$

where the orthogonality condition

$$\int \phi_l^*(\mathbf{r}, t) \phi_m(\mathbf{r}, t) d\mathbf{r} = \delta_{lm}$$

is enforced at every timestep. If ultrasoft pseudopotentials are used to describe the core-valence interactions, the orthogonality condition is relaxed and new terms appear in the equations of motion [66].

The functional derivative which appears in equation 2.25 is the same as that used to derive the Kohn-Sham equation 2.5. Therefore at equilibrium ($\mu \ddot{\phi}_m(\mathbf{r}, t) = 0$) the ϕ-functions co-incide with the Kohn-Sham states, up to a unitary transformation. The essential ingredient of the approach however is that the $\mathbf{R}$-dependence of $\frac{\delta E}{\delta \phi_m^*}$ exhibits a 'drag' on the electrons so that they track the motion of the nuclei, staying close to their ground state Born-Oppenheimer energy surface.

The Car-Parrinello scheme allows access to molecular dynamics through the Verlet integration of the equations of motion. The general justification for using

CPMD is that the computational saving of not having to perform a self-consistent electronic minimisation at every timestep outweighs the loss in accuracy of not having the electrons in their true ground state [75]. A smaller value for the fictitious mass μ will increase the accuracy of the calculated forces but reduce the stability of the MD run, so a trade-off is generally necessary. Standard values of μ range from 300-900m_e [72]; the simulations in this thesis use $\mu = 600m_e$. Benchmark calculations [75] often find that the CP-calculated forces only exhibit small fluctuations about those calculated with equation 2.23, but some systems (for instance D_2O-ice [76]) have been shown to exhibit larger discrepancies.

In this thesis the Car-Parrinello scheme is mainly used for "simulated annealing" rather than for MD. Here, a damping term is introduced into equation 2.25 so that at every timestep energy is removed from the system. Allowing the ions to evolve as in a standard MD run leads to "damped CPMD", where the joint electron-ions system converges to its nearest low-energy minimum and thus provides a method of determining equilibrium geometries. Alternatively, if the ions are kept fixed the damped equation 2.25 yields the ground-state electron density.

2.3.3 Temperature control with thermostats

In a standard molecular dynamics simulation one works in the microcanonical ensemble, where the number of particles, energy and volume of the system is fixed (for CPMD the conserved energy includes the fictitious kinetic energy of the electrons). However it is more usual to take measurements on a system of constant temperature, where the probability of finding the system in a microstate of a particular energy is given by the Boltzmann factor evaluated at that energy [77]. The purpose of thermostats is to modify the behaviour of the MD run in order to mimic these constant temperature conditions.

A stochastic approach, employed in the Andersen thermostat, is to periodically rescale a selection of ionic velocities according to the Maxwell-Boltzmann distribution appropriate for that temperature [78]. An alternative is the Nosé-Hoover approach [79; 80], where yet more terms are added to the Lagrangian:

$$\mathcal{L}^T = \mathcal{L} + \frac{Q}{2}\dot{s}^2 - (3N+1)k_b T \ln s$$

Here Q is an effective mass (or frequency) of the thermostat. With this particular choice of terms, the average of a quantity taken over a long MD run tends to the statistical mechanical average of that quantity at temperature T [73].

2.4 Correlated electrons: LDA + Hubbard U

2.4.1 The LDA and fractional occupations

Above it was stated that the local-density approximation works rather well across a wide range of materials. Notable exceptions are systems containing atoms with unfilled d or f shells, i.e. strongly-correlated materials [81]. In particular, the energy of localised states is affected in DFT by the so-called self-interaction error, where the repulsive Hartree energy of an electron interacting with itself is not fully cancelled by the local-density approximation to exchange and correlation [82]. Rather than allowing individual electrons to occupy atomic-like d and f states, the LDA tends to spread out the charge through the partial occupation of states.

Schematically the behaviour is illustrated in Figure 2.2, considering a material consisting of two sites which each can be occupied by a maximum of two electrons. The lowest energy configuration has each site occupied by one elec-

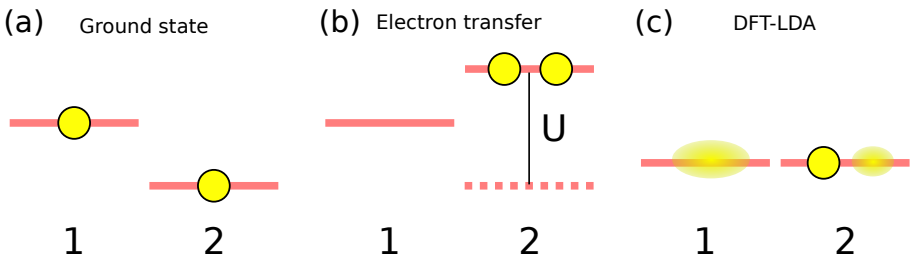

Figure 2.2: Schematic description of the problem of fractional occupations in DFT. A system consisting of two localised states may have the equilibrium configuration shown in (a), where each state is occupied by one electron. Forcing an electron from site **1** to **2** raises the energy of the state at **2** through the Coulomb repulsion between the electrons, with a penalty U. However the local-density approximation permits a partial occupation of both states, which lowers (raises) the energy at site **1** (**2**) until a new equilibrium is achieved.

tron. Supposing that an electron could be forced from site **1** to **2**, the Coulomb repulsion between the other electron on **2** raises the energy of the states localised at that site. The associated energy penalty is denoted U. However, the LDA permits a fractional transfer of an electron from **1** to **2**. Adding charge to **2** increases the Coulomb repulsion at this site but lowers the repulsive self-interaction at **1**; thus it is possible for the LDA to find a lower energy configuration based on the unphysical fractional occupation of sites **1** and **2**. Consequently, for certain materials (particularly transition metal oxides) the LDA fails to find the correct ground state density [83].

2.4.2 Introducing U corrections

In order to improve the description of localised states, the DFT+U method modifies the total energy functional (equation 2.3) by introducing a new piece, E_U [84–86]:

$$E_U\left[\{n^I_{mm'}\}\right] = E_{\text{Hub}}\left[\{n^I_{mm'}\}\right] - E_{\text{dc}}\left[\{\text{Tr}\ [\mathbf{n^I}]\}\right] \tag{2.27}$$

The on-site density matrix $\mathbf{n^I}$ is defined in terms of projection orbitals located on a particular atom I:

$$n^I_{mm'} = \sum_i f_i \langle m|\psi_i\rangle\langle\psi_i|m'\rangle \tag{2.28}$$

where each ψ_i is a Kohn-Sham state with occupation f_i=0 or 1. The projector orbitals $|m\rangle$ are centred on the atom I; m stands for a whole set of quantum numbers. The choice of projectors is in some senses arbitrary; a standard approach is to use pseudo-atomic orbitals.

Equation 2.27 consists of two terms. E_{Hub} takes into account the explicit Coulomb repulsion between the on-site orbitals and is written in terms of an angular expansion of the Coulomb interaction [87]. The term corresponding to the $L = 0$ part of the angular expansion can be expressed in terms of the parameter U, while higher order moments are described by another parameter J. The complication is that the LDA exchange-correlation energy already contains some of the interaction described by E_{Hub}; to avoid double counting, this contribution E_{dc} must be removed. Since E_{XC} is not known analytically, determining E_{dc} is non-trivial.

2.4.3 DFT+U kept simple

Already it might be noted that there are quite a few choices to be made in the DFT+U approach, regarding the projectors, functional forms of the correction, and how to deal with the double counting. Indeed different flavours of DFT+U exist in the literature [85; 87; 88], which means care should always be taken in comparing different DFT+U calculations. There is a strong argument for keeping the model as simple as possible, given that an incomplete knowledge of E_{dc} will

always limit the exactness of any expression. The DFT+U implementation used in this thesis is that of Ref. 85 where only the spherically symmetric, $L = 0$ term of the Coulomb interaction is maintained. Then, the parameter J equals 0, and E_U becomes

$$E_U[\{\mathbf{n^I}\}] = \frac{U}{2}\sum_I \text{Tr}\,[\mathbf{n^I}(\mathbf{1} - \mathbf{n^I})] \tag{2.29}$$

The corresponding modification to the Kohn-Sham equation 2.5 is to introduce a new term δV_U, where

$$\delta V_U = \sum_{Imm'} \left[\frac{1}{2}\delta_{mm'} - n^I_{mm'}\right] U|m\rangle\langle m'| \tag{2.30}$$

In the context of Fig. 2.2 it is useful to consider projector orbitals that diagonalise the on-site density matrix (equation 2.28). Then, the contribution to the total energy from each atom is

$$\sum_m n^I_m(1 - n^I_m)$$

where $n^I_m \equiv n^I_{mm}$, and $0 \leq n_m \leq 1$. That is, there is an energy penalty for non-integer values of n_m, thus acting against the fractional occupation of Fig. 2.2. In terms of the Kohn-Sham eigenvalues, employing the same diagonal representation gives

$$\delta V_U = \sum_m \left[\frac{1}{2} - n^I_m\right] U|m\rangle\langle m|$$

which opens a gap of size U between occupied and unoccupied states.

Although methods exist for calculating U from first principles (Refs. 84, 85 and references therein) in this thesis it will be treated as an adjustable parameter. Precisely how U might be chosen will be addressed in Section 5.3.1.

2.5 Excitations in DFT

2.5.1 The ΔSCF method

The key quantity in DFT is the density of the electrons in their ground state. As such it may be supposed that DFT does not allow access to the excitation energies which are probed in photoemission experiments. However the lowest-energy transition observable in such experiments (neglecting ionic relaxation) is between the ground state of the N-electron system and the ground state of the $N \pm 1$ system. The energies required to excite these transitions are known as the ionisation potential (I.P.) and electron affinity (E.A.):

$$\text{I.P.} = E(N-1) - E(N) \tag{2.31}$$

$$\text{E.A.} = E(N) - E(N+1) \tag{2.32}$$

Since all energies in the above equations are ground-state quantities, it should be possible to use equation 2.8 for the N, $N+1$ and $N-1$-electron systems to obtain E and thus the I.P. and E.A. as total energy differences. Such an approach is known as the ΔSCF method [89]. The I.P. and E.A. allow access to the "quasiparticle gap" of a material, defined as

$$E_G = \text{I.P.} - \text{E.A.} = E(N-1) + E(N+1) - 2E(N) \tag{2.33}$$

In fact, it was realised that while DFT (as introduced by Hohenberg and Kohn) applied just to the electronic ground state, it is possible to generalise the theory so that it is valid for the energetically lowest state of a given symmetry [59].

This has led to the ΔSCF method being applied to neutral excitations as well as photoemission, for instance in probing the triplet excited state of functionalised C_{60} molecules [90].

2.5.2 Benchmarking ΔSCF for ionisation potentials

The accuracy of equation 2.31 in determining the I.P. can be illustrated by considering the test set of twelve molecules introduced in Ref. 91, including thiophene, porphyrins and C_{60}. For each case the geometry of the neutral molecule was optimised in DFT, treating exchange and correlation with the PBE functional [54], and then the I.P. evaluated from equation 2.31. The calculations were performed in periodic boundary conditions; when calculating the total energy of molecules with an electron added or removed, the spurious interaction between charged replicas was removed using the Martyna-Tuckerman truncation scheme introduced above [69].

The resulting calculated ionisation potentials are shown as the blue crosses in Figure 2.3. They are compared to the experimentally-measured values and state-of-the art *GW* calculations reported in Ref. 91 (the *GW* method is the subject of the following chapter). The ΔSCF method exhibits an impressive performance, calculating the I.P. over a 3 eV range with a mean average error (M.A.E.) with respect to experiment of 0.22 eV compared to 0.30 eV for the *GW* calculations [91]. Similarly in Ref. 92 a M.A.E. of 0.24 eV was determined for ΔSCF compared to 0.4 eV for the best *GW* calculations.

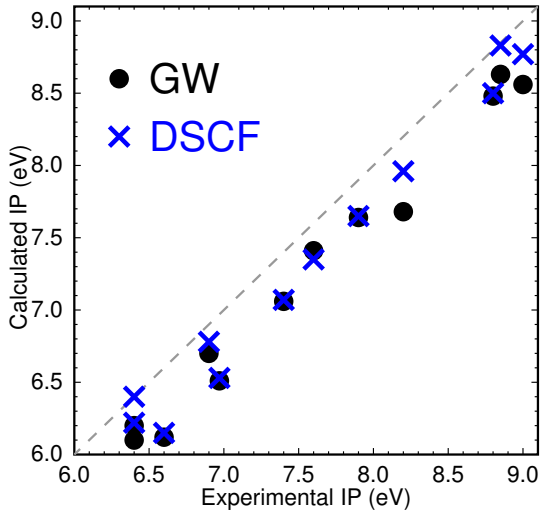

Figure 2.3: Ionisation potentials of the set of test molecules introduced in Ref. 91 calculated with the ΔSCF method (equation 2.31, blue crosses) compared to the *GW* calculations (black circles) and experimental measurements reported in that work. The mean average errors of the ΔSCF and *GW* calculations are 0.22 and 0.30 eV, respectively.

2.5.3 ΔSCF and core-level shifts

Equation 2.31 shows that the ΔSCF method allows access to the I.P. of the system, corresponding to the onset of photoemission observed in experiment. However the rest of the spectrum which originates from excited states of the $(N-1)$-electron system is theoretically inaccessible in DFT. This consideration has not prevented the development of constained-DFT approaches, which force the occupation of higher-energy Kohn-Sham states [93]. It should be noted that this method does not have a general theoretical justification, and suffers from the practical problem of the final result possibly being sensitive to how the constraint is defined.

An interesting exception is core-level photoemission (e.g. Ref. 94). In such an experiment one of the most tightly-bound electrons is removed from a particular atom in the system. After the photoemission event the $(N-1)$ system is obviously

in a highly excited state, and can be expected to decay through outer electrons cascading to lower energy states, emitting photons or Auger electrons [46]. But if these processes occur on a longer timescale than that of the initial photoelectron leaving the solid, it could be argued that the core-level photoemission experiment probes the energy of the system in a pseudo-ground state, where the outer electrons relax in the presence of the core-hole but do not decay.

Supposing that the above constitutes a theoretical justification of using ΔSCF for core-level photoemission, the practical consideration remains of how to ensure that a single core-electron state remains unoccupied in a DFT calculation of the total energy. Here the pseudopotential approach becomes very useful, because at the generation stage, the occupation of a particular state (say the spin up electron of the $1s$ orbital) can be forced to be zero, thus freezing the core-hole into the pseudo atom [95; 96]. This approach assumes the spatial distribution of the core-hole is independent of its surrounding environment, a reasonable approximation given how tightly bound the state is. By constrast in a DFT calculation incorporating the core-hole pseudopotential, the outer electrons will act to screen the positively charged hole; the change in screening depending on the atom's local environment will give rise to core-level shifts.

2.5.4 Practical calculation of core-level shifts

The scheme outlined in the previous section can be illustrated with the example of calculating the O $1s$ binding energies of acetic acid, CH_3COOH. The ball-and-stick representation of this molecule is shown in Figure 2.4. An O pseudopotential is generated in the configuration $1s2s^22p^4$, with the $n = 2$ shell in the valence. The valence charge Z of this pseudopotential is +7 (compared to +6 for a standard O pseudopotential).

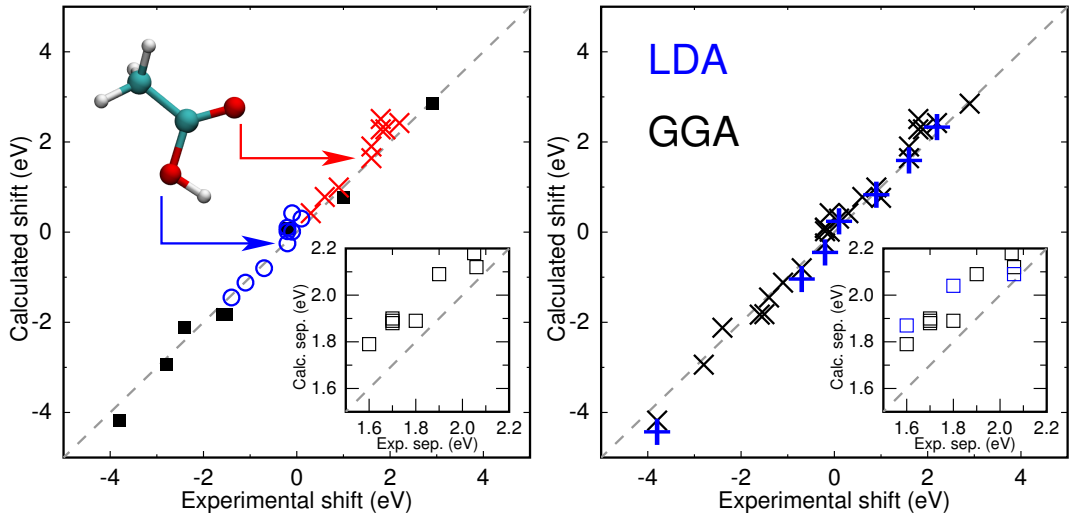

Figure 2.4: O 1*s* shifts for test molecules (c.f. Table 2.1) calculated with the PBE functional (left) and within the LDA (right). In the left plot the shifts are classified into shifts of carbonyl (red crosses) and hydroxyl (blue circles) O atoms of molecules containing carboxylic acid (COOH) groups, and the shifts of molecules not containing COOH groups (black squares). The insets of the figure compares the calculated and experimental differences in carbonyl/hydroxyl shifts for the COOH molecules. The ball-and-stick model of acetic acid is also shown. The experimental shifts are from Refs. 97 and 98.

Next, three DFT calculations are performed to obtain the total energies of (a) the neutral molecule (i.e. where both O atoms are represented by standard pseudopotentials), (b) acetic acid with the core-hole pseudopotential used for the carbonyl O atom (double-bonded to C, red line in Fig. 2.4) and (c) acetic acid with the core-hole pseudopotential used for the hydroxyl O atom (bonded to C and H, blue line in Fig. 2.4). The three energies are labelled E^0, E_C^+ and E_H^+, respectively. Then the O $1s$ binding energies E_C^{1s} and E_H^{1s} are obtained as

$$E_C^{1s} = E_C^+ - E^0 + \Delta_{PP}$$
$$E_H^{1s} = E_H^+ - E^0 + \Delta_{PP}$$

A new quantity has appeared, Δ_{PP}. This part reflects the fact that pseudopotentials miss the contribution to the total energy from the core electrons. In principle this quantity could be extracted directly from the all-electron calculations used to generate the pseudopotential. However since normally it is core-level shifts that are of interest, e.g. $E_C^{1s} - E_H^{1s}$, the difference tends to cancel. Alternatively one can choose Δ_{PP} to align the calculated shifts to a reference energy (which actually mimics the experimental procedure of aligning to a reference peak).

Figure 2.4 and Table 2.1 give the O $1s$ shifts calculated for a set of test molecules compared to experimental measurements reported in Refs. 97 and 98. The O $1s$ binding energies are given with respect to that of the H_2O molecule, which is 539.9 eV experimentally [97]. Here the convention is a negative "shift" implies a higher binding energy, i.e. it costs more energy to remove a $1s$ electron from O_2 than H_2O.

The agreement between the ΔSCF calculations and experimental O $1s$ binding energies is typically very good, with a mean average error of 0.31 eV over a

Table 2.1: O 1*s* shifts of test molecules (c.f. Fig. 2.4). All values are referenced to the shift of the H_2O molecule. For molecules containing carboxylic acid groups the shifts of the carbonyl O atoms and of the hydroxyl O atoms are reported separately. In the other cases where a molecule has more than one O atom, the relevant atom is indicated in boldface. The experimental data are from Refs. 97 and 98.

Molecule	Theory (eV)	Experiment (eV)
H_2O	0.00	0.00
O_2	-4.18	-3.8
N_2O	-1.82	-1.5
$F_3C\mathbf{O}\mathbf{O}\mathbf{O}CF_3$ (average)	-1.83	-1.6
$F_3CO\mathbf{O}OCF_3$	-2.94	-2.8
N-(OH)-2-Pyridone (CO)	2.85	2.9
N-(OH)-2-Pyridone (OH)	0.09	-0.2
CF_3NO	-2.12	-2.4
HCOOH[a] (CO)	0.99	0.9
HCOOH (OH)	-0.80	-0.7
CH_3COOH[b] (CO)	1.64	1.6
CH_3COOH OH	-0.25	-0.2
CH_3CH_2COOH[c] (CO)	1.90	1.6
CH_3CH_2COOH (OH)	0.01	-0.1
C_6H_5OH[d]	0.76	1.0
$F_2CHCOOH$[e] (CO)	0.78	0.6
$F_2CHCOOH$ (OH)	-1.12	-1.1
CF_3COOH[f] (CO)	0.42	0.3
CF_3COOH (OH)	-1.45	-1.4
C_6H_5COOH[g] (CO)	2.42	2.2
C_6H_5COOH (OH)	0.30	0.1
$C_6H_4(COOH)_2$[h] (CO)	2.51	1.8
$C_6H_4(COOH)_2$ (OH)	0.42	-0.1
$C_6H_4(COOH)_2$[i] (CO)	2.28	1.9
$C_6H_4(COOH)_2$ (OH)	0.10	-0.2
$C_6H_4(COOH)_3$[j] (CO)	2.28	1.8
$C_6H_4(COOH)_3$ (OH)	0.02	-0.2

[a]Formic acid
[b]Acetic acid
[c]Propionic acid [d]Phenol
[e]Difluoroacetic acid
[f]Trifluoroacetic acid
[g]Benzoic acid
[h]Phthalic acid
[i]Isophthalic acid
[j]Terephthalic acid

7 eV energy range. Particularly relevant to this thesis are the binding energies of hydroxyl and carbonyl O atoms in carboxylic acid groups, (blue circles and red crosses, respectively) and the differences between these shifts (inset of Fig. 2.4). Here the agreement with experiment is even better, with a M.A.E. of 0.16 eV (note the difference in scales between the two plots).

Also shown in Fig. 2.4 is a comparison of core-level shifts calculated using the PBE [54] functional or in the LDA [53]. The two methods give similar results, with a slight improvement for PBE. In fact, it will be shown in Chapter 4 that the difference can probably be attributed to differences in the relaxed molecular geometries obtained with the two approaches rather than in the calculation of total energy differences.

Finally, it is worth pointing out that obtaining E^+ is a calculation on a charged system, which as for valence ΔSCF presents a problem in periodic boundary conditions. For the calculations presented above E^+ was calculated for a number of simulation cell sizes, fitted to a Makov-Payne expansion [68] and then extrapolated to the limit of infinite cell size. Truncating the Coulomb interaction is also possible [69]. Although the absolute binding energies converge slowly with increasing simulation cell size, differences converge far more quickly. For instance, E_C^+ calculated for formic acid changes by 0.25 eV on increasing the simulation cell length from 9 to 27 Å, while $E_C^+ - E_H^+$ changes by less than 0.02 eV. This observation is useful in the context of extended systems, where the Coulomb interaction cannot be truncated. Alternatively a recent work employed arguments based on classical electrostatics in order to correct for the periodic interaction in extended systems [99].

2.5.5 ΔSCF and the derivative discontinuity

ΔSCF also provides insight into the "band gap problem"; that is, the eigenvalue difference between the highest-energy occupied and lowest-energy unoccupied Kohn-Sham states is generally smaller than the band gap measured in experiments. Taking the definition of the quasiparticle gap (equation 2.33) and the expression for the DFT total energy (equation 2.8) gives the band gap in terms of Kohn-Sham eigenvalues:

$$\begin{aligned} E_G &= \varepsilon_{N+1}^N - \varepsilon_N^N + \sum_i^{N+1} \Delta\varepsilon_i^L + \sum_i^{N-1} \Delta\varepsilon_i^H \\ &\quad -E_H[\Delta\rho^L] - E_H[\Delta\rho^H] + \int V_H^N(\mathbf{r})(\Delta\rho^H(\mathbf{r}) - \Delta\rho^L(\mathbf{r}))d\mathbf{r} \\ &\quad +E_{XC}[\rho^{N+1}] + E_{XC}[\rho^{N-1}] - 2E_{XC}[\rho^N] \\ &\quad -\int V_{XC}^{N+1}(\mathbf{r})\rho^{N+1}(\mathbf{r})d\mathbf{r} - \int V_{XC}^{N-1}(\mathbf{r})\rho^{N-1}(\mathbf{r})d\mathbf{r} + 2\int V_{XC}^N(\mathbf{r})\rho^N(\mathbf{r})d\mathbf{r} \end{aligned} \tag{2.34}$$

The new quantities introduced above reflect that on adding or removing an electron, the density changes. For instance, removing an electron changes the density from ρ^N to ρ^{N-1}:

$$\rho^N \to \rho^{N-1} = \rho^N - \Delta\rho^H$$

Accordingly, the eigenvalues, exchange-correlation potential and energy and the Hartree contributions all change, e.g.:

$$\begin{aligned} \varepsilon_i^N &\to \varepsilon_i^{N-1} = \varepsilon_i^N + \Delta\varepsilon^H \\ V_{XC}^N &\to V_{XC}^{N-1} \end{aligned}$$

The above emphasises that with or without the local-density approximation, the Kohn-Sham gap of the neutral system $\varepsilon_{N+1}^N - \varepsilon_N^N$ does not generally correspond to the real gap. As such it could be claimed that the band gap problem is not a problem at all; the two quantities should not be expected to agree. However in the limit of an infinite system (e.g. a periodic crystal) removing an electron produces only an infinitesimal change in density. As such, *if all the functionals in equation 2.8 vary smoothly with density*, on taking the difference between $E(N)$ and $E(N-1)$ all terms cancel except one contribution in the sum over eigenvalues; that is, the I.P. of an infinite system is $-\varepsilon_N$, the highest occupied eigenvalue. The same argument for adding an electron finds that, providing the condition of smoothly-varying functionals is satisfied, the DFT prediction of the band gap of an infinite system is indeed the Kohn-Sham gap.

The above argument can be verified from equation 2.34 by expressing the eigenvalue shifts in terms of perturbation theory. Alternatively the relation of the highest occupied Kohn-Sham eigenvalue to the ionisation potential is given by Janak's theorem [100], which considers fractionally changing the occupation f of the highest-energy state between 0 and 1:

$$E(N-1) - E(N) = \int_1^0 \varepsilon_N(f) df \tag{2.35}$$

The fact that ε_N has an argument f emphasises that, as the population of a state changes, so does the density; consequently the eigenvalue solutions of the self-consistent Kohn-Sham equations also change. Again, in the limit of an infinite system the perturbation to the density is infinitesimal, so equation 2.35 might be expected to yield $-\varepsilon_N$.

The apparent failure of DFT is found in the fact that real calculations only use an approximate exchange-correlation functional, which varies continuously as one changes the density. In fact, Refs. 101–103 established that the exact exchange-correlation potential varies discontinuously with ρ, such that

$$\Delta = \lim_{N\to\infty} \left[V_{XC}^{N+1}(\mathbf{r}) - V_{XC}^{N}(\mathbf{r}) \right] \tag{2.36}$$

where Δ is the "derivative discontinuity". Accordingly the exact DFT expression for the quasiparticle gap consists of the Kohn-Sham gap plus this contribution. Calculating Δ is highly non-trivial and has only been performed in a few cases; the calculations of Ref. 103 found a value of 0.58 eV for Δ in silicon.

Interestingly, reconciling ΔSCF with the derivative discontinuity has proved contentious in the past, e.g. for silicon nanoclusters [104; 105]. Consequently benchmarks like those in Fig. 2.3 are an important and necessary check of the validity of ΔSCF when using the method to describe new systems.

2.6 Conclusions

This chapter has covered a wide range of topics, from the fundamental background of density-functional theory to its practical implementation and applications. While the coverage is by no means exhaustive it provides the necessary background to the techniques employed in this thesis. In particular, the Coulomb truncation scheme and ΔSCF method will be used to consider both core and valence photoemission from molecules, while the DFT+U method will form the basis of an investigation of the bulk properties of TiO_2.

The failure of DFT to predict the fundamental band gap was ascribed to the

lack of the derivative discontinuity in the local-density approximation. Yet even with the exact exchange-correlation functional the Kohn-Sham eigenvalues do not give the full excitation spectrum of a system in general. In order to access this quantity it is necessary to go beyond DFT, which is the subject of the next chapter.

Chapter 3

Electronic structure of excited states in the GW approach

This chapter serves as an abridged introduction to the GW approximation. The electronic Green's function contains a vast amount of information including the energies of the excited states probed in photoemission experiments. Closely related is the spectral function, which provides the bridge between the Green's function and experimentally-measured spectra. Both quantities depend intimately on the self-energy operator, Σ, and the purpose of the GW method is to calculate this.

In the literature, GW occupies an interesting position. Its roots are in many-body condensed matter physics, which is the subject of many detailed textbooks (e.g. Refs. 106–109). These treatments tend to deal with idealised systems like the homogeneous electron gas. To find details of the application of GW to real materials one can go to contemporary reviews [110–113] which place less emphasis on the fundamental derivations and more on later developments. There are also works which focus on the computational details of GW calculations, discussing practical limitations and bottlenecks [114–116].

Here I provide a mix of all of these aspects. Sections 3.1 and 3.3 focus on the theoretical background of the Green's function and self-energy. Section 3.2 introduces the quasiparticle equation, which allows access to the energies of excited states, while Section 3.5 describes the link to photoemission. The practical steps of the GW calculations performed in this thesis are described in Section 3.4.

3.1 Green's functions

3.1.1 Definition of the Green's function

A key quantity in the theory of excited states is the time-ordered electronic Green's function, defined as:

$$\begin{aligned} G(x,t;x't') &= -i\theta(t-t')\langle N|\Psi(x,t)\Psi^\dagger(x',t')|N\rangle \\ &\quad +i\theta(t'-t)\langle N|\Psi^\dagger(x',t')\Psi(x,t)|N\rangle \end{aligned} \tag{3.1}$$

Here, t is time and x is a composite index which includes both a particle's spin σ and its position $\mathbf{r}$. The Heaviside function $\theta(\tau) = 1$ for $\tau > 0$ and 0 otherwise. $|N\rangle$ is the electronic many-body ground state. The quantum field operators $\Psi^\dagger(x)$ and $\Psi(x)$ describe the creation or removal of a particle of a given spin at a point in space, through:

$$\Psi^\dagger(x) = \sum_m \psi_m^*(x) c_m^\dagger \tag{3.2}$$

$$\Psi(x) = \sum_m \psi_m(x) c_m \tag{3.3}$$

where the ψ_m's are a complete set of single-particle orbitals with associated creation/destruction operators $c_m^\dagger$ and c_m. The time dependence of the field operators is obtained in the Heisenberg picture:

$$\begin{aligned} \Psi^\dagger(x,t) &= e^{iHt}\Psi^\dagger(x)e^{-iHt} \\ \Psi(x,t) &= e^{iHt}\Psi(x)e^{-iHt} \end{aligned} \tag{3.4}$$

where H is the Hamiltonian of the system.

Loosely speaking, for $t > t'$, the Green's function can be thought of as the overlap of a state with an electron added at point $\mathbf{r}'$ at time t' with one where the electron is added at a point $\mathbf{r}$ at a subsequent time t. For $t' > t$, G describes the propagation of a hole.

3.1.2 Energy structure of the Green's function

The usefulness of the Green's function is seen in its energy-space representation. The first term in equation 3.1 can be written as

$$\langle N|\Psi(x,t)\Psi^\dagger(x',t')|N\rangle = e^{iE_N^0 t}e^{-iE_N^0 t'}\langle N|\Psi(x)e^{-iHt}e^{iHt'}\Psi^\dagger(x')|N\rangle \tag{3.5}$$

since the ground state obeys $H|N\rangle = E_N^0|N\rangle$. Next, one considers the complete set of states of an M-particle system which are eigenstates of H, $H|M,j\rangle = E_M^j|M,j\rangle$, which obey the completeness relation

$$\sum_j |M,j\rangle\langle M,j| = 1 \tag{3.6}$$

Inserting these states into equation 3.5 allows the operators in the exponentials to be replaced with eigenenergies, which then can be brought outside the integral:

$$\langle N|\Psi(x,t)\Psi^\dagger(x',t')|N\rangle = \sum_j e^{i(E_N^0 - E_M^j)(t-t')}\langle N|\Psi(x)|M,j\rangle\langle M,j|\Psi^\dagger(x')|N\rangle \tag{3.7}$$

Following the same procedure for the second term in equation 3.1 gives

$$\langle N|\Psi^\dagger(x',t')\Psi(x,t)|N\rangle = \sum_j e^{i(E_N^0 - E_M^j)(t'-t)}\langle N|\Psi^\dagger(x')|M,j\rangle\langle M,j|\Psi(x)|N\rangle. \tag{3.8}$$

There are two points to note from equations 3.7 and 3.8. First, time only enters as a difference, $\tau = t - t'$; i.e. the only important quantity is the time between addition and removal events, not the absolute time when the first event occurs. This time invariance makes an energy-representation a natural choice for the Green's function. Second, the matrix elements only make sense if $M = N+1$ for 3.7 and $M = N - 1$ for 3.8, since the field operators change the particle numbers by ± 1. Accordingly, G can be written as

$$\begin{aligned} G(x, x'; \tau) &= -i\theta(\tau) \sum_j e^{i(E_N^0 - E_{N+1}^j)\tau} \times \\ &\quad \langle N|\Psi(x)|N+1, j\rangle\langle N+1, j|\Psi^\dagger(x')|N\rangle \\ &\quad +i\theta(-\tau) \sum_j e^{-i(E_N^0 - E_{N-1}^j)\tau} \times \\ &\quad \langle N|\Psi^\dagger(x')|N-1, j\rangle\langle N-1, j|\Psi(x)|N\rangle. \end{aligned} \tag{3.9}$$

The next step is to define a Fourier transform (FT) of the Green's function as

$$G(x, x'; E) = \int_{-\infty}^{+\infty} d\tau e^{iE\tau} G(x, x'; \tau). \tag{3.10}$$

A complication which arises is that, for the FT to be well-defined, G must decay at large $|\tau|$. In order to ensure convergence, an infinitesimal imaginary part $\pm i\eta$ is added to E, which forces the integrand to decay (alternative derivations attribute this factor to the FT of the Heaviside functions). The sign preceeding the infinitesimal changes depending on whether it is the hole or electron part of the G being considered, since $\theta(\pm\tau)$ ensures G is cut off at the other limit.

Accordingly,

$$\begin{aligned} G(x,x';E) &= -i\sum_j \int_0^\infty e^{i(E_N^0-E_{N+1}^j)\tau} e^{iE\tau} e^{-\eta\tau} d\tau \times \\ &\quad \langle N|\Psi(x)|N+1,j\rangle\langle N+1,j|\Psi^\dagger(x')|N\rangle \\ &\quad +i\sum_j \int_{-\infty}^0 e^{-i(E_N^0-E_{N-1}^j)\tau} e^{iE\tau} e^{\eta\tau} d\tau \times \\ &\quad \langle N|\Psi^\dagger(x')|N-1,j\rangle\langle N-1,j|\Psi(x)|N\rangle \end{aligned} \tag{3.11}$$

which after performing the integrals over τ gives:

$$\begin{aligned} G(x,x';E) &= \sum_j \frac{\langle N|\Psi(x)|N+1,j\rangle\langle N+1,j|\Psi^\dagger(x')|N\rangle}{E-(E_{N+1}^j-E_N^0)+i\eta} \\ &\quad +\sum_j \frac{\langle N|\Psi^\dagger(x')|N-1,j\rangle\langle N-1,j|\Psi(x)|N\rangle}{E-(E_N^0-E_{N-1}^j)-i\eta} \end{aligned} \tag{3.12}$$

Equation 3.12 is very important. It shows that G has poles in the complex E plane when

$$E = E_{N+1}^j - E_N^0 - i\eta$$

and

$$E = E_N^0 - E_{N-1}^j + i\eta.$$

That is, the poles of the Green's function defined on the N particle system occur at the excited and ground-state energies of the $N \pm 1$ system, i.e. one where a single electron has been added or removed.

3.1.3 The non-interacting Green's function

It will be useful to consider the Green's function of a system where the electrons do not interact with each other. Then, the Hamiltonian can be written as

$$H = \sum_m \varepsilon_m c_m^\dagger c_m$$

which leads to the following forms for the field operators:

$$\Psi(x,t) = \sum_m e^{-i\varepsilon_m t}\psi_m(x)c_m$$

$$\Psi^\dagger(x,t) = \sum_m e^{i\varepsilon_m t}\psi_m^*(x)c_m^\dagger$$

Since each state can only be occupied by one electron (Pauli exclusion) any terms in the Green's function which involve $c_n^\dagger|N\rangle$, will be nonzero only if the state n is not occupied in the ground state. Similarly, $c_n|N\rangle$ will require the state n to be occupied for a nonzero contribution. Therefore the non-interacting Green's function (G^0) in the time domain is:

$$\begin{aligned} G^0(x,x';\tau) &= -i\theta(\tau)\sum_c e^{-i\varepsilon_c\tau}\psi_c^*(x')\psi_c(x) \\ &\quad +i\theta(-\tau)\sum_v e^{-i\varepsilon_v\tau}\psi_v^*(x')\psi_v(x) \end{aligned} \tag{3.13}$$

where c and v correspond to unoccupied (conduction) and occupied (valence) states. The corresponding expression in energy-space is:

$$G^0(x,x';E) = \sum_c \frac{\psi_c^*(x')\psi_c(x)}{E-\varepsilon_c+i\eta} + \sum_v \frac{\psi_v^*(x')\psi_v(x)}{E-\varepsilon_v-i\eta} \tag{3.14}$$

which again highlights the pole structure of the Green's function corresponding to the excitation energies of the system.

3.1.4 Equation of motion

From the analysis above it is clear that determining the Green's function of a system would be highly desirable, since it contains a large amount of information. This is realised by considering the time evolution of G, $\frac{\partial}{\partial t}G(x,t;x',t')$, which in turn is governed by the time evolution of the field operators:

$$i\frac{\partial}{\partial t}\Psi(x,t) = -[H,\Psi(x)](t)$$

Anticipating the electron gas, the Hamiltonian H is divided into the single-particle part $h_0(x)$ (kinetic energy, local ionic potential) and the electron-electron interaction $v(x,x')$. The second-quantised form of this Hamiltonian is

$$\begin{aligned} H &= \int dx\Psi^\dagger(x)h_0(x)\Psi(x) + \frac{1}{2}\int dxdx'\Psi^\dagger(x)\Psi^\dagger(x')v(x,x')\Psi(x')\Psi(x) \\ &= H_0 + H_1 \end{aligned}$$

Differentiating equation 3.1, employing the anticommutator relation

$$\left\{\Psi(x),\Psi^\dagger(x')\right\} = \delta(x-x')$$

and using that the derivative of a θ-function is a δ-function gives:

$$\begin{aligned} & i\frac{\partial}{\partial t}G(x,t;x't') - h_0(x)G(x,t;x't') \\ +i\int dx''v(x,x'')G_2(x,t;x't',x'',t,x''t^+) &= \delta(x-x')\delta(t-t') \end{aligned} \qquad (3.15)$$

Here a new quantity has been introduced, the two particle Green's function G_2 (see Ref. 107 page 128 for a definition); $t^+ \equiv t+\delta$, where δ is a positive infitesimal.

G_2 is an unwieldy object. However, it can be related to G by considering the response of the system to an external applied potential $\phi(x,t)$. It is convenient to introduce a labelling system of indices such that $G(1,2) \equiv G(x_1,t_1;x_2,t_2)$ etc., while $1^+ \equiv (x_1, t_1+\delta)$. The Coulomb interaction, being instantaneous, is

$$v(1,2) = v(x_1,x_2)\delta(t_1-t_2).$$

Taking a functional derivative of G with respect to the applied potential ϕ gives

$$-\frac{\delta G(1,2)}{\delta\phi(3)} = G_2(1,2,3,3^+) - G(1,2)G(3,3^+) \tag{3.16}$$

which allows G_2 to be replaced in the equation of motion:

$$\begin{aligned} i\frac{\partial}{\partial t_1}G(1,2) - h_0(1)G(1,2) + i\int d3v(1,3)G(3,3^+)\ G(1,2) \\ -i\int d3v(1,3)\frac{\delta G(1,2)}{\delta\phi(3)} = \delta(1-2) \end{aligned} \tag{3.17}$$

There is now a term containing $G(3,3^+)$. Inserting the time arguments $t_3, t_3+\delta$ into the original definition of the Green's function gives

$$\begin{aligned} G(3,3^+) &= i\langle N|e^{iHt_3}\Psi^\dagger(x_3)\Psi(x_3)e^{-iHt_3}|N\rangle \\ &= i\rho(3) \end{aligned} \tag{3.18}$$

where $\rho(3)$ is the electronic density. Thus the term can be written as

$$i \int d3v(1,3)G(3,3^+)\ G(1,2) = -\int d3v(1,3)\rho(3)\ G(1,2) = -V_H(1)G(1,2) \tag{3.19}$$

where V_H is the Hartree potential,

$$V_H(1) = \int d3v(1,3)\rho(3)$$

3.1.5 Introducing the self-energy

The final term of equation 3.17 containing the functional derivative can be rewritten by first defining an inverse to G:

$$\int G^{-1}(1,3)G(3,2)d3 = \delta(1-2) \tag{3.20}$$

Trivially $\frac{\delta(G^{-1}G)}{\delta\phi} = 0$, so employing the chain rule and applying another G gives

$$\frac{\delta G(1,2)}{\delta\phi(3)} = -\int d4d5G(1,4)\frac{\delta G^{-1}(4,5)}{\delta\phi(3)}G(5,2)$$

which means

$$\begin{aligned} -i\int d3v(1,3)\frac{\delta G(1,2)}{\delta\phi(3)} &= i\int d3d4d5v(1,3)G(1,4)\frac{\delta G^{-1}(4,5)}{\delta\phi(3)}G(5,2) \\ &= -\int d3\Sigma(1,3)G(3,2) \end{aligned} \tag{3.21}$$

where

$$\Sigma(1,3) = -i\int d4d5v(1,4)G(1,5)\frac{\delta G^{-1}(5,3)}{\delta\phi(4)} \tag{3.22}$$

or, in longhand notation,

$$\begin{aligned}\Sigma(x_1,t_1;x_3t_3) &= -i\int dx_4dt_4dx_5dt_5 \\ &\quad v(x_1,x_4)\delta(t_1-t_4)G(x_1,t_1,x_5,t_5)\frac{\delta G^{-1}(x_5,t_5;x_3,t_3)}{\delta\phi(x_4,t_4)}\end{aligned}$$

The quantity $\Sigma(1,3)$ is called the self-energy. Like the exchange-correlation potential V_{XC} in DFT, it contains the part of the Coulomb interaction not accounted for by the Hartree potential. Unlike V_{XC} however the self-energy is non-local, complex, and energy-dependent. As the next section shows, constructing Σ and solving for the equation of motion gives the excited-state energies of the system.

3.2 The quasiparticle equation

3.2.1 Energy-space representation

Inserting the self-energy Σ and Hartree potential V_H into the equation of motion of the Green's function (eq. 3.15) gives

$$\begin{aligned}i\frac{\partial}{\partial t}G(x,t;x',t') - [h_0(x)+V_H(x,t)]G(x,t;x't') \\ -\int dx''\Sigma(x,t;x''t'')G(x'',t'';x',t') &= \delta(x-x')\delta(t-t') \quad (3.23)\end{aligned}$$

Previously it was noted that for time-independent Hamiltonians, only differences in time $\tau = t - t'$ were important, which motivates moving to an energy-space representation. Employing the Fourier transform defined in equation 3.10 on all

quantities yields

$$\begin{aligned}(E - [h_0(x) + V_H(x)])\, G(x, x'; E) \\ - \int dx'' \Sigma(x, x''; E) G(x'', x'; E) \quad &= \quad \delta(x - x')\end{aligned} \tag{3.24}$$

Now, returning to equation 3.12 for the Green's function in energy-space, introducing the shorthand quantities

$$f_j^+ = \langle N|\Psi(x)|N+1, j\rangle$$

$$f_j^- = \langle N-1|\Psi(x)|N\rangle$$

and

$$E_j^+ = E_{N+1}^j - E_N^0$$

$$E_j^- = E_N^0 - E_{N-1}^j$$

allows the Green's function to be written as

$$G(x, x'; E) = \sum_j \frac{f_j^+(x) f_j^{*+}(x')}{E - E_j^+ + i\eta} + \sum_j \frac{f_j^-(x) f_j^{*-}(x')}{E - E_j^- - i\eta} \tag{3.25}$$

Substituting this representation into equation 3.24, multiplying through by the denominator and taking the limit $E \to E_j^{\pm}$ picks out a particular excited state j. The coefficient of $f^{*\pm}(x')$ must be zero, giving

$$[E_j h_0(x) + V_H(x)]\, f_j(x) - \int \Sigma(x, x''; E_j) f_j(x'') = 0$$

or

$$[h_0(x) + V_H(x)]\, f_j(x) + \int \Sigma(x, x'; E_j) f_j(x') dx' = E_j f_j(x) \tag{3.26}$$

where the ± has been dropped since the same equation describes both adding or removing a particle. Equation 3.26 is known as the quasiparticle equation. It looks rather similar to a Kohn-Sham equation, except for the more complicated properties of the self-energy. Indeed Σ is non-Hermitian, so that the energies E_j are generally complex and the f_j's are not orthonormal.

3.2.2 Matrix element representation

The equation of motion 3.24 provides one more useful piece of insight, which can be seen by projecting the Green's function onto single-particle orbitals:

$$G(x, x'; E) = \sum_{mm'} \psi_m(x)\psi^*_{m'}(x')G_{mm'}(E) \tag{3.27}$$

where

$$G_{mm'}(E) = \int dx\ dx' \psi^*_m(x)G(x, x'; E)\psi_{m'}(x') \tag{3.28}$$

For reasons that shall become clear, the projection orbitals ψ_m are chosen to be eigenstates of the following Hamiltonian:

$$\left[h_0(x) + V_H(x) + V'(x)\right]\psi_m(x) = \varepsilon_m\psi_m(x) \tag{3.29}$$

where as before $h_0(x)$ contains the electronic kinetic energy and electron-ion interaction. The new potential $V'(x)$ is intended to account approximately for the electron-electron interaction. Defining two further projections,

$$\Sigma_{mm'}(E) = \int dx\ dx' \psi^*_m(x)\Sigma(x, x'; E)\psi_{m'}(x')$$
$$V'_{mm'} = \int dx \psi^*_m(x)V'(x)\psi_{m'}(x)$$

allows the equation of motion to be re-written in matrix form:

$$(E - \varepsilon_m)G_{mm'}(E) - \sum_l \left[\Sigma_{ml}(E) - V'_{ml}\right] G_{lm'}(E) = \delta_{mm'} \tag{3.30}$$

No approximations have been made in obtaining equation 3.30. However, supposing that $V'(x)$ was chosen in such a way so that the sum along the off-diagonal elements $\Sigma_{ml}(E) - V'_{ml}$ could be neglected, equation 3.30 becomes diagonal and therefore easily invertible:

$$G_{mm}(E) \approx \frac{1}{E - (\varepsilon_m + \Sigma_{mm}(E) - V'_{mm})} \tag{3.31}$$

Equation 3.31 demonstrates an important concept. A non-interacting Green's function, constructed from the single-particle orbitals $\psi_m(x)$ using equation 3.14, will be diagonal in the mm' representation. But equation 3.30 shows that the interacting Green's function can also be diagonal in the same representation, if the arbitrary single-particle potential $V'(x)$ sufficiently mimics the full self-energy $\Sigma(x, x'; E)$. The difference is the position of the poles of the Green's function (energies of the excited states), which go from $E = \varepsilon_m$ in the noninteracting system to $E = \varepsilon_m + \Sigma_{mm}(E) - V'_{mm}$ in the diagonal approximation for the interacting Green's function.

Of course it is a rather large assumption that the real, static potential $V'(x)$ can sufficiently approximate the complex, energy-dependent and fully non-local self-energy $\Sigma(x, x'; E)$. One major breakthrough in the development of efficient calculations of excited states in a Green's function approach was the realisation that the exchange-correlation potential of DFT led to small off-diagonal elements for many semiconductors. However it is worth stressing that the choice of $V'(x)$

is not unique, a fact which will be exploited in Chapter 5.

3.3 Constructing the self-energy

The next step is to consider how Σ might actually be calculated through the so-called GW method. The approach given here follows that of Inkson [107] and Hedin's 1965 paper [117].

3.3.1 The dielectric function and screened Coulomb interaction

The quasiparticle equation contains a non-interacting Hamiltonian and the Hartree potential, both of which are well-defined (providing the density of the system is known). The remaining question is how to obtain the self-energy, which was defined in equation 3.22 in terms of the functional derivative of the inverse Green's function with respect to an external potential ϕ. It is possible to use the definition to produce an iterative expression for Σ, which is actually a power series in the Coulomb interaction v. The problem with this approach is that, in solids, the power series converges slowly. For instance, the first term in the series gives a Hartree-Fock exchange term, which is known to significantly overestimate the band gap of semiconductors.

A more useful approach is to recast the problem as a variation of the Green's function with the *total* potential, $V = \phi + V_H$. Perturbing the external potential by $\delta\phi$ will induce a rearrangement of charge $\delta\rho$, which therefore changes the Hartree potential:

$$\delta V(x_1, t_1) = \delta\phi(x_1, t_1) + \int v(x_1, x_2)\delta\rho(x_2, t_1)dx_2$$

The idea of a medium screening an external potential brings classical electrostatics to mind, and indeed the next step is to define an inverse dielectric function:

$$\epsilon^{-1}(x_1, t_1; x_2, t_2) = \frac{\delta V(x_1, t_1)}{\delta \phi(x_2, t_2)} \tag{3.32}$$

which in turn allows the definition of the screened Coulomb interaction W:

$$W(x_1, t_1; x_2, t_2) = \int \epsilon^{-1}(x_1, t_1; x_3, t_3) v(x_3, x_2) \delta(t_3 - t_2) dx_3 dt_3 \tag{3.33}$$

The dielectric function ϵ is also introduced as the inverse of ϵ^{-1}:

$$\int \epsilon(x_1, t_1; x_3, t_3) \epsilon^{-1}(x_3, t_3; x_2, t_2) dx_3 dt_3 = \delta(x_1 - x_2)\delta(t_1 - t_2) \tag{3.34}$$

which is used to define a polarisation propagator P

$$\epsilon(x_1, t_1; x_2, t_2) = \delta(x_1 - x_2)\delta(t_1 - t_2) - \int v(x_1, x_3)\delta(t_1 - t_3) P(x_3, t_3; x_2, t_2) dx_3 dt_3 \tag{3.35}$$

which, by comparing to the expression for ϵ^{-1}, gives

$$P(x_1, t_1; x_2, t_2) = \frac{\delta \rho(x_1, t_1)}{\delta V(x_2, t_2)} \tag{3.36}$$

3.3.2 Hedin's equations

The abstract definitions of the previous section, combined with equation 3.22, are sufficient to construct a recursive set of equations which connect G and Σ through the screened Coulomb interaction and dielectric function:

$$\Gamma(1, 2, 3) \;=\; -\frac{\delta G^{-1}(1, 2)}{\delta V(3)} \tag{3.37}$$

$$P(1,2) = -i\int G(1,3)\Gamma(3,4,2)G(5,1^+)d3d4 \tag{3.38}$$

$$\epsilon(1,2) = \delta(1-2) - \int v(1,3)P(3,2)d3 \tag{3.39}$$

$$W(1,2) = \int \epsilon^{-1}(1,3)v(3,2)d3 \tag{3.40}$$

$$\Sigma(1,2) = i\int d3d4G(1,3)W(1^+,4)\Gamma(3,2,4) \tag{3.41}$$

$$V(1) = \phi(1) - i\int v(1,3)G(3,3^+)d3 \tag{3.42}$$

Equations 3.37–3.41 are referred to as Hedin's equations, while the three-point function $\Gamma(1,2,3)$ is called the vertex function.

3.3.3 The GW approximation

Unfortunately, finding the set of functions which satisfy Hedin's equations and thus completely solving the many-body problem is not a realistic proposal. However the success of the formalism comes from using the equations to construct an approximate expression for Σ starting from the non-interacting case. If Σ is initially set to zero, equation 3.23 can be inverted and differentiated with respect to V to get the vertex function, which is a product of delta functions:

$$\Gamma_0(1,2,3) = \delta(1,3)\delta(2,3)$$

Inserting the delta functions into the expression for the polarisability gives

$$P_0(1,2) = -iG_0(1,2)G_0(2,1^+) \tag{3.43}$$

where the 0 subscript serves as a reminder that these are constructed in a non-interacting approximation. P_0 can then be used to construct ϵ and W, and thus

allow access to the first-order expression for Σ:

$$\begin{aligned} \Sigma_1(1,2) &= i\int d3d4 G_0(1,3)W_0(1^+,4)\Gamma_0(3,2,4) \\ &= iG_0(1,2)W_0(1^+,2) \end{aligned} \tag{3.44}$$

Equation 3.44 constitutes the G_0W_0 approximation to the self-energy. In principle one could use Σ_1 to construct a new Green's function and cycle through the equations again. Such an approach introduces new terms in the vertex function (vertex corrections), which greatly increase the complexity of the problem. However since the calculations in this thesis use the G_0W_0 approximation, it is appropriate to end the discussion here and instead move to the practicalities of GW calculations.

3.4 The G_0W_0 method

3.4.1 Reciprocal space and matrix element representations of Hedin's equations

The first step of a G_0W_0 calculation is to use equation 3.14 to construct a non-interacting Green's function. As discussed the choice of orbitals ψ_m used to construct the Green's function is somewhat arbitrary, but it makes sense to use those constructed from a potential V' which best approximates the true self-energy. The most widely-used choice is the exchange-correlation potential V_{XC} from DFT, so that the ψ_m's are Kohn-Sham states [118]. Then the polarisability

P_0 is obtained as

$$P_0(x_1, x_2; E) = \sum_{ln} \frac{\psi_l^*(x_2)\psi_l(x_1)\psi_n^*(x_1)\psi_n(x_2)(f_l - f_n)}{\varepsilon_l - \varepsilon_n - E + i\eta(f_l - f_n)} \tag{3.45}$$

where $f_l = 1$ if state l is occupied and zero otherwise. In crystalline systems it is more convenient to work in reciprocal co-ordinates rather than real space. Functions of two spatial co-ordinates like $P(x_1, x_2; E)$ are represented in terms of reciprocal lattice vectors G, G' and a wavevector inside the first Brillouin zone, q, i.e.

$$P(x_1, x_2; E) = \sum_{GG'q} e^{i(q+G)x_1} P_{GG'}(q, E) e^{-i(q+G')x_2} \tag{3.46}$$

In GW (dropping the 0 subscript on P),

$$P_{GG'}(q, E) = \sum_{lnk} \frac{\langle n, k|e^{-i(q+G)x}|l, k+q\rangle\langle l, k+q|e^{i(q+G')x}|n, k\rangle(f_l - f_n)}{\varepsilon_{lk+q} - \varepsilon_{nk} - E + i\eta(f_l - f_n)} \tag{3.47}$$

where l and n now refer to band indices and k to wavevectors of the states. The dielectric function is related to $P_{GG'}(q, E)$ through

$$\epsilon_{GG'}(q, E) = \delta_{GG'} - v_G(q) P_{GG'}(q, E) \tag{3.48}$$

where $v_G(q) = \frac{4\pi}{|q+G|^2}$ is the FT of the Coulomb potential. Unsurprisingly the inverse dielectric function is obtained by inverting the dielectric function, that is, looking for the matrix $\epsilon^{-1}(q, E)$ which satisfies

$$\sum_{G''} \epsilon_{GG''}(q, E)\epsilon^{-1}_{G''G'}(q, E) = \delta_{GG'} \tag{3.49}$$

while the screened Coulomb interaction W is given by

$$W_{GG'}(q,E) = \epsilon^{-1}_{GG'}(q,E)v_{G'}(q) \tag{3.50}$$

As an operator, the self-energy is most conveniently expressed in real time and space; however noting that it is the matrix element representation that is important in the quasiparticle picture, it is appropriate to consider the projection onto state $|m,k\rangle$, i.e.:

$$\begin{aligned}\Sigma_{mk,mk}(E) &= i\sum_{GG'ql}\langle m,k|e^{i(q+G)x}|l,k-q\rangle\langle l,k-q|e^{-i(q+G')x}|m,k\rangle \times \\ &\int \frac{W_{GG'}(q,E')e^{-iE'\delta}dE'}{E-E'-\varepsilon_{l,k-q}-(2f_l-1)i\eta}\end{aligned} \tag{3.51}$$

where the infinitesimal $\delta = 0^+$ has appeared due to the time ordering in Hedin's equation for Σ.

3.4.2 Σ_X and Σ_C

The self-energy Σ can usefully be divided into different contributions which display different convergence properties. A new quantity W^P is defined as

$$W^P_{GG'}(q,E) = \left[\epsilon^{-1}_{GG'}(q,E) - \delta_{GG'}\right] v_{G'}(q) \tag{3.52}$$

which separates out the contibution to the screened Coulomb interaction W from the bare Coulomb interaction v:

$$W_{GG'}(q,E) = \delta_{GG'}v_G(q) + W^P_{GG'}(q,E) \tag{3.53}$$

The first term is independent of energy. Its contribution to equation 3.51 can be evaluated by performing the energy integral in the complex E' plane, where the $e^{-iE'\delta}$ requires that the contour is closed in the negative half plane. Therefore only the residues from the poles lying below the real axis contribute to the integral, i.e. the contributions from the states l which are occupied. This part of the self-energy is denoted Σ_X, where

$$\langle m,k|\Sigma_X|m,k\rangle = -\sum_{Gq}\sum_{v}\left|\langle m,k|e^{i(q+G)x}|v,k-q\rangle\right|^2 v_G(q) \tag{3.54}$$

where v stands for occupied states only. The "X" stands for exchange, since in real space Σ_X has the form

$$\Sigma_X(x,x') = -\sum_{v}\frac{\psi_v(x)\psi_v^*(x')}{|x-x'|}$$

i.e. the exchange term which appears in the Hartree-Fock equations.

Equation 3.54 only requires a sum over one set of G vectors, has no energy dependence, and only has contributions from occupied states. As such it is relatively inexpensive to evaluate. The remaining contribution to the self-energy is termed the correlation part Σ_C and is more challenging to obtain.

3.4.3 Plasmon pole models

In principle, equations 3.47–3.51 provide the framework of calculating Σ with no further approximations required. In practice, a numerical evaluation of the energy convolution in equation 3.51 requires the calculation of W for a grid of frequencies. Each energy calculation requires constructing and then inverting the dense matrix ϵ; furthermore the zeros in the denominator of the integrand in

3.51 indicate that a fine grid of frequencies would be required to obtain good convergence.

Different methods of dealing with this problem exist. A generally desirable approach is to move the calculation of W^P from real to imaginary frequencies, where it is a much smoother function. For instance the contour deformation approach expresses the energy integral in terms of an integral along the imaginary axis with additional contributions from poles of the Green's function [119]. Alternatively Padé approximants can be used to construct the real axis behaviour of W^P from imaginary-energy calculations, with the integral for Σ subsequently performed along the real axis [120; 121], or Σ can be calculated for imaginary frequencies and then continued onto the real axis [122; 123].

While these methods are growing in popularity, approaches invoking plasmon-pole approximations (PPAs) are still the most common [118; 124; 125]. The fundamental premise of these approaches is that, since W^P is integrated over all frequencies in obtaining Σ, it may be sufficient to replace W^P with a model function which reproduces the most important features of the interaction. The PPA used in this thesis is based on that introduced by Hybertsen and Louie [118], who noted that full calculations of the dielectric matix $\epsilon_{GG'}(q, E)$ showed Fourier components that exhibited single peaks, or fluctations about zero. Accordingly they introduced a PPA where each component of the inverse dielectric matrix had poles of strength $\Omega^2_{GG'}(q)$ at frequencies $\pm\tilde{\omega}_{GG'}(q)$,i.e.

$$\epsilon^{-1}_{GG'}(q,\omega) = \delta_{GG'} + \frac{\Omega^2_{GG'}(q)}{\omega^2 - \tilde{\omega}^2_{GG'}(q)} \tag{3.55}$$

Here $\omega = \frac{E}{\hbar}$. The great advantage of this approach is that, since W^P now has a well-defined functional form the energy convolution can be carried out analytically

(as for Σ_X), yielding

$$\langle m,k|\Sigma_C(E)|m,k\rangle = \sum_{GG'q}\sum_{l}\langle m,k|e^{i(q+G)x}|l,k-q\rangle\langle l,k-q|e^{-i(q+G')x}|m,k\rangle \times \frac{v_{G'}(q)}{2\hbar\tilde{\omega}_{GG'}(q)}\frac{[\hbar\Omega_{GG'}(q)]^2}{[\hbar\omega-\varepsilon_{l,k-q}+(\hbar\tilde{\omega}_{GG'}(q)-i\eta)(2f_l-1)]} \quad (3.56)$$

In contrast to Σ_X there is a sum over both G and G', and also over all valence and conduction states l (see below).

The remaining question is how to determine the plasmon pole parameters $\tilde{\omega}_{GG'}(q)$ and $\Omega_{GG'}(q)$. In the Hybertsen-Louie approach, the model dielectric function is constrained to obey the f-sum rule so that a single calculation of ϵ^{-1} for the static case $\omega = 0$ is sufficient to determine all parameters. An alternative method is to note that since there are only two parameters, the model expression can be fitted to ϵ^{-1} calculated at two different frequencies. Generally the frequencies chosen are $\omega = 0$ and $\omega = i\omega_P$, where ω_P roughly matches the plasmon frequency of the system under study. This latter approach, (known as the Godby-Needs plasmon-pole model [125]) has the advantage of having more input data to fit, but no longer satisfies the f-sum rule.

Evaluating the relative merits of different plasmon pole models and their applications is an area of current research [126; 127]. In this thesis the Godby-Needs plasmon pole model is used in calculations of Σ. Here it is found that the value of the quasiparticle gap of TiO_2 calculated with the Godby-Needs approach is close to that calculated with the contour deformation method, a result that was also found for ZnO [126].

3.4.4 Obtaining quasiparticle energies

After inserting the noninteracting Green's function into the quasiparticle equation 3.26, within first-order pertubation theory the energy solutions $E_{m,k}$ satisfy

$$E_{m,k} = \varepsilon_{m,k} + \langle m,k| \left[\Sigma_X + \Sigma_C(E_{m,k}) - V'\right] |m,k\rangle.$$

Since $E_{m,k}$ appears on both sides of the equation, $\Sigma_C(E_{m,k})$ is expanded as

$$\begin{aligned}\langle m,k|\Sigma_C(E_{m,k})|m,k\rangle &\approx \langle m,k|\Sigma_C(\varepsilon_{m,k}) + (E_{m,k}-\varepsilon_{m,k})\frac{d\Sigma_C^R(\varepsilon_{m,k})}{dE}|m,k\rangle \\ &\approx \langle m,k|\Sigma_C(\varepsilon_{m,k})|m,k\rangle + \left(1-\frac{1}{Z(\varepsilon_{m,k})}\right)(E_mk-\varepsilon_{m,k})\end{aligned}$$

yielding

$$E_{m,k} = \varepsilon_{m,k} + Z(\varepsilon_{m,k})\langle m,k|\Sigma_X + \Sigma_C(\varepsilon_{m,k}) - V'|m,k\rangle \tag{3.57}$$

where the Z is the quasiparticle renormalisation factor:

$$Z_{(}\varepsilon_{m,k}) = \frac{1}{1-\frac{d}{dE}\Sigma^R_{mk,mk}(\varepsilon_{m,k})} \tag{3.58}$$

and Σ^R is the real part of the self-energy.

3.4.5 Technical limitations: empty states and plane-wave cutoffs

As a conclusion to this section on GW it is worth identifying the computational difficulties associated with these calculations. One significant hurdle is the summation over a technically infinite number of unoccupied states, which occurs both when constructing the polarisability (eq. 3.47) and the self-energy (eq. 3.56). Un-

fortunately the quasiparticle corrections are found to converge slowly with the number of states used in these summations; increasing the number of empty states adds to the expense of the initial DFT calculation used to construct the single particle orbitals and of course to the GW calculation itself, linearly increasing the number of required matrix elements. Recently a number of methods [121; 128–131] have been developed to circumvent this costly sum, but have yet to be widely implemented. Instead the number of conduction states must be considered an essential quantity to converge in "standard" sum-over-states GW calculations.

Other important quantities to converge are the plane-wave cutoff and k-point sampling of the initial DFT calculation, and also the size of the matrix G, G' of the polarisability. Generally, it is only feasible to include plane waves up to a maximum energy of 10–20 Ry for the latter, due to the vast number of matrix elements involved. On the other hand Σ_X, which has only one sum over G-vectors, can be calculated for higher plane-wave cutoffs ($\sim$ 100 Ry).

3.5 Photoemission

Having addressed how Σ can be calculated, it is now worth considering its importance in the context of spectroscopy. The photocurrent observed in a photoemission experiment may be derived from the Fermi Golden Rule expression introduced in Chapter 1. Since the expression contains matrix elements between states of the entire interacting system, evaluating it requires the full machinery of many-body physics.

There are two important concepts in photoemission which are generally applied in theoretical treatments. The first is that of a "blue electron" [132]; that is, the photoelectron created upon absorption of a photon is distinguishable from all

the other electrons in the solid, and interacts with the remaining $N-1$ electrons only in specific scattering events. Under this approximation the photoelectron is described with a single-particle state $\psi_k(x)$. The second is to distinguish between "intrinsic" and "extrinsic" phenomena. The intrinsic photocurrent considers the interactions surrounding the absorption of the photon and creation of a photoelectron, which leaves the remaining $N-1$ electrons in an excited state. Extrinsic processes concern the passage of the photoelectron from the interior of the solid to the detector, whereby it may lose energy through further interactions with the solid. Here the many-body treatment will focus on intrinsic processes, with any extrinsic losses treated phenomenologically.

3.5.1 The spectral function

In order to analyse the photocurrent it is useful to introduce the spectral function A:

$$A(x,x';E) = \sum_j f_j^{\pm}(x) f_j^{*\pm}(x') \delta(E - E_j^{\pm}) \tag{3.59}$$

A is related to the Green's function through

$$A(x,x';E) = \frac{1}{\pi} \left| \mathrm{Im} G(x,x';E) \right| \tag{3.60}$$

and obeys the sum rule

$$\int A(x,x';E) dE = \sum_j f_j^{\pm}(x) f_j^{*\pm}(x') = \delta(x-x') \tag{3.61}$$

Furthermore, in the case of non-interacting systems where $f_j(x) = \psi_j(x)$, A reduces to a generalised local density-of-states:

$$A_0(x, x'; E) = \sum_j \psi_j(x)\psi_j^*(x')\delta(E - \varepsilon_j)$$

3.5.2 The spectral function in the diagonal approximation

Again moving to a matrix element representation, taking the Green's function in the diagonal approximation of equation 3.31 yields the following for the spectral function:

$$\begin{aligned} A_{mm}(E) &= \frac{1}{\pi}\left|\mathrm{Im}G_{mm}(E)\right| \\ &\approx \frac{1}{\pi}\left|\mathrm{Im}\frac{1}{E - (\varepsilon_m + \Sigma_{mm}(E) - V'_{mm})}\right| \\ &\approx \frac{1}{\pi}\frac{|\Sigma^I_{mm}(E)|}{\left[E - (\varepsilon_m + \Sigma^R_{mm}(E) - V'_{mm})\right]^2 + \left[\Sigma^I_{mm}(E)\right]^2} \end{aligned} \tag{3.62}$$

where the self-energy has been split into real and imaginary parts $\Sigma_{mm} = \Sigma^R_{mm} + i\Sigma^I_{mm}$. If $\Sigma^I_{mm}(E)$ is small, this expression describes a function which peaks at $E = E_m = \varepsilon_m + \Sigma^R_{mm}(E_m) - V'_{mm}$. Expanding the first term in the denominator around E_m gives

$$E - (\varepsilon_m + \Sigma_{mm}(E) - V'_{mm}) \approx \left(1 - \frac{d\Sigma^R_{mm}(E_m)}{dE}\right)(E - E_m) = Z^{-1}(E_m)(E - E_m),$$

where the quasiparticle renormalisation factor $Z(E_m)$ was introduced previously in equation 3.58. Finally taking the limit $(Z\Sigma^I) \to 0$ recovers a δ-function expression for the spectral function:

$$A_{mm}(E) \approx Z_m(E_m)\delta(E - E_m) \tag{3.63}$$

The crucial difference with the non-interacting case is that the peak is weighted by the quasiparticle renormalisation factor Z: Clearly, integrating the expression 3.63 yields Z, while the full spectral function should satisfy the sum rule $\int A_{mm}(E)dE = 1$. In this sense Z measures how much a particular excitation of the many-body system corresponds to a familiar single-particle picture. In fact the full spectral function can be separated into a "quasiparticle" contribution and a background:

$$A_{mm}(E) = Z_m(E_m)\delta(E - E_m) + \text{background}$$

If Z is close to one, then the spectral weight is concentrated in the δ-function at E_m; one can therefore talk meaningfully about a quasiparticle excitation at this energy.

3.5.3 Expression for photoemission

The reason for introducing the spectral function stems from the analysis of Ref. 133, where it is shown that the contribution to the intrinsic photocurrent from a particular "blue electron" in state ϕ_k can be expressed as

$$I^i(k, E) = \int \phi_k^*(x)\Delta(x)A(x, x'; \xi_k - E)\Delta(x')\phi_k(x')dxdx' \tag{3.64}$$

E is the energy of the incoming photon, and Δ is the electric dipole operator governing the electromagnetic transition. ξ_k is the energy of the photoelectron. Expressing A in terms of matrix elements and again assuming the diagonal ap-

proximation, the photocurrent reduces to

$$I^i(k,E) \approx \sum_m \left|\langle\phi_k|\Delta|\psi_m\rangle\right|^2 A_{mm}(\xi_k - E) \tag{3.65}$$

Finally employing the analysis of the previous section to re-express A_{mm} gives

$$I^i(k,E) \approx \sum_m \left|\langle\phi_k|\Delta|\psi_m\rangle\right|^2 Z_m(E_m)\delta(E - E_m - \xi_k) \tag{3.66}$$

Therefore, according to equation 3.66 the intrinsic photocurrent is determined by the "quasiparticle density-of-states" $\sum_m Z_m(E_m)\delta(E - E_m)$ and matrix elements between the photoelectron and the orbitals used to represent the Green's function.

3.5.4 Extrinsic losses

Despite the complexity of the underlying physics of equation 3.66, it is worth remembering that it only deals with one part of the photoemission process, namely the creation of the photoelectron. Any subsequent extrinsic events, such as scattering of the photoelectron within the solid or at the boundary with the vacuum [46], are not included. Such events can lead to new features in the spectrum; for instance, photoelectrons which lose energy by creating charge-density waves (plasmons) contribute to new, satellite peaks. Calculating the energies of these features is beyond the scope of this thesis [113; 134; 135], where the focus will be on resolving the main peaks. The effect of extrinsic processes on the primary features is to reduce the intensity, and may be accounted for with a phenomenological model. The particular details of the model will be discussed in later chapters, but for now it is sufficient to note that the matrix elements in equation 3.66 and any inelastic losses can be grouped into a general intensity

prefactor $I_0(E)$, giving the expression for the observed photocurrent

$$I(\xi_k, E) = \sum_m I_0(\xi_k) A_{mm}(\xi_k - E). \tag{3.67}$$

3.6 Conclusions

The aim of this chapter was to provide an introductory description of the quantities and concepts which lie at the centre of the Green's function approach to understanding excitations in condensed matter. In particular, the time-ordered electronic Green's function calculated for the N-electron ground state was shown to contain the excitation energies of the $N \pm 1$-electron system. The amplitudes of this Green's function were shown to obey the so-called quasiparticle equation, which resembles a Kohn-Sham equation with the exchange-correlation potential replaced with a complex, non-local and energy-dependent operator Σ, the self-energy.

The second part of the chapter was devoted to the practicalities of determining Σ in the most widely-used method, the G_0W_0 approximation. The computational challenges of the approach are found in having to evaluate a large number of matrix elements in expressions of the self-energy and performing large summations. Replacing the dielectric function with a model based on single plasmon poles reduces some of the cost of having to evaluate expensive energy convolutions. Then, the concept of quasiparticles was further illustrated by considering the spectral function, which directly relates to the photocurrent observed in photoemission spectroscopy. In the case of a strong quasiparticle excitation one would expect to see a sharp peak in the experimental spectrum, at an energy determined by the non-interacting part of the Hamiltonian and the self-energy.

The theoretical physics behind *GW* is certainly sophisticated, and its success in calculating excited-state properties like band gaps is well documented [113]. However, the role played by DFT in these calculations should not be forgotten. Recalling equations 3.31 and 3.57, calculating quasiparticle energies in the standard *GW* approach assumes that the exchange-correlation potential provides a highly simplified, but nonetheless reasonable approximation to the full self-energy. Similarly one could argue that invoking a plasmon pole approximation is a remarkable step, compressing all the many-body physics of the dielectric function into two matrices of parameters. Much like for the local density-approximation in standard DFT, physically appealing arguments can be made for both of these steps, but the fundamental justification for their use is that they have been shown to work for many systems. As computer power increases and allows the study of more exotic materials, it is highly likely that *GW* methodology will also have to be developed in order to take more complex physical phenomena into account.

Chapter 4

The structure of TiO_2, the N3 dye and the N3/TiO_2 interface

In this chapter I consider the atomistic structure of the interface formed between the sensitizing molecule and semiconductor substrate found in dye-sensitized solar cells. The first half of the chapter is devoted to constructing interface models where the dye molecule is adsorbed on the TiO_2 surface in different geometries, and calculating their relative stability. This requires considering TiO_2 both in its bulk form and with surfaces exposed, as well as the dye molecule in isolation. The second half of the chapter looks to connect theory to experiment by calculating photoemission spectra for each model and comparing to previously published data.

This chapter is an expansion of the results previously published in Ref. 136.

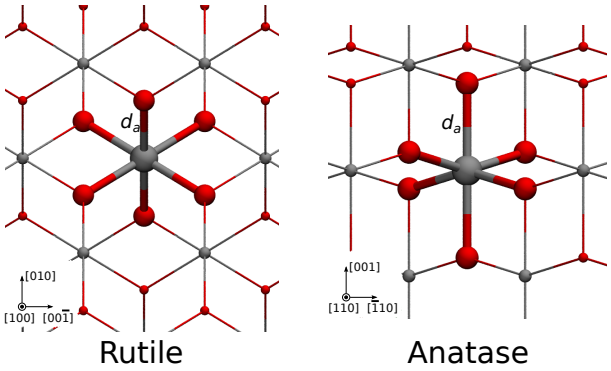

Figure 4.1: The crystal structures of the two most common polymorphs of TiO_2, rutile and anatase. Both are formed from TiO_6 octahedra as shown. The apical Ti–O bond, length d_a, is labelled. Colour code: Ti, silver; O, red.

4.1 Titanium dioxide

4.1.1 Crystal structure

Titanium dioxide occurs naturally in three crystal structures — rutile, anatase and brookite — and can assume a number of other forms at high pressure [137]. However the two polymorphs by far most relevant to technological applications are anatase and rutile [138]. As shown in Figure 4.1 both polymorphs are formed from stacked TiO_6 octahedra. The anatase crystal structure belongs to the space group $I4_1/amd$ [139] and rutile to the group $P4_2/mnm$ [140]. In each case the conventional unit cell is tetragonal, and the entire structure is determined by the lattice parameters a and c and a dimensionless internal co-ordinate u. The apical Ti–O bond length d_a (shown in the figure) is related to u via $d_a = uc$ for anatase and $d_a = ua\sqrt{2}$ for rutile. The primitive unit cells of the two polymorphs both contain two TiO_2 units, whose co-ordinates are listed in Table 4.1.

	Anatase			Rutile		
Ti	$-\frac{1}{8}$	$-\frac{3}{8}$	$\frac{1}{4}$	0	0	0
Ti	$\frac{1}{8}$	$\frac{3}{8}$	$-\frac{1}{4}$	$\frac{1}{2}$	$\frac{1}{2}$	$\frac{1}{2}$
O	$\frac{1}{8}$ - u	$\frac{3}{8}$ - u	$2u$ - $\frac{1}{4}$	u	u	0
O	$-\frac{1}{8}$ - u	$-\frac{3}{8}$ - u	$2u + \frac{1}{4}$	$-u$	$-u$	0
O	$-\frac{1}{8} + u$	$-\frac{3}{8} + u$	$-2u + \frac{1}{4}$	$\frac{1}{2} + u$	$\frac{1}{2}$ - u	$\frac{1}{2}$
O	$\frac{1}{8} + u$	$\frac{3}{8} + u$	$-2u - \frac{1}{4}$	$\frac{1}{2}$ - u	$\frac{1}{2} + u$	$\frac{1}{2}$

Table 4.1: Atomic positions of the primitive unit cell of the anatase and rutile polymorphs of TiO_2, given in terms of the primitive lattice vectors $[a\,0\,0]$, $[0\,a\,0]$ and $[\frac{a}{2}\,\frac{a}{2}\,\frac{c}{2}]$ (anatase) and $[a\,0\,0]$, $[0\,a\,0]$ and $[0\,0\,c]$ (rutile).

4.1.2 Calculation of structural parameters

The first step towards constructing an atomistic model of the N3/TiO_2 interface is to obtain the relaxed structure of bulk titania; that is, determine the values of a, c and u at which the total energy per unit cell is minimised. The calculations were performed within density-functional theory, treating exchange and correlation either in the local-density approximation (LDA, Perdew-Zunger parameterisation [53]) or with the Perdew-Burke-Ernzerhof (PBE) functional [54], which includes gradient corrections. The core-valence interaction was described by ultrasoft pseudopotentials [65], with the semicore Ti $3s$ and $3p$ electrons explicitly included in the valence. The Kohn-Sham wavefunctions and density were expanded in plane waves up to cutoffs of 35 and 200 Ry respectively, and the wavefunctions sampled on a $3 \times 3 \times 3$ Monkhorst-Pack grid for anatase and a $4 \times 4 \times 4$ grid for rutile. The structures were taken to be relaxed when the total force on each atom was below 0.03 eV/Å and the pressure on the unit cell less than 0.5 kbar. All calculations were performed using the `Quantum ESPRESSO` software package [141].

	anatase					rutile				
	this work		Ref. 142		Exp. [139]	this work		Ref. 142		Exp. [140]
	LDA	PBE	LDA	PBE		LDA	PBE	LDA	PBE	
a	3.73	3.79	3.74	3.79	3.78	4.52	4.61	4.55	4.63	4.59
c	9.36	9.72	9.53	9.74	9.52	2.91	2.96	2.93	2.96	2.96
u	0.209	0.207	0.207	0.206	0.208	0.304	0.305	0.304	0.305	0.305

Table 4.2: Structural parameters of bulk TiO_2 calculated here compared to previous calculations and experiment. The lattice parameters a and c are in Å, u is dimensionless.

Table 4.2 shows the structural parameters of anatase and rutile obtained in the LDA or with the PBE functional, compared to those calculated using the same methodology in a previous study [142] and those measured in X-ray diffraction experiments [139; 140]. The structural parameters calculated here are in close agreement with those reported in Ref. 142, which in turn lie within a few percent of the experimentally-measured values. The data display the standard trend of the local-density and generalised-gradient approximations underestimating and overestimating bond lengths, respectively [143]. Since in this case PBE performs slightly better than LDA, and also noting that gradient corrections may provide a more accurate description of interfaces, in the following the PBE functional is used to describe exchange-correlation unless otherwise stated.

4.1.3 Modelling mesoporous films

The next step in building an interface model is to move from bulk TiO_2 to a structure which reflects the nanostructured titania films found in actual dye-sensitized solar cell interfaces. A widely-used approach [144–152] is to cut bulk anatase TiO_2 so that the (1 0 1) plane is exposed. Additional cuts can be performed to form a nanocluster, or periodicity can be enforced in the [0 1 0] and [$\bar{1}$ 0 1] directions to form a slab geometry. The latter approach is taken here, forming the

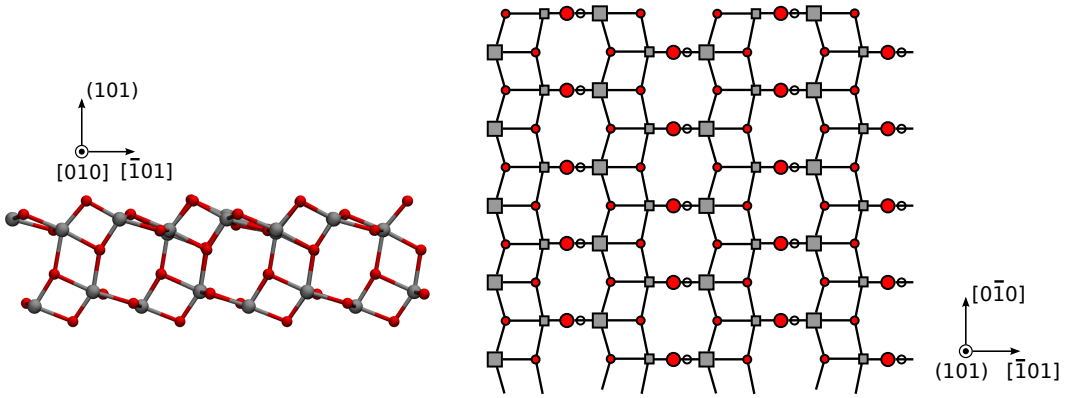

Figure 4.2: The anatase (1 0 1) slab used to model the mesoporous TiO_2 films, viewed along the [0 1 0] direction (left) and from above. In the schematic view, red circles and silver squares denote O and Ti atoms respectively. The largest symbols show the atoms at the surface, which are fivefold (Ti) or twofold (O) coordinated. The rows of Ti atoms act as chemisorption sites for the dye molecule.

stoichiometric slab shown in Figure 4.2. The use of this model is driven by the following observations:

- The mesoporous films employed in DSCs consist largely of TiO_2 in the anatase phase [153].

- High-resolution transmission electron microscopy images of the nanostructured films are dominated by fringes assigned to the anatase (1 0 1) crystal planes [153]. Indeed in natural anatase crystals there are two exposed surfaces, along the (1 0 1) and (0 0 1) crystal planes, and the (1 0 1) surface accounts for over 90% of the total area [138]. Calculations reported in Ref. 142 also found that (1 0 1) is the most thermodynamically stable surface of anatase.

- Since TiO_2 nanoparticles in mesoporous films are much larger than individual dye molecules (10–40 nm vs. 1 nm [153]) it is reasonable to neglect effects arising from the nanoparticles edges, and instead work in a slab geometry.

The electronic structure of TiO_2 in bulk and slab forms will be addressed in the next two chapters, but for now it is sufficient to note that in DFT the stoichiometric (1 0 1) slab is semiconducting with a band gap > 2 eV (the precise value depending on the geometry of the slab). Although creating the slab shown in Fig. 4.2 requires cutting Ti–O bonds, there are no dangling bonds at the surface. A simple explanation of this phenomenon is provided by the "autocompensation" picture [154]. Bulk TiO_2 has a mixed covalent/ionic bonding character, with formal charges of Ti^{4+} and O^{2-}. Cutting a Ti–O bond by removing an O atom leaves a dangling bond with excess charge; conversely, cutting an O–Ti bond by removing a Ti atom leaves a charge deficient bond. An equal number of Ti–O and O–Ti bonds are broken when forming the anatase (1 0 1) surface, so the excess charge from the Ti–O bonds exactly compensates the charge deficit from the O–Ti bonds and leaves a surface with only totally filled or totally empty bonds.

4.1.4 Details of the anatase (1 0 1) slab

The anatase slab shown in Fig. 4.2 has dimensions $20.9 \times 19.0 \times 5.8$ Å^3 and consists of 80 TiO_2 units (four TiO_2 layers). The area of the slab is large enough to accommodate the large footprint of the sensitizing molecule when constructing interface models, but the thickness of < 1 nm is far smaller than the > 10 nm radius of actual nanoparticles. Since DFT calculations on even the thinnest slab are already expensive computationally (960 Kohn-Sham states), it is impractical to consider thicker slabs of this surface area. Instead the 5.8 Å slab is used to construct interface models, but in all geometry relaxations the lowest three layers of atoms are fixed in their bulklike position in order to mimic the structure of the larger nanoparticle.

The precise atomistic structure of the clean anatase (1 0 1) surface will be

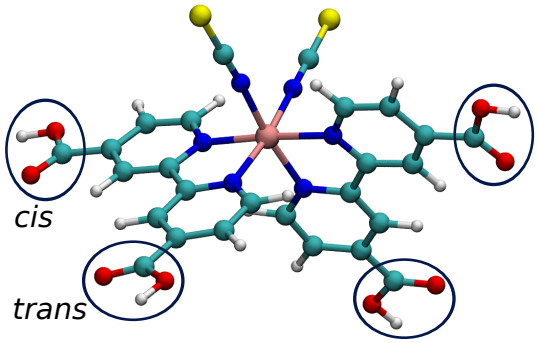

Figure 4.3: Ball-and-stick model of the N3 dye. The four carboxylic acid (COOH) groups, which may be cis or trans to the NCS ligands, are identified. Colour code: Ru, pink; S, yellow; O, red; N, blue; C, cyan; H, white.

discussed in detail in Chapter 7. However for now it is useful just to consider the schematic diagram of the rectangular surface cell, also shown in Fig. 4.2. There are rows of Ti and O atoms running along [0 1 0] direction; within each row the atoms are separated by the lattice constant $a = 3.79$ Å. The fivefold co-ordinated Ti atoms (large silver squares) are possible sites for chemisorption of oxygen atoms, while the twofold co-ordinated O atoms (large red circles) are chemisorption sites for hydrogen. These facts will be used in Section 4.3 when constructing interface models.

4.2 The N3 dye

4.2.1 Molecular structure

The other component of the interface is the dye molecule $Ru(dcbpyH_2)_2(NCS)_2$, commonly known as N3 [36]. The ball-and-stick model of N3 (approximate C_2 symmetry) is shown in Figure 4.3. The molecule consists of a central ruthenium atom co-ordinated to two bipyridines and two thiocyanate (NCS) ligands. Each

Parameter	PBE, this work	PBE, Ref. 45	Exp. [155]
d(Ru–NCS)	2.05–2.04	2.07–2.07	2.05–2.05
d(Ru–bpy_{trans})	2.07–2.07	2.08–2.08	2.04–2.06
d(Ru–bpy_{cis})	2.07–2.07	2.07–2.07	2.03–2.01
N–C(NCS)	1.19–1.19	1.18–1.18	1.16–1.10
C–S(NCS)	1.61–1.61	1.64–1.64	1.61–1.68
∠N(NCS)-Ru-N(NCS)'	90.7	90.7	88.7
∠N(bpy_{trans})-Ru-N(bpy_{cis})	78.7–78.6	78.9–78.9	79.1–79.8
∠N(bpy_{trans})-Ru-N(bpy_{trans})	95.5	92.2	90.5
∠N(bpy_{cis})-Ru-N(bpy_{cis})	174.5	175.3	176.2

Table 4.3: Optimised geometrical parameters (distances in Å, angles in °) for the N3 molecule compared to previous calculations and experiment.

bipyridine carries two carboxylic acid groups (COOH) which either lie cis or trans to the NCS ligand, as shown in the figure.

4.2.2 Calculation of structural parameters

N3 is not volatile, so its structural parameters have only been measured for its crystalline form [155]. The structure of the isolated molecule was obtained by optimising the geometry in DFT, using the experimental crystalline structure as a starting point. The same computational approach was used as for bulk TiO_2, except that the wavefunctions were sampled at the Γ-point only. To ensure no interactions between periodic replicas, the Martyna-Tuckerman Coulomb truncation scheme [69] and a 50×50×50 $Å^3$ simulation cell were used.

In Table 4.3 some of the calculated structural parameters are compared to the data measured experimentally for the N3 crystal and also to the DFT calculations reported in Ref. 45. The calculated, gas-phase parameters lie within a few percent of the measured, crystalline parameters, with the same systematic overestimation of bond lengths observed as for the PBE calculations on TiO_2. It is interesting to note that in the crystal, intermolecular interactions and interactions with solvate

DMSO molecules break the C_2 symmetry of the gas phase. For instance, the lengths of the C–S bond in the two NCS ligands exhibit a 0.1 Å variation. Interactions between the N3 molecule and TiO_2 substrate may similarly be expected to break the molecular symmetry.

4.3 Adsorption models of isolated N3 dyes on the anatase (101) surface

Having determined the structures of the TiO_2 substrate and N3 dye in isolation, it is now possible to construct atomistic models of the interface between the two. The problem that arises when considering the adsorption of large molecules is that, by including all rotations and distortions of the molecular structure, the number of possible adsorption modes is very large. A complete mapping of the total energy landscape spanned by the combined adsorbate/substrate system is therefore impractical. Instead, it is necessary to use some physical intuition and geometrical guesswork to attempt to find stable structures. A similar approach was employed in Ref. 155. As an example, the distance between the two trans COOH groups of N3 (10.5 Å) nicely matches double the spacing between the rows of Ti atoms (10.4 Å), so it is likely that there exist stable configurations where the trans groups are bound to these rows.

Unfortunately even within this approach there is no clear candidate atomistic model of the N3/TiO_2 interface. Indeed no less than four different adsorption geometries have been proposed in the literature in the last ten years [145; 149; 156; 157]. The strategy employed here is to first perform a critical survey of these models with regard to their relative stabilities, and then attempt to make a direct connection to experimental measurements by calculating core-level photoemission

spectra. Ideally this comparison would be used to select or exclude particular adsorption geometries.

4.3.1 Computational details

Atomistic models of the N3/TiO_2 interface were constructed by taking the anatase (1 0 1) slab described in Section 4.1.4 and placing an N3 molecule in the desired geometry onto the slab. Then, a damped Car-Parrinello MD simulation was performed so that the atoms relaxed to their equilibrium positions. All atoms were allowed to move except the lowest three layers of the slab (Section 4.1.4), and the criterion for a relaxation was that the force on each atom (except in the fixed layers) was below 0.07 eV/Å. The dimension of the simulation cell in the direction normal to the slab was chosen so that there was at least 10 Å of vacuum between the top of the adsorbed molecule and the bottom of the next periodic replica of the interface. When calculating adsorption energies any spurious electrostatic dipole interaction was removed by including the self-consistent correction of Ref. 71.

4.3.2 The adsorption energy

In order to compare relative stabilities of different interface geometries it is useful to define an adsorption energy E_{ads}:

$$E_{\text{ads}} = E_C - (E_S + E_M) \tag{4.1}$$

Here, E_C is the total energy of the adsorbed molecule and substrate. E_S is the total energy of the clean substrate, and E_M the total energy of the isolated molecule. If periodic boundary conditions are in use all calculations must be performed with the same simulation cell. As defined above, a more negative value

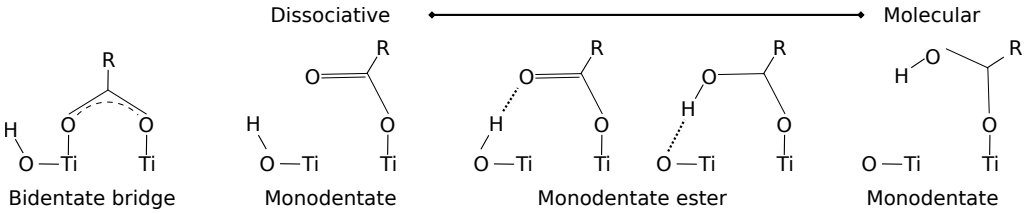

Figure 4.4: Some possible adsorption modes of RCOOH molecules on metal oxide surfaces. In dissociative modes the H atom is transferred to the substrate, while in molecular modes it remains part of the COOH group. Ester-type modes involve both hydrogen and chemical bonds.

of E_{ads} implies greater stability; in some definitions of the adsorption energy the signs are reversed.

4.3.3 Carboxylates on metal surfaces

Although some studies have considered the possibility that the NCS ligands play a role in binding the N3 molecule to TiO_2 [49], the more widely-held view [145; 149; 156–158] is that it is the dye's carboxylic acid (COOH) groups which are responsible for anchoring the dye. In this case the problem of determining atomistic models of the N3/TiO_2 interface falls into a more general framework which describes the binding of carboxylates to metal oxides. Figure 4.4 provides a guide to the necessary terminology, summarised as follows:

- Carboxylate adsorption can be *dissociative*, where the hydrogen atom in the COOH group is transferred to the substrate, or *molecular*, when the hydrogen atom remains part of the COOH group.
- Between the extremes of pure dissociated or molecular binding there are *ester-type* modes where hydrogen bonds are also formed.
- In the *bidentate bridge* mode the COOH group dissociates, forming a surface hydroxyl (OH) group and two strong bonds to the metal atoms.

- In *monodentate* binding only one bond is formed to a metal atom.

The simplest molecule with a carboxylic acid group is formic acid (R=H; HCOOH). The relative stability of various binding modes of this molecule to the anatase (1 0 1) surface was investigated in Ref. 147. The most stable adsorption geometry was found to be monodentate ester-type with E_{ads}=−0.92 eV. The next most stable mode was the bidentate bridge (E_{ads}=−0.68 eV) while dissociative monodentate binding was considerably less stable (E_{ads} =-0.21 eV). It is reasonable to expect the trends observed for formic acid to carry across to the four COOH groups of the N3 molecule.

4.3.4 Interface models—description of structure

The ball-and-stick models of six candidate interface models, with the atoms in their relaxed positions, are shown in Figure 4.5. The models are labelled by the number of COOH groups which participate in binding the N3 molecule to the substrate. "I" stands for "isolated", in that each molecule is well-separated from its neighbours. Four of the six configurations (I2a–c, I3a) are based on models from previous studies, one is a new model (I3b), and the other (I1) is a benchmark system.

Each configuration can be described using the terminology of carboxylate adsorption introduced in Fig. 4.4:

- *I1*: a single trans COOH group is adsorbed in a bidentate bridge mode. This model is one of the simplest adsorption modes, and has the advantage that it can be readily compared to previous calculations on formic acid [147].

- *I2a*: two COOH groups belonging to the same bipyridine are both adsorbed in bidentate bridge modes. This model was introduced to explain the X-ray

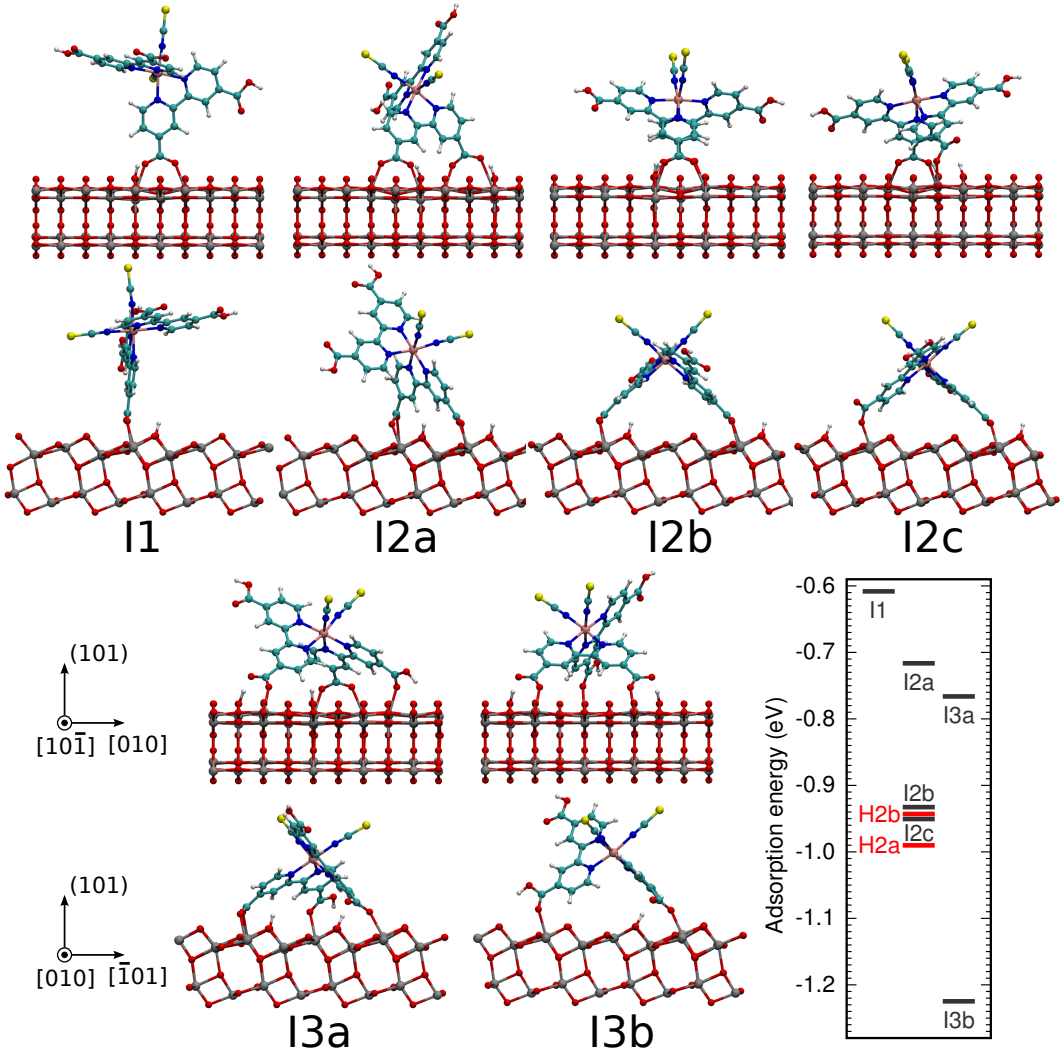

Figure 4.5: Ball-and-stick models of the six considered interface models of the N3 dye and anatase (1 0 1) slab, viewed along different directions. Also shown are the adsorption energies calculated for these models and for two H-bonded models, discussed later in the text.

photoemission specta measured for N3-sensitized anatase [156] and studied in subsequent quantum chemical calculations [144]. The same model has been employed to describe the adsorption of a single bi-isonicotinic acid ligand [159], a system which will be returned to in Chapter 7. It should be noted that in this model, one of the Ti–O bonds is heavily elongated compared to the rest: 2.68 Å vs. 2.06, 2.18 and 2.01 Å.

- *I2b*: two trans COOH groups (belonging to different bipyridines) are both adsorbed in bidentate bridge modes. This model was first proposed based on the molecular modelling of Ref. 155 and subsequently used to interpret infrared spectroscopy experiments on the interface [157].

- *I2c*: like I2b, two trans COOH groups are adsorbed. The difference is that one of the groups forms a monodentate ester-type bond instead of a bidentate bridge. This model was found to be the most stable in the molecular dynamics investigation of N3 dyes on anatase (1 0 1) slabs reported in Ref. 145.

- *I3a*: three COOH groups bind the dye to the substrate. One trans group is adsorbed in a bidentate bridge. The cis group on the same ligand is adsorbed in a molecular monodentate mode, and the trans group on the other ligand forms an ester-type bond. This model was found to be stable in a molecular dynamics investigation of an N3 dye on an anatase nanocluster [149].

- *I3b*: again three COOH groups bind the dye to the substrate. A cis and trans group on the same bipyridine form ester-type bonds, and the other trans group adsorbs in a molecular monodentate mode. This model has not been previously proposed by others.

4.3.5 Interface models—adsorption energies

Fig. 4.5 also shows the adsorption energies calculated for each interface model. As expected the adsorption energy of I1 is comparable to that calculated for the bidentate bridge mode of formic acid in Ref. 147 (−0.61 eV vs. −0.68 eV). Then the overall trend is a 0.3 eV increase in stability per COOH group involved in binding. There can be a substantial energy cost associated with distorting the molecule in order to bring the COOH group into contact with the substrate: for instance the bipyridine twist and elongated Ti–O bond in I2a results in an adsorption energy of −0.72 eV compared to −0.95 eV for I2c. For I3a the effect is even more severe, to the extent that the stability gain of involving the third group is cancelled by the cost of distorting the molecule, with E_{ads}=−0.77 eV. Interface model I3b, which involves minimal strain on the molecule and two favourable ester-type bonds, is the most stable of the sample considered here with an adsorption energy of −1.22 eV.

On one hand the enhanced stability of I3b (0.27 eV, more than $10\times k_BT$ at room temperature) makes it a tempting assignment for the adsorption geometry of the N3 molecule in actual DSC interfaces. However the following points of caution should be noted:

1. As pointed out above the phase space spanned by all possible adsorption modes is huge. It is entirely possible that there are other structures, not considered here, that have a lower energy.

2. All structures were formed by manually positioning the dye molecule and if necessary removing the hydrogen atom from the COOH group. Thus any energy barriers that may be associated with forming a particular interface model are not taken into account; energetically favourable geometries

may not be kinetically accessible in the sensitization process. For instance configurations I3b and I2c rely on the presence of suitably placed surface hydroxyls, but there may be substantial barriers to OH diffusion. Indeed the calculations of Ref. 160 indicate that surface protons might tend to diffuse into the bulk solid.

3. These isolated models do not take into account any interactions between dye molecules on the surface or with external molecules.

For these reasons it is desirable to go beyond the adsorption energy as a criterion of selecting a realistic interface model, and instead look to form a connection between calculations and experimental efforts to characterise the interface.

4.4 O $1s$ core-level shifts at the N3/TiO_2 interface

4.4.1 Experimental data—general overview

Since the introduction of the N3/TiO_2 system in 1993 [36] there have been several attempts to determine the atomistic structure of the interface experimentally. The experiments can broadly be sorted into three categories: infrared (IR) spectroscopy, X-ray photoemission spectroscopy (XPS) and scanning tunnelling microscopy (STM). Despite considerable progress, the STM work is still in its infancy [161; 162] and the image resolution is currently too low to distinguish particular geometries. IR [157; 158; 163–165] experiments offer a promising means of identifying carboxylate binding modes, because different chemical bonds have different vibrational signatures. But although it is possible to calculate these

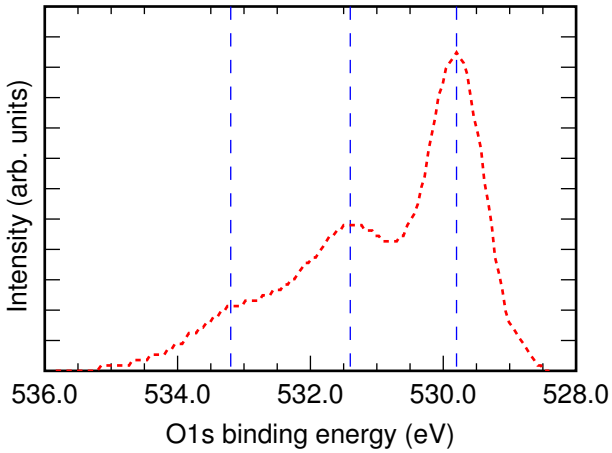

Figure 4.6: The O 1s spectrum reported in Ref. 47. N3-sensitized anatase films were illuminated by a beam of 758 eV photons generated by the synchrotron source at the Swedish National Laboratory in Lund. The kinetic energy of photoelectrons was measured, allowing the binding energy to be deduced. The spectrum can be deconvolved into three gaussians, whose centres are shown as vertical dashed lines.

signatures from first principles [145; 166], the interpretation of IR data more often relies on empirical rules derived for other systems. Also if vibrational bands overlap in the spectrum, the signals from particular bonds can be obscured, particularly if the experimental resolution is low. These factors led to conflicting assignments of the spectrum, with earliest experiments proposing monodentate linkages [163; 164], later ones proposing bidentate bridges [157; 165] and most recently, observation of signals associated with H-bonding [158].

Like IR spectroscopy, XPS gives information about the nature of bonding at interfaces through the observation of spectral fingerprints of different chemical bonds. Bombarding the N3/TiO_2 interface with high-energy photons and measuring the kinetic energy of emitted photoelectrons gives the core electron binding energies, that is, the energy required to remove the most tightly-bound electrons from each atom (Chapter 1). The binding energies of the O 1s electrons at the N3/TiO_2 interface have been measured in several studies [47; 49; 156; 167; 168].

The highest-resolution experimental data was reported in Ref. 47 and is reproduced in Figure 4.6.

4.4.2 Previous assignment of the O 1s spectrum

The experimental O 1s spectrum in Fig. 4.6 shows three components centred at 529.8, 531.4 and 533.2 eV, marked as dashed lines. In Ref. 47 the following assignments are made:

- The strong peak at lowest binding energy (529.8 eV) originates from the 1s electrons emitted from O atoms in the TiO_2 substrate.
- The two peaks at 531.4 and 533.2 eV originate solely from the eight oxygen atoms of N3 and are thus called adsorbate peaks.
- The adsorbate peak at 531.4 eV has dual origin. Part of the signal comes from double-bonded (carbonyl) O atoms in N3's carboxylic acid (COOH) groups located far from the substrate. Additionally, carboxylate O atoms bound to Ti atoms in a bidentate bridge configuration also contribute here.
- The adsorbate peak at 533.2 eV comes from the single-bonded (hydroxyl) O atoms in N3's carboxylic acid (COOH) groups located far from the substrate.

The authors of Ref. 47 argued that their data were consistent with an adsorption model where two of the four carboxylic groups of N3 were involved in binding the molecule to the substrate, in bidentate bridging modes (models I2a or I2b in Fig. 4.5), based on the following reasoning. Fitting three gaussian curves to the experimental spectrum gives a relative intensity of 0.31 between the adsorbate peaks. In models I2a and I2b, there are four O atoms forming bidentate bridges

and two double-bonded O atoms in the COOH groups located far from the substrate, i.e. six contributions to the 531.4 eV peak. The remaining two O atoms are single-bonded, so contribute to the 533.2 eV peak. Under the assumption that the intensity of each peak scales linearly with the number of O atoms which contribute to it, the expected ratio is therefore 2:6 = 0.33, in agreement with the experimentally-observed 0.31.

4.4.3 Calculation of O 1s spectra—general principles

The assignment described above is certainly a plausible explanation of the data. If correct, it narrows down the number of candidate interface models to just two, I2a and I2b. However the implicit assumption is that the O 1s signatures of other types of carboxylate binding (e.g. the monodentate linkages of I3b) are appreciably different from the signatures of bidentate bridges. If this is not the case, it is possible that any of the interface models in Fig. 4.5 could provide equally plausible assignments of the O 1s spectra. Calculating and comparing the O 1s spectra for the six interface models allows this assumption to be tested.

The O 1s spectra were calculated using the ΔSCF method introduced in Chapter 2. For a given interface model a DFT calculation was performed where the pseudopotential of a single oxygen atom was replaced with one containing a 1s core hole. The calculated total energy gives (up to a constant) the O 1s binding energy of that particular atom, and repeating the process for all oxygen atoms builds up the full dataset for that interface model. To account for vibrational broadening and core-hole lifetimes, gaussians of width 1.6 eV were convolved onto each shift to produce a synthetic spectrum. This width was chosen to best match to the experimental spectrum of Ref. 47. The same computational parameters (functional, cutoffs, simulation cell size) were used as for the geometry

relaxations. Since the pseudopotential containing a core hole has a net charge of +1, in periodic boundary conditions the electrostatic energy diverges. This divergence is avoided by introducing a compensating negative jellium background, but even so there is still a $\frac{1}{R}$ interaction between periodic images. The possible effects of this interaction is discussed below.

The current analysis focuses solely on the two adsorbate peaks at higher binding energy. The third peak (at 529.8 eV) contains contributions from all oxygen atoms in the TiO_2 substrate which lie close enough to the surface so that their photoelectrons are not inelastically scattered before escaping the solid. The characteristic length scale for this scattering is the phenomenological electron escape depth λ, which is energy and material dependent; for photoelectrons with 200 eV kinetic energy reasonable values range from 3–20 Å [169] (the value of 200 eV for kinetic energy is appropriate for incident photons of energy 758 eV extracting electrons with binding energies of 530 eV). However the anatase slab used to construct the interface models is only 5.8 Å thick, and three of its eight oxygen layers sit at the unphysical lower surface of the slab. Therefore the substrate peak at 529.8 eV cannot be accessed unless some correction is made for the finite width of the slab; such a scheme is developed Chapter 7.

As pointed out in Chapter 2 the calculated $1s$ binding energies carry an unknown constant, but it is meaningful to compare differences in binding energies. In order to easily compare configurations to each other and to experiment, the following procedure was adopted. First, analogous to the experimental analysis two gaussians were fitted to the calculated spectra. Then the arbitrary constant was set so that the high-binding-energy peak was positioned at the origin. Correspondingly a shift of 533.2 eV was applied to the experimental data to the same effect. Then the key quantity to compare is the separation of the two adsorbate

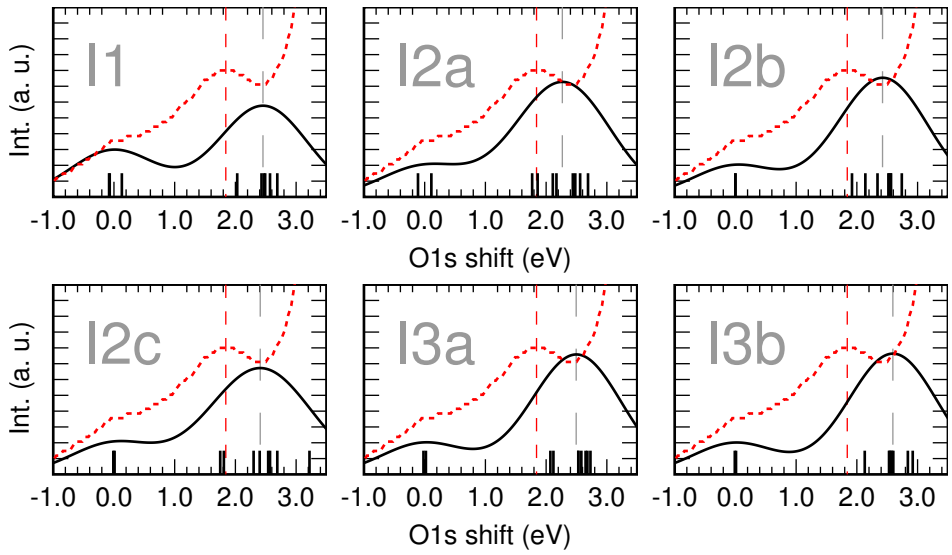

Figure 4.7: O 1s spectra calculated for the six adsorption models in Fig. 4.5 (black curves). Higher binding energy corresponds to the left side of the plots. The experimental spectrum from Ref. 47 is shown as the red dashed line. The dashed vertical lines give the peak separation between the two gaussian components of the spectra. The short vertical lines give the raw O 1s binding energies used to construct the spectrum.

Model	I1	I2a	I2b	I2c	I3a	I3b	Ref. 47
Separation (eV)	2.45	2.25	2.41	2.41	2.48	2.59	1.8
Intensity	0.50	0.25	0.25	0.25	0.25	0.25	0.31

Table 4.4: Separation and relative intensity of the two adsorbate peaks calculated for each interface model, compared to experiment.

peaks, measured to be 1.8 eV in Ref. 47 and 1.8 eV [168] and 1.6 eV [167] in other studies.

4.4.4 O 1s spectra of interface models

The O 1s spectra calculated for the six interface models are shown in Figure 4.7. The bare calculated shifts (i.e. without the convolved gaussians) are also shown in the figure. The experimental spectrum from Ref. 47 is shown in red. The dashed vertical lines give the splitting between the adsorbate peaks, and the values of the

splitting and relative intensities of the two peaks are also provided in Table 4.4.

The most important message of Fig. 4.7 is that the peak separations calculated for all six interface models fall within the range 2.3–2.6 eV, systematically overestimating the experimentally-observed value by at least 0.5 eV. This is a significant discrepancy, seeing that the benchmark calculations on small molecules presented in Chapter 2 had an r.m.s. deviation of 0.2 eV from experiment when comparing differences in 1s binding energies. The following other points should be noted:

- *The peak at high binding energy* (around 0.0 eV in Fig. 4.7) is formed from the single-bonded (hydroxyl) O atoms in N3's COOH groups, in agreement with the experimental assignment. The hydroxyl atom contributes to this peak both when the COOH group is located far from the substrate, or if the group is bonded in a molecular monodentate mode (as for I3a and I3b).

- *Double-bonded (carboxyl) O atoms in the COOH groups* have 2.4–2.6 eV lower binding energy than the hydroxyls. Careful examination of Fig. 4.7 shows that the spectra of all interface models contain contributions at this energy, from the COOH groups located far from the substrate.

- *O atoms bonded in bidentate bridging modes* have similar 1s binding energies to free carboxyl atoms, again agreeing with the experimental assignments. For I2a the four O atoms bonded to Ti appear at 2.1, 2.2, 2.5 and 2.6 eV in Fig. 4.7.

- *O atoms in ester-type bonds* have the lowest 1s binding energies of the carboxylate modes considered here. Model I3b, which has two COOH groups bound in strong ester-type modes, has contributions to the spectrum at 2.8–3.0 eV. All three O atoms involved in bonding— i.e. Ti–O–C, C–O–H

and H–O–Ti — have shifts within 0.3 eV of each other. If the H-bond is weaker as in I2c, the three atoms are more strongly inequivalent.

- *Surface OH groups* which do not interact with the dye (e.g. in I2a) contribute to the adsorbate peak, appearing at 1.8 eV in Fig. 4.7. Consequently these contributions should be included when making arguments based on relative intensities as in the experimental assignment.

- *Unadsorbed COOH groups* have slightly different 1s energies depending on whether they are cis or trans to the NCS ligands. This effect is observed in model I2a where there is one cis and one trans COOH group located far from the substrate. The two contributions to the high-binding-energy peak are split by 0.2 eV, with the cis contributions appearing at higher energy. With the 1.6 eV broadening this splitting is not resolved. In model I2b the unadsorbed COOH groups are both cis, so no splitting is seen.

- *Large differences in bond lengths* have a surprisingly small effect on the 1s binding energies. The clearest example is I2a: it was pointed out above that in one of bidentate bridges there is a 0.7 Å difference in the length of the Ti–O bonds, but the corresponding difference in 1s binding energies is less than 0.1 eV.

The above points explain the trends displayed in Table 4.4. Including the contribution from the surface OH groups gives relative intensities of 2:8 for I2a and I2b, compared to 2:6 as found in the assignment of Ref. 47. The strong ester-type bonds interface model I3b provide a large contribution at lower binding energy, so this model has the largest peak separation; the cis/trans splitting of I2a widens the higher-energy peak, giving it the smallest separation.

4.4.5 Conclusions from calculations on single-molecule interface models

The calculations on the six interface models have demonstrated three points. First, large changes in structural parameters of the interface lead to only subtle changes in the O 1*s* spectrum. The calculated spectra of I2b and I2c are very similar, despite one having two bidentate bridges and the other a monodentate/bidentate mix. Second, although model I3b was calculated to be the most stable, it also overestimates the peak separation by the largest amount compared to experiment. But the third point is that *all* of the spectra significantly overestimate the peak separation.

A variety of reasons could account for this discrepancy:

- The problem of determining the atomistic structure of the N3/TiO_2 interface may not be particularly well-defined; that is, there could be many different adsorption models co-existing on the surface. This in fact is a highly likely scenario, and may partly account for the large broadening of the experimental spectrum. Yet since all of the six overestimate the peak separation, any combination of these interface models will display the same overestimation.

- The sample of six interface models could simply be too small, thus not including the atomistic structure found in the real interface. This possibility cannot be discounted, but as already pointed out the 1*s* spectrum does not appear to be very sensitive to individual geometrical parameters; therefore, in order to induce the 0.5 eV change in peak separation necessary to obtain agreement with experiment, presumably a radically different interface model would be required.

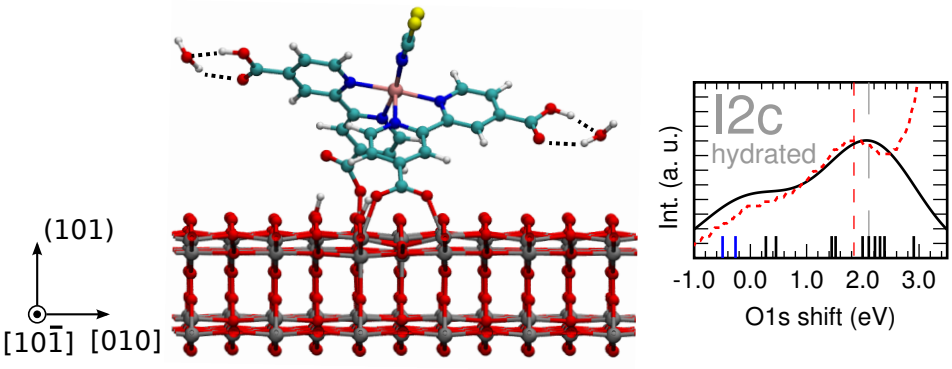

Figure 4.8: Ball-and-stick representation and O 1*s* spectrum of a model based on I2c, with two additional H_2O molecules included at the interface which form H-bonds with the unadsorbed COOH groups. The H-bonds formed with the hydroxyl and carbonyl O atoms are of length 1.80 Å and 2.05 Å respectively. The red dashed line is the experimental spectrum. The two short blue lines are the contributions to the spectrum from the O atoms of the H_2O molecules.

- The method of calculating core-level shifts, found to be accurate to within 0.2 eV for gas phase molecules, may have broken down in the condensed phase. This would be a surprising result; by nature first-principles theories make few assumptions about the system under study, which is why DFT is regularly applied to both solids and molecules.

- The six interface models are based on single N3 molecules, isolated on the surface, and therefore do not include the possibility that these molecules interact with each other, or with external molecules. It is this aspect which is investigated in the final section of this chapter.

4.5 Beyond single-molecule interface modules

4.5.1 External contaminants

The first possibility is that the *ex situ* preparation of the N3-sensitized TiO_2 films performed in Ref. 47 introduced contaminant molecules, which interact with the COOH groups and affect the O 1*s* binding energies. Indeed the C 1*s* spectra of the films show evidence that additional hydrocarbons are present in the sample [47], while the fact that the dye is applied in solution obviously introduces the possibility that H_2O molecules get trapped at the interface.

On the other hand, in order for there to be a noticeable change in the O 1*s* spectrum, a large fraction of the adsorbed N3 molecules must be affected by these interactions, perhaps forming supramolecular assemblies of dye and contaminant molecules. It is unlikely that bulky hydrocarbons could form such assemblies, but H_2O molecules are sufficiently small to form H-bonds with unadsorbed COOH groups of dyes within the monolayer.

A possible structure based on model I2c with two H_2O molecules added is shown in Figure 4.8. Each H_2O molecule forms two H-bonds with the unadsorbed COOH groups. The O 1*s* spectrum calculated for this interface model is also shown in Fig. 4.8. Crucially, the H-bonds formed between the H_2O molecules and the hydroxyl O atom of the COOH groups shifts the 1*s* binding energy of the latter to lower energy; conversely the binding energy of carbonyl O atom is shifted to higher energy. Thus the separation in 1*s* binding energy between the carbonyl and hydroxyl O atoms of the COOH group goes from 2.5 eV (in the absence of H-bonding) to 1.8 eV.

This phenomenon—that the difference in 1*s* binding energies between the two O atoms in COOH groups is reduced if the COOH group undergoes H-bonding—

was previously demonstrated in experiments [170] and calculations [171] on formic acid (HCOOH). In the DFT calculations of Ref. 171 it was shown that, on forming an H-bonded dimer of formic acid, the 1s binding energy of hydroxyl O atom shifted to 0.81 eV lower binding energy, while the carbonyl shifted to 0.15 eV higher energy. Again it should be emphasised that in the N3/TiO_2 O 1s spectra, the position of the adsorbate peak at high energy is determined by the hydroxyl O atom; and, according to the formic acid calculations, this is the atom most heavily affected by H-bonding. Therefore it is certainly plausible that H-bonding could account for the overestimation of the calculated separation of the two adsorbate peaks compared to experiment.

The problem with using H_2O molecules as the source of the H-bonding is that, since they themselves contain O atoms, the H_2O molecules provide their own contribution to the spectrum. These new contributions are shown in Fig. 4.8 as the blue lines at -0.2 eV and -0.5 eV. That is, the H_2O molecules also contribute to the high-energy adsorbate peak, and act to shift it to higher energy. The overall separation of the adsorbate peaks calculated for the hydrated model I2c is 2.10 eV, while the relative intensity is (2+2):(6+2) = 0.5. The separation is closer to the experimental value of 1.8 eV than the models based on isolated dyes, but the intensity ratio is overestimated compared to 0.31.

4.5.2 Intermolecular H-bonding

In the previous section it was shown that H-bonding of COOH groups provides a mechanism of reducing the separation of the two adsorbate peaks in the O 1s spectrum of the N3/TiO_2 interface. Using H_2O molecules as the source of the H-bonds created a new problem, since these molecules themselves contributed to the spectrum. A simpler solution is not to invoke external molecules, but instead

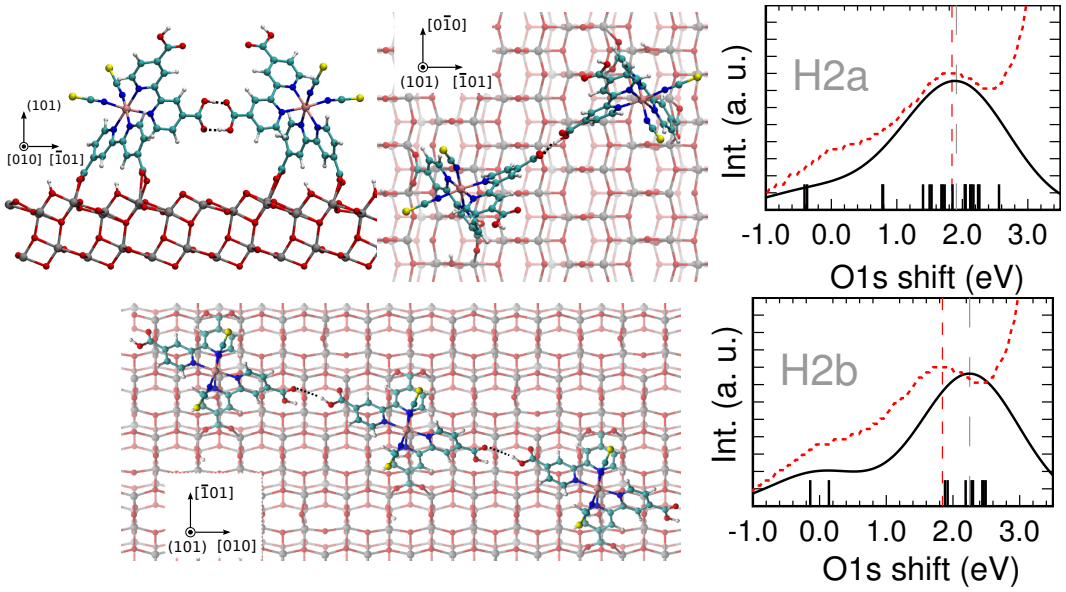

Figure 4.9: Ball-and-stick representations and O 1*s* spectra of interface models which include H-bonds. For clarity, the periodic repeats are not shown; the surface cells are rectangular for H2a (31.3×7.6 Å^2) and oblique for H2b (area 138 Å^2). The red dashed line is the experimental spectrum.

suppose that H-bonds are formed between N3 molecules within the monolayer.

Figure 4.9 shows ball-and-stick representations of two interface models based on H-bonded N3 dye molecules. The models probe the strong and weak regimes of H-bonding. In H2a two N3 molecules adsorbed via two bidentate bridges on the same bipyridine (c.f. model I2a) form an H-bonded dimer through their COOH groups trans to the NCS ligands. Two strong H-bonds are formed of length 1.51 Å. In H2b long chains of N3 molecules are formed, linked by H-bonds of length 2.68 Å. Each molecule is bound to the TiO_2 surface via two bidentate bridges on different bipyridines (c.f. model I2b). A model similar to H2b was previously introduced in Ref. 145.

The strong H-bonds of H2a have a dramatic effect on its O 1*s* spectrum, shown in Fig. 4.9. The 1*s* binding energies of hydroxyl O atoms belonging to the COOH group pointing away from the substrate remain the largest, appearing at

-0.4 eV. However the binding energies of the hydroxyls involved in H-bonding are lowered by 1.2 eV, while the binding energies of the carbonyl O atoms are raised by 0.1 eV. Correspondingly the separation of the two fitted gaussians reduces to 1.92 eV. The relative intensity is found to be 0.21, which is the smallest value of all the considered adsorption models. The reason for this small value is that the H-bonded hydroxyl O atoms are shifted so much that they contribute partly to the lower energy adsorbate peak.

For H2b, the weaker H-bond has less of an impact on the O 1*s* spectrum. The H-bonded hydroxyl is shifted to 0.4 eV lower binding energy than its non-H-bonded counterpart. The calculated separation of the adsorbate peaks for H2b is 2.24 eV, and their relative intensity is 0.25.

It is interesting to return to the energetics of adsorption displayed in Fig. 4.5, and note that H-bonds can significantly stabilise different adsorption modes. The effect in moving from I2b to H2b is small, only 0.02 eV. However the H-bonds formed in H2a increases the stability of I2a by 0.27 eV, so that H2a is the most stable of all models considered where two COOH groups form bonds with the TiO_2 substrate.

4.5.3 Long-range intermolecular interactions

Apart from the H-bonding, another factor has changed on moving from the interface models based on isolated dyes: the areal density of dye molecules on the surface has increased from 0.25 nm^{-2} to 0.8 nm^{-2} and 0.7 nm^{-2} for H2a and H2b respectively. It is important to quantify the effect on the calculated spectra of this increase in areal density, independent of the H-bonding. Figure 4.10 shows an interface model based on I2c where the areal dye density has been doubled to 0.5 nm^{-2}. There are now two dye molecules per unit cell, carefully arranged so

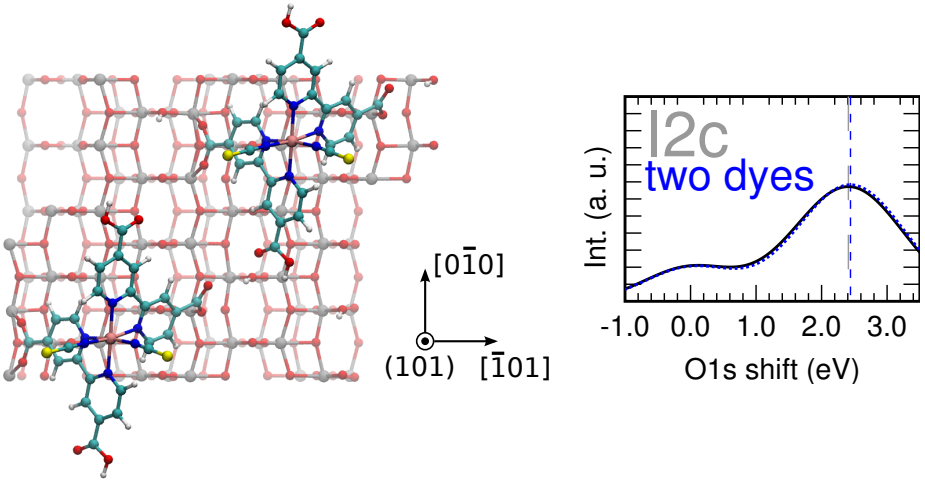

Figure 4.10: Ball-and-stick representation of model I2c with the areal dye density doubled. The O 1*s* spectra calculated at high and low density (blue and black lines) are effectively identical.

that the unadsorbed COOH groups do not interact.

The calculated O 1*s* spectra of I2c with the two different areal densities are also shown in Fig. 4.10. The spectra are effectively indistinguishable, leading to the conclusion that the 1*s* binding energies are sensitive only to the local bonding environment of the parent O atoms, and not to any long-range effects. Thus the changes in the O 1*s* spectra observed for H2a and H2b can be attributed solely to H-bonding.

A related, computational, point is that calculations using different simulation cell sizes provide a check of the validity of not truncating the $\frac{1}{R}$ interaction between periodic images. In H2a, the separation of the hydroxyl and carbonyl O atoms of the COOH group pointing away from the substrate (i.e. cis to the NCS ligands) is 2.55 eV. The corresponding separation in I2a is 2.56 eV, thus showing that changing both the size and shape of the simulation cell has a neglible effect on differences in binding energies. This result supports the idea that the dependence on unit cell size is cancelled when taking differences in total energies

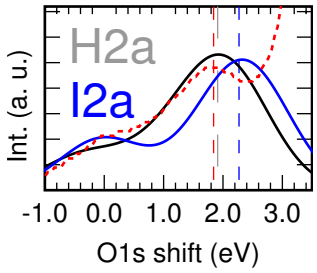

Figure 4.11: O 1*s* spectra calculated including escape depth effects for models H2a (black line) and I2a (blue line), compared to experiment (red line).

of charged interface models.

4.5.4 Escape depth effects

In calculating O 1*s* spectra and relative intensities, it was assumed that each O atom provides an equal contribution. Photoelectrons emitted from O atoms further above the TiO_2 surface have a better chance of reaching the detector. The electron escape depth λ introduced above can be used to estimate this effect, by weighting the contribution from each O atom by a factor $\exp(z/\lambda)$ where z is the height of the O atom above the substrate. Figure 4.11 shows the O 1*s* spectra calculated for I2a and H2a assuming a value of 15 Å for λ, which falls into the acceptable range of 3–20 Å given by the universal curve of Ref 169.

The exponential prefactor enhances the contribution of the unadsorbed COOH groups compared to those bound to the TiO_2 substrate. Since the hydroxyl O atoms which form the peak at higher binding energy are located on these unadsorbed groups, the relative strength of this peak is increased. The intensity ratios with escape depth included increase to 0.37 and 0.31 for I2a and H2, respectively. Of course the exponential prefactor is an extremely simplified model with a degree of arbitrariness introduced by the uncertainty in λ. Consequently not too much significance can be attached to these numbers, although the qualitative

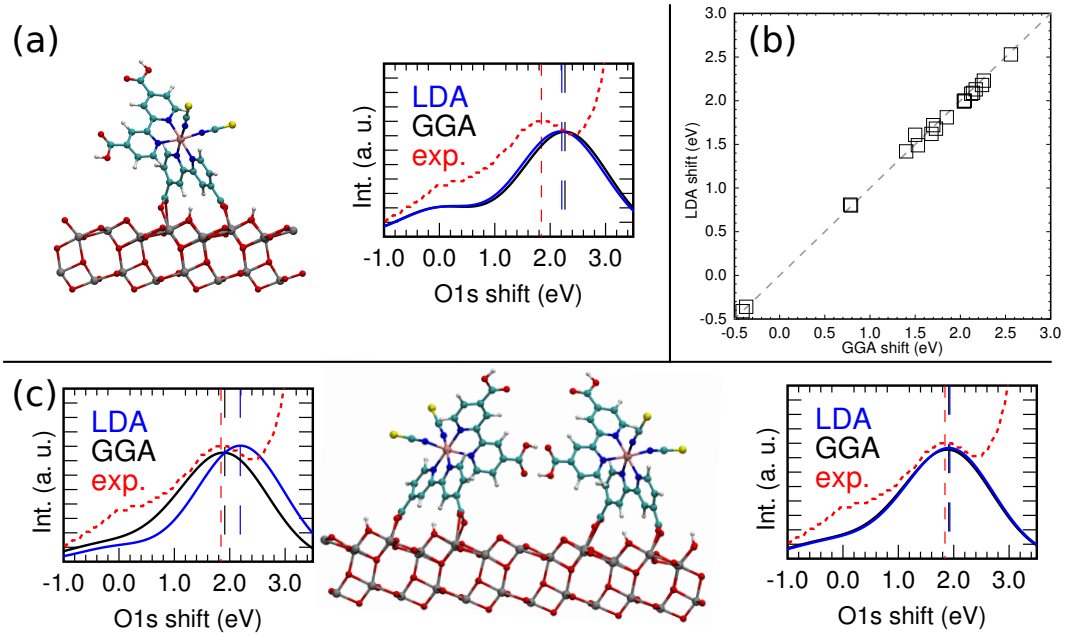

Figure 4.12: (a) The optimised structure and O 1*s* spectrum of model I2a, calculated in the LDA (blue line) compared to that calculated with the PBE functional (black line) and experiment (red line). (b) Comparison of O 1*s* shifts calculated within the LDA or with the PBE functional for the test set of molecules considered in Chapter 2 (c.f. Fig. 2.4). If the two methods produced identical results all points would lie on the diagonal line. (c) The optimised structure of H2a calculated in the LDA (centre). On the left the O 1*s* spectrum of H2a calculated with the LDA using LDA geometries (blue line) is compared to that calculated with PBE using PBE geometries (black line) and experiment (red line). On the right, the PBE geometry is used throughout. In this case the LDA and PBE-calculated O 1*s* spectra are indistinguishable.

improvement in lineshape is encouraging.

4.5.5 H-bonding and exchange-correlation functionals

A final check is to consider the influence of different exchange-correlation functionals when calculating the O 1*s* binding energies and the properties of H-bonded systems in general. Figure 4.12 compares the performance of the local-density approximation (LDA) with the PBE functional in different cases. First, the optimised geometry of interface model I2a was obtained in the LDA, and then the

O 1s spectrum calculated for this structure. Fig. 4.12(a) shows that LDA spectrum is effectively identical to that obtained with the PBE functional. Indeed, taking the set of molecules used to benchmark the calculations of 1s binding energies in Chapter 2, reoptimising their geometry in the LDA and recalculating the O 1s shifts finds an r.m.s. difference in shifts of less than 0.05 eV for the two functionals [Fig. 4.12(b); c.f. Fig. 2.4].

However, when the optimised structure of H2a is obtained in the LDA, the length of the H-bond decreases to 1.32 Å from its PBE value of 1.51 Å. The corresponding O 1s spectrum is rather different [Fig. 4.12(c)], with the separation of adsorbate peaks increasing by 0.3 eV in the LDA. The difference in O 1s spectra between PBE and LDA can be attributed solely to the different optimised geometry. If the LDA is used to calculated the O 1s binding energies with the PBE-optimised geometry [Fig. 4.12(c), right], the two spectra again are indistinguishable.

The question therefore is to determine which functional describes H-bonded structures more accurately. Once the structure is fixed, using LDA or PBE does not affect the calculation of the O 1s spectrum. The performance of the two functionals can be assessed through the benchmark system of the formic acid dimer. The formation energy per HCOOH molecule was calculated to be 0.67 eV in the LDA and 0.38 eV with the PBE functional. Meanwhile the high-accuracy coupled-cluster calculations of Ref. 172 found a formation energy of 0.30 eV per HCOOH molecule, showing that the LDA vastly overestimates the strength of the H-bonding. In the same study, the generalised-gradient PW91 functional was found to reproduce the coupled-cluster formation energies to within a 10% accuracy for a range of H-bonded structures. On this evidence, exchange-correlation functionals including gradient corrections provide a superior description of H-

bonding, justifying the use of geometries obtained with the PBE functional.

4.6 Conclusions

The purpose of the work presented in this chapter was to derive an atomistic model of the interface formed between the N3 dye molecule and mesoporous TiO_2 films, as found in dye-sensitized solar cells. The TiO_2 nanostructured film was approximated as a slab of anatase cut along the (1 0 1) direction. A set of six interface models were constructed where the N3 molecule formed bonds with the anatase surface through some of its carboxylic acid (COOH) groups. The most stable of these configurations was found to be a model where three COOH groups were involved in the bonding. However it was pointed out that stability may not be a sufficient criterion to determine a realistic interface model, since there may be energy barriers associated with forming different geometries.

Instead, an attempt was made to validate the adsorption models by calculating the O 1s binding energies at the interface and comparing the results to X-ray photoemission spectroscopic data. A quantitative disagreement was found between calculations and experiment for all six interface models, with calculations overestimating the separation between the two peaks in the O 1s spectrum formed by the adsorbate. By introducing H_2O molecules and also by considering previous work on formic acid, it was noted that H-bonding of COOH groups located far from the substrate might reduce the separation of these peaks. Two new interface models were constructed probing the strong and weak regimes of H-bonding, based on N3 dimers and chains, respectively. The H-bonded models showed a reduced separation of the adsorbate peaks, in line with the experimental measurements. Reconsidering the energetics of adsorption showed that H-bonds

could also have a significant effect, stabilising configurations by 0.27 eV in the case of dimers.

On these results, it would appear that H-bonding may play an important role in determining the structure of the interface. Clearly only two H-bonded models have been considered here, based on heterogenously adsorbed dye molecules (I2a→H2a, I2b→H2b), but more complex H-bonded supramolecular assemblies can be imagined, based on mixing of single-molecule configurations.

Convincing evidence of the formation of large H-bonded structures could be found in STM experiments. As mentioned previously these experiments are highly challenging, in part due to the difficulty in preparing a suitable anatase (1 0 1) surface [173] and then applying molecules in sufficiently clean conditions [174]. However it is interesting to consider the STM experiment of Ref. 161, where images of N3 dyes on the rutile (1 1 0) show a clustering of molecules on the surface. The preferred nearest neighbour distance lies in the range 1.4–1.6 nm, as determined by the corresponding autocorrelation function. For comparison the Ru–Ru separation calculated for H2a is 1.6 nm (of course, calculated for a different TiO_2 surface). In a different experiment [162] the N3 molecules appear as 1.8 nm wide ovals, raising the possibility that these features are actually unresolved dimers.

From the point of view of solar cell performance, two questions arise. First, DSCs based on N3 [36] normally employ a liquid electrolyte to regenerate the oxidised dye. It would be interesting to learn whether the possible H-bonded assemblies would remain stable in the presence of this electrolyte. Second, it is important to understand the effect of H-bonding on cell performance, particularly on charge injection mechanisms and energy-level alignment. H-bonded aggregation is generally thought to hamper cell performance [175]. However given that N3 is one of the highest-performing sensitizers, if it were to turn out that H-

bonding is an essential feature of its binding to TiO_2 it is possible that forming larger H-bonded structures may be more beneficial to DSC performance than traditionally thought.

Chapter 5

Electronic properties of bulk TiO_2 and the N3 molecule

Having addressed the atomistic structures of N3 and TiO_2, I now move to their electronic properties. As discussed in Chapter 3, it is necessary to go beyond density-functional theory in order to obtain information about the excited-state properties of a system, e.g. its fundamental gap. The optimum methods of calculating the quasiparticle properties of N3 (an isolated molecule) and TiO_2 (a bulk solid) are different, and as such this chapter is divided into two halves. The first part deals with the electronic structure of TiO_2, particularly of anatase, in the GW approximation. Here it is shown that the inclusion of Hubbard U corrections in the DFT Hamiltonian quantitatively affects the GW quasiparticle energies. The second part takes the ΔSCF method discussed in Chap. 2 and applies it to the N3 molecule. The electronic structure of the entire N3/TiO_2 interface is the subject of the following chapter.

The work on TiO_2 described in the first half of this chapter was previously published in Ref. 176.

5.1 The electronic structure of anatase in DFT

5.1.1 Introduction and computational approach

As discussed in Chapter 3, the single-particle Kohn-Sham (KS) eigenvalues and eigenstates do not formally describe the excited-state properties of a system. However they do provide the initial guess in a perturbative approach, and as such it is appropriate to begin with a study of the electronic structure of TiO_2 obtained in density-functional theory. To facilitate comparison with other work, calculations were performed on the experimental structures of anatase [139] and rutile [140] TiO_2 unless otherwise stated. The PBE functional [54] was used to describe exchange-correlation and the core-valence interaction described with norm-conserving pseudopotentials [64]. The pseudopotential for Ti was generated with the Ti ion in the 4+ state and the semicore $3s$ and $3p$ electrons explicitly included in the valence. The wavefunctions were expanded in plane waves up to a cutoff of 200 Ry, and in the self-consistent calculations of the charge density the Brillouin zone was sampled on a $6 \times 6 \times 6$ Monkhorst-Pack grid. All DFT calculations were performed with the `Quantum ESPRESSO` software package [141].

Due to its technological importance in dye-sensitized solar cells (c.f. Chapter 4) the main focus here will be on the properties of the anatase polymorph of TiO_2.

5.1.2 Band structure and partial density-of-states

The band structure of anatase TiO_2, obtained by calculating the KS energies along high-symmetry directions in the Brillouin zone, is shown in Figure 5.1. Anatase is an indirect-gap semiconductor in DFT with the conduction band minimum (CBM) at the Γ-point and the valence band maximum (VBM) at a point close to X. This position of the VBM is rather inconvenient, especially for *GW*

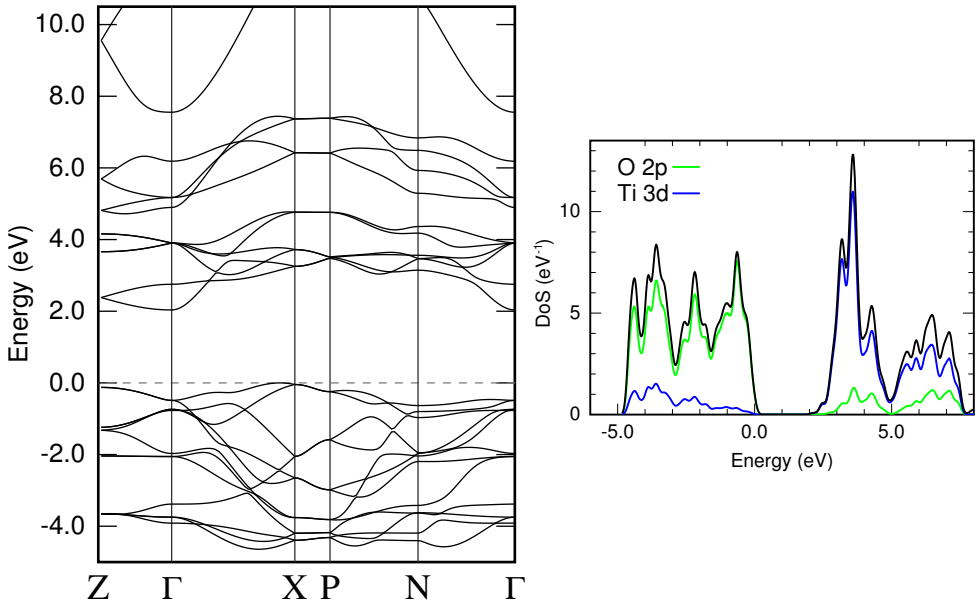

Figure 5.1: Band structure (left) and partial density-of-states calculated in DFT for anatase TiO_2. In units of reciprocal lattice vectors, the co-ordinates of the special k-points are $Z = 0\ 0\ \frac{1}{2}$, $X = \frac{1}{2}\ \frac{1}{2}\ \frac{1}{2}$, $P = \frac{1}{2}\ \frac{1}{2}\ \frac{3}{4}$ and $N = \frac{1}{2}\ 0\ \frac{1}{2}$. The energy zero has been set to the top of the valence band lying between X and Γ. In the PDoS plot the δ-functions were approximated by gaussians of width 0.1 eV.

calculations which often are performed on regular k-meshes. On the other hand the KS energy of the highest occupied state at X differs from the "true" VBM by less than 0.06 eV. Therefore in the following the difference is ignored and the analysis focuses on the highest occupied state at X. The calculated X–Γ gap is 2.08 eV. The smallest direct gap is 2.37 eV and is located between Z and Γ.

To assess the character of the conduction and valence bands it is useful to define a partial density-of-states (PDoS) by projecting the KS orbitals ψ_{nk} onto the pseudo-atomic orbitals ϕ_{Iml}:

$$g_{Iml}^{\mathrm{PDoS}}(E) = \sum_{nk} \langle \phi_{Iml} | \psi_{nk} \rangle \delta(E - \varepsilon_{nk}) \tag{5.1}$$

Here I refers to the atom type, m the principal quantum number and l the angular momentum channel. Summing over the contributions from a complete

set of projection operators recovers the standard density-of-states (DoS):

$$g^{\mathrm{DoS}}(E) = \sum_{nk} \delta(E - \varepsilon_{n,k}) \tag{5.2}$$

Fig. 5.1 shows the DoS for the valence and conduction bands (black line), projected onto the $2p$ states of the O atoms (green line) and the $3d$ states of the Ti atoms (blue line). The Ti $3d$ and O $2p$ states entirely account for these two bands; the former dominate the conduction band, the latter the valence. The conduction band further displays two sub-bands spanning 2–5 eV and 5–8 eV. The Ti $3d$ orbitals forming these sub-bands are of t_{2g} and e_g character, respectively [177].

The next step is to take the calculated KS eigenstates and eigenvalues and apply *GW* corrections to obtain quasiparticle energies.

5.2 *GW* corrections to the DFT bandstructure

5.2.1 Computational methodology

The quasiparticle corrections to the DFT band structure were calculated through the scheme first introduced in Ref. 118. The self-energy operator Σ was split as $\Sigma_X + \Sigma_C$, where Σ_X is the frequency independent bare-exchange contribution and Σ_C accounts for correlation effects (Chap. 3). Σ was expanded in plane waves, up to cutoffs of 80 Ry and 10 Ry for Σ_X and Σ_C respectively.

The frequency dependence of the screened Coulomb interaction was described by the Godby-Needs plasmon pole model [125], where the polarisability was calculated at ω=0 and $i\omega_P$. ω_P=23 eV was chosen to match the experimentally-observed TiO_2 plasmon frequency [178]. Both the polarisability and the Green's

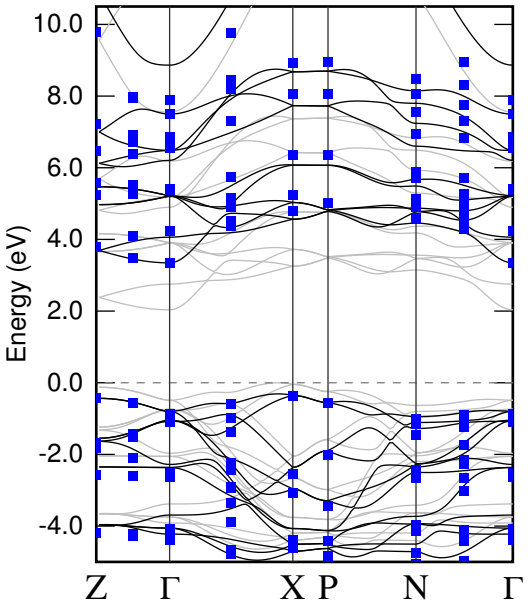

Figure 5.2: The band structure of anatase TiO_2 including G_0W_0 corrections (blue squares). As in Fig. 5.1 the energy zero was set to the top of the valence band calculated in DFT (light grey lines). The black lines are the DFT bands with rigid shifts of -0.31 eV or 1.31 eV applied to the occupied and unoccupied states respectively.

function were constructed from the KS eigenstates obtained on a uniform, unshifted 4×4×4 Brillouin zone mesh, and 568 unoccupied bands were included in both sums over conduction states (the convergence with respect to the number of unoccupied bands is discussed below). All *GW* calculations were performed using the `SaX` code [114].

5.2.2 Quasiparticle corrections in the G_0W_0 approximation

Figure 5.2 shows the quasiparticle energies calculated in the G_0W_0 approximation with equation 3.57. The DFT bands are shown as light grey lines, and the quasiparticle energies are shown as blue squares.

The effect of the G_0W_0 corrections is to open the gap by over 1.5 eV. The $X \rightarrow \Gamma$ gap is calculated to be 3.70 eV while the direct gap at the point midway

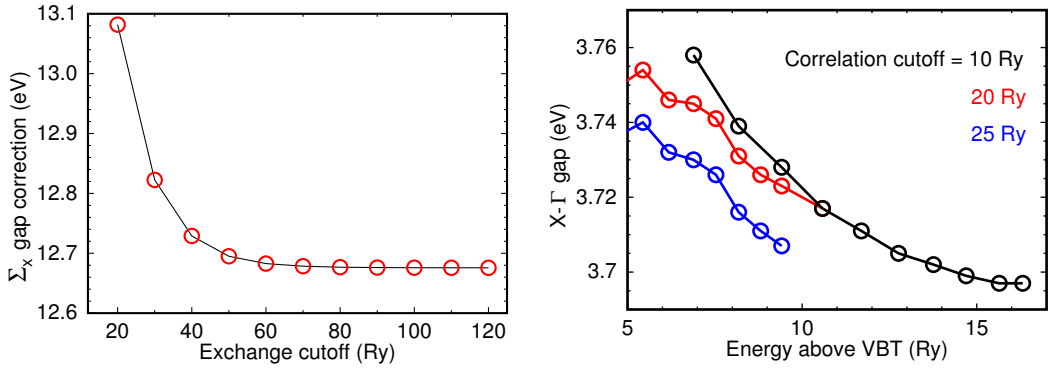

Figure 5.3: Convergence of matrix elements of the self energy operator Σ. The left plot shows the convergence of $\langle\psi_{\Gamma_{25c}}|\Sigma_X|\psi_{\Gamma_{25c}}\rangle - \langle\psi_{X_{24v}}|\Sigma_X|\psi_{X_{24v}}\rangle$ with the number of planes waves used to describe Σ_X. $\psi_{X_{24v}}$ and $\psi_{\Gamma_{25c}}$ are the KS states at the valence and conduction band edges, respectively. The right plot shows the convergence of the G_0W_0 gap as a function of plane wave cutoff for Σ_C (black, red, blue symbols) and the number of unoccupied bands used to construct the polarisability and Green's function. The lines are guides to the eye.

between Z and Γ is 4.03 eV. The main contribution to the gap opening is from the conduction states shifting up in energy by 1.31 eV, while the downshift of the valence states is smaller at 0.31 eV.

Interestingly, aside from the increased gap, the widths of the bands are largely unchanged on applying the quasiparticle corrections. The black lines in Fig. 5.2 again are the DFT bands, but with rigid shifts of -0.31 eV or 1.31 eV applied to the occupied and unoccupied states respectively so that the DFT and quasiparticle energies match at the band edges. Inspection of the figure shows that the scissor-shifted DFT valence band reproduces the quasiparticle energies rather well, while the conduction band widths only differ by 0.2 eV.

5.2.3 Convergence behaviour

It is interesting to consider the convergence behaviour of the different contributions to the quasiparticle energies. The exchange part of the self-energy Σ_X only

involves occupied states, and displays straightforward convergence with plane wave cutoff (Figure 5.3). Indeed the computational effort involved in computing Σ_X is relatively light, so working at the cutoffs between 40–120 Ry is not prohibitive.

The quasiparticle energies calculated with equation 3.57, which include Σ_C and $\frac{d\Sigma_C}{dE}$, display more complicated convergence behaviour. Constructing the polarisability and Green's function requires two separate sums over an (in principle) infinite number of unoccupied bands, while the computational workload increases dramatically with the number of plane waves used to describe Σ_C. The right plot of Fig. 5.3 shows the convergence of the $X \rightarrow \Gamma$ gap with respect to these two parameters. For the 10 Ry plane wave cutoff, increasing the number of unoccupied bands from 296–568 (equivalent cutoff of 10.6–16.3 Ry) reduces the band gap by 0.02 eV. Meanwhile for a fixed number of unoccupied bands increasing the plane wave cutoff to 25 Ry also reduces the gap by 0.02 eV.

For a 25 Ry cutoff it is prohibitive to go above 256 unoccupied bands with current computational power. Therefore for this work the 10 Ry cutoff with 568 unoccupied bands was deemed the best compromise. It should be noted that the convergence behaviour of *GW* calculations can be the source of controversy (c.f. the calculations of Refs. [126; 127] on ZnO), while removing the sum over unoccupied states in *GW* calculations is the subject of current research efforts [121; 128–130].

5.2.4 Comparison to previous calculations and experiment

The calculated indirect gap of 3.70 eV compares well with previous G_0W_0 calculations on anatase, which yielded 3.61 eV [179], 3.83 eV [180], 3.7 eV [181], 3.73 eV [182] and 3.79 eV [183]. As discussed in Chap. 3 the energies calculated

in *GW* correspond to the addition or removal of electrons and should therefore be compared to measurements made in photoemission and inverse photoemission experiments. Unfortunately there is a lack of inverse photoemission data on anatase in the literature meaning that this *quasiparticle* gap is not known. By contrast the *optical* gap of anatase, that is, the energy required to excite an electron from the valence into the conduction band, has been measured in a number of studies (Ref. 184 and references therein) to be indirect at a value of 3.2 eV.

The optical gap is generally expected to be smaller than the quasiparticle gap, since the former includes the attractive interaction of the electron-hole pair (exciton). Calculations of the optical absorption including the exciton with the Bethe-Salpeter equation and G_0W_0 found the fundamental transition to occur at 3.57 eV [182], showing that it is unlikely that the exciton accounts for the entire 0.4–0.6 eV difference between the calculated quasiparticle and measured optical gaps. Alternatively, increasing the plane wave cutoff of Σ_C and number of unoccupied bands will reduce the band gap, but Fig. 5.3 indicates this will be of the order of 0.1 eV.

One potential flaw of the calculations is that they do not take the quantum motion of the ions (electron-phonon interaction) into account. In diamond including electron-phonon corrections has been shown to have a remarkable effect, closing the static-ion band gap by more than 0.6 eV even at zero temperature [185; 186]. However these calculations are still rather novel and have yet to be applied to more complex systems like TiO_2.

Another possibility is that the standard G_0W_0 approach is not sufficient in the case of TiO_2. The success of G_0W_0 as implemented above rests on the ability of DFT to give a good approximation to the quasiparticle wavefunctions. But the conduction band of TiO_2 is formed from Ti $3d$ states (Fig. 5.1) which are

not necessarily well-described in DFT. In Chapter 2 the DFT+U approach was introduced, where correlations between d electrons are taken into account with a Hubbard U parameter. A Hamiltonian including U corrections may provide a better starting point for GW for TiO_2. Indeed this approach (known as $GW+U$, GW@DFT+U or simply GWU) was previously shown to produce gaps smaller than GW for a number of oxides [86]. In the following section the GWU approach is applied to anatase TiO_2.

5.3 Inclusion of Hubbard U corrections; GWU

5.3.1 Introduction to the procedure

The central concept of GWU is simple. Rather than constructing the Green's function and screened Coulomb interaction from the KS eigenstates calculated in standard DFT, the states obtained in DFT+U are used instead. However there is now a parameter in the calculations, the Hubbard U, which introduces an arbitrariness into the proceedings. Previous calculations on Ti-based oxides employed values of U ranging from 2–8 eV (Ref. 187 and references therein) depending on the property under investigation.

Here, U is chosen to satisfy the following criterion: upon applying GW corrections to the DFT+U electronic structure, the fundamental band gap does not change. This approach, previously demonstrated for BCC hydrogen [188], is the natural choice when working in perturbation theory; the optimum starting Hamiltonian is the one that leads to the smallest quasiparticle corrections.

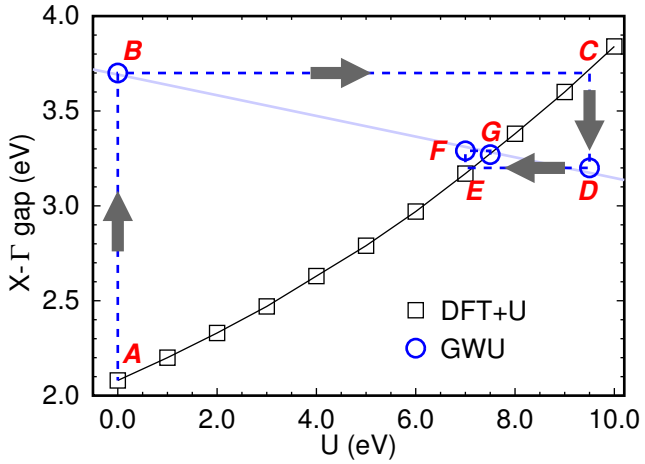

Figure 5.4: The X–Γ gap of anatase TiO_2 calculated with DFT including Hubbard U corrections (DFT+U), for different values of the Hubbard U parameter (black squares). The blue circles are the gaps calculated in a GW calculation starting from DFT+U eigenvalues and eigenstates (GWU). The arrows and letters illustrate the procedure of determining an optimum U, as described in the main text. The lines are guides to the eye.

5.3.2 GWU

The optimum value of U is determined in the iterative procedure illustrated in Figure 5.4. Here, the rotationally invariant formulation of DFT+U is used (Ref. 85) with the Ti 3d pseudo-wavefunctions employed as projectors. The black squares in Fig. 5.4 are the X–Γ gaps calculated for different values of U. The gap increases monotonically with U, and as found in previous calculations [189] a value of U between 7–7.5 eV reproduces the experimental optical gap of 3.2 eV.

The first step, labelled A→B in the figure, is to perform a G_0W_0 calculation starting from U=0 eV, as described already in Section 5.2.2. The gap opens from 2.08 eV to 3.70 eV. Next, following the path B→C finds that a DFT+U calculation with U=9.5 eV has the same 3.70 eV band gap. A G_0W_0 calculation starting from U=9.5 eV (C→D) actually reduces the X–Γ gap, to 3.20 eV. This gap corresponds to U=7.0 eV (D→E), and the subsequent G_0W_0 calculation (E→F)

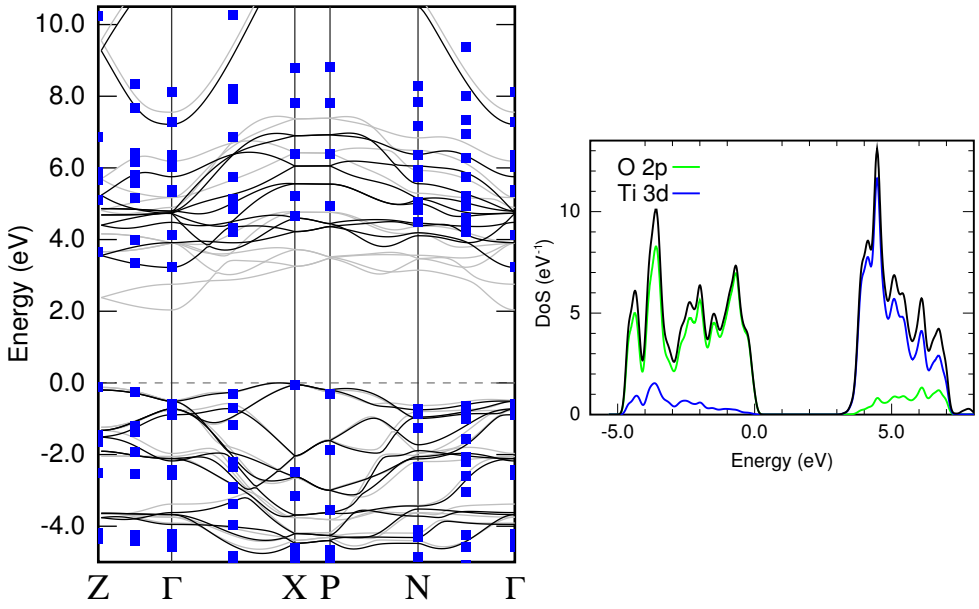

Figure 5.5: Band structure and PDoS of anatase TiO_2 calculated in DFT+U with U=7.5 eV. The black lines in the band structure plot are the DFT+U bands, while the blue squares are the GWU-calculated energies. The light grey lines are the DFT bands. Note that all three datasets have been aligned here to co-incide at the valence band edge; as discussed in the text DFT+U consistently yields energies which are ∼0.6 eV higher than in GWU.

opens the gap to 3.29 eV. Finally, setting U=7.5 eV (point G) yields identical band gaps of 3.27 eV in both DFT+U and GWU. Thus the U parameters follow the converging sequence 0.0→9.5→7.0→7.5 eV, with corresponding GWU band gaps of 3.70→3.20→3.29→3.27 eV.

5.3.3 Electronic structure at the optimum U

According to the criterion introduced in Section 5.3.1, the optimum value of the Hubbard parameter U is 7.5 eV. Figure 5.5 shows the band structure and PDoS obtained in DFT+U and the quasiparticle energies calculated with GWU (c.f. Figs. 5.1 and 5.2) for U=7.5 eV. Considering the PDoS first, the effect of the U term is to raise the energy of the t_{2g} sub-band, reducing the overall width of the

Anatase TiO_2

	DFT		*GW*		DFT+*U*		*GWU*	
X_{24v}	0.00	(0.00)	-0.31	(-0.30)	0.48	(0.49)	-0.14	(-0.13)
Γ_{25c}	2.08	(2.06)	3.39	(3.38)	3.75	(3.70)	3.13	(3.07)
E_g	2.08	(2.06)	3.70	(3.68)	3.27	(3.21)	3.27	(3.20)

Rutile TiO_2

	DFT	*GW*	DFT+*U*	*GWU*
Γ_{24v}	0.00	-0.19	0.59	0.08
Γ_{25c}	1.82	3.21	3.42	2.93
E_g	1.82	3.40	2.83	2.85

Table 5.1: Energies of critical points of anatase and rutile TiO_2 calculated using various methods: plain density-functional calculations (DFT), calculations including Hubbard U corrections U =7.5 eV (DFT+U), G_0W_0 calculations starting from the DFT (*GW*) and from DFT+U (*GWU*). All values are in eV. Experimental lattice paramaters are used throughout except for the values given in brackets, which are calculated at optimised lattice parameters.

conduction band from 6 eV (U=0 eV) to 4 eV. Interestingly, on applying *GWU* corrections (blue squares in left panel of Fig. 5.5) the conduction band width opens up again. Indeed apart from the DFT+U and *GWU* energies coinciding at the valence (conduction) edges at X (Γ) by construction, the agreement between the black lines and blue squares is not as close as found for basic *GW* in Fig. 5.2.

Table 5.1 further compares DFT+U and *GWU* by considering the individual quasiparticle corrections at the top of the valence band at X (X_{24v}) and the bottom of the conduction band at Γ (Γ_{25c}). Although in Fig. 5.5 the DFT+U and *GWU* energies were aligned at X_{24v} for clarity, Table 5.1 shows that DFT+U in fact consistently yields energies which are ∼0.6 eV higher than in GWU.

Table 5.1 explores two further aspects. First, instead of using experimental lattice parameters the structures calculated from first principles can be used instead. The numbers in brackets in Table 5.1 were calculated at the lattice parameters optimised in DFT, a=3.83 Å, c=9.84 Å and u=0.206 (these numbers differ by 0.1 Å from the values presented in Table 4.2 calculated with the ultrasoft

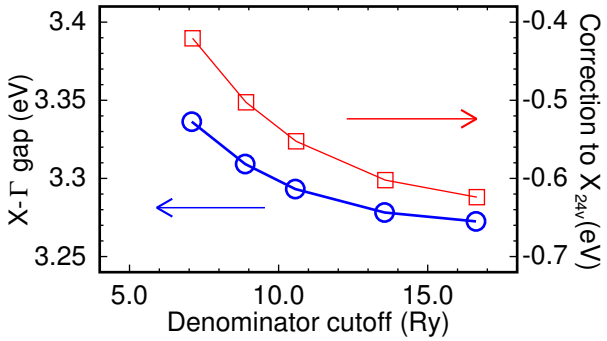

Figure 5.6: Convergence of the X–Γ gap (blue circles, left scale) and the correction to energy of the valence band top at X (red squares, right scale) with the number of unoccupied bands used to construct the polarisability and Green's function.

pseudopotentials). The choice of theoretical versus experimental parameters lead to differences smaller than 0.1 eV.

Second, the transferability of U=7.5 eV can be tested by considering the electronic structure of rutile. In DFT and GWU rutile has a direct gap at Γ, although the conduction band minima at Γ, M and R are within 0.06 eV of each other, and in DFT+U and standard GW the ordering switches. Table 5.1 presents the energies at Γ only. The direct gaps calculated in DFT+U and GWU are 2.83 and 2.85 eV respectively, showing that the criterion for the optimal U is reasonably well-satisfied in rutile. As for anatase, the corrections to the individual eigenvalues calculated in DFT+U are $\sim$0.5 eV higher than in GWU.

5.3.4 Convergence of quasiparticle corrections in GWU

As before it is important to check the convergence of the GWU corrections. Figure 5.6 shows the X–Γ gap (blue) and correction to the top of the valence band (red) with the number of unoccupied bands used to construct the Green's function and polarisability, using the 10 Ry cutoff to describe Σ_C. Exactly as found for the GW calculations in Sec. 5.2.2 increasing the equivalent energy cutoff from 10.6

Ryd (296 conduction bands) to 16.6 Ryd (568 bands) reduces the bandgap by 0.02 eV. Additionally Fig. 5.6 also demonstrates that the individual corrections to band edges converge more slowly than to gaps (note the different scales), as was shown in Ref. 179 for rutile.

5.3.5 Summary for TiO_2

Using the GWU method with the optimal U of 7.5 eV finds a value of 3.27 eV for the indirect gap of anatase TiO_2. This is a 0.43 eV reduction from the value of 3.70 eV obtained in a G_0W_0 calculation starting from standard DFT, and is closer to the experimentally-measured optical gap of 3.2 eV [184]. Using optimised instead of experimental lattice parameters has a small effect, reducing the gap by just under 0.1 eV.

Considering rutile, the GWU gap of 2.85 eV is technically compatible with the experimental quasiparticle gap [190] of 3.3 eV, once the uncertainty of ± 0.5 eV estimated by the authors of that work is included. However 2.85 eV is smaller than the widely-quoted direct optical gap of rutile of 3.0 eV [184], although it is still closer than the gap of 3.4 eV calculated in standard G_0W_0.

This section concludes the investigation of the electronic structure of TiO_2. The remainder of the chapter considers the electronic structure of the sensitizing molecule, N3.

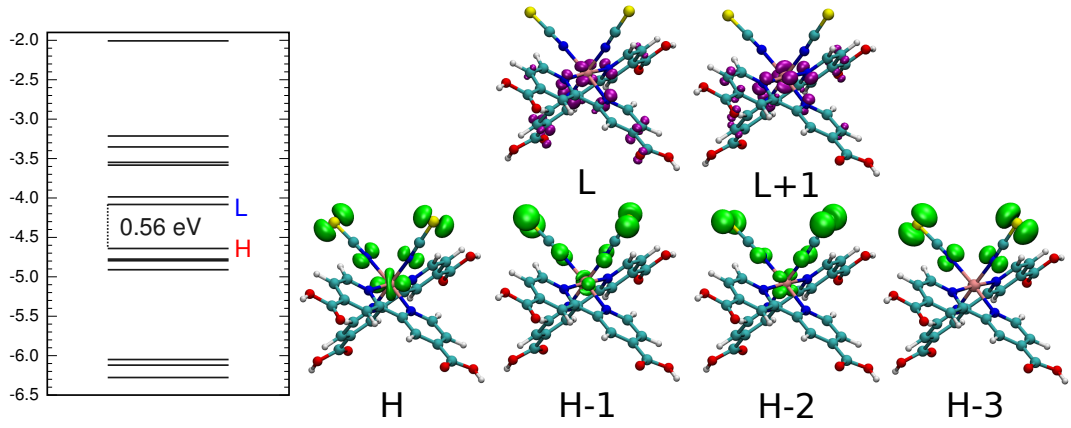

Figure 5.7: Kohn-Sham (KS) energy levels calculated for the N3 molecule (left) and isosurface plots of the frontier orbitals obtained in DFT (right). The KS levels are referred to vacuum and are in eV, and the HOMO and LUMO (H and L) energies are indicated. The isosurface plots were constructed with isovalues of 0.005 electrons/bohr^3 both for occupied (green) and unoccupied (purple) states.

5.4 Electronic structure of N3

5.4.1 DFT

Figure 5.7 shows the KS energies and states calculated for the N3 molecule in its relaxed structure, as obtained in Section 4.2.2. The same computational paramenters were used as for the relaxation (ultrasoft pseudopotentials, the PBE functional for exchange-correlation, plane wave cutoffs of 35 and 200 Ry for wavefunctions and density, truncation of the Coulomb interaction). The HOMO-LUMO gap, that is, the difference in energies between the highest occupied and lowest unoccupied molecular orbitals, is calculated to be 0.56 eV in DFT. The next lowest-energy occupied states (HOMO-1,2,3) fall within a 0.3 eV energy window below the HOMO, while the next highest-energy unoccupied state (LUMO+1) is only 0.1 eV above the LUMO.

The isosurface plots displayed in Fig. 5.7 show that the HOMO–HOMO-3 lie on the central Ru atom and the NCS ligands, consisting of Ru 4*d*, N 2*p* and S 3*p*

contributions. The LUMO and LUMO+1 are mainly found on the bipyridines and the Ru atom, consisting of Ru $4d$ and C, N and O $2p$ characters.

The calculated electronic structure is in good quantitative and qualitative agreement with the BPW91 (i.e. GGA) calculations of Ref. 191. In that work the HOMO-LUMO gap was calculated to be 0.50 eV. Comparing to experiment is more difficult. Ideally the HOMO-LUMO gap should be taken as the difference in ionisation potential and electron affinity of the molecule in the gas phase. However the non-volatility of N3 means that experiments are performed in solution or thick films, while generally it is the optical absorption that is measured. The UV-vis experiments of Ref. 153 found the absorption onset to occur at 2.49 eV for N3 dissolved in H_2O. Meanwhile photoemission and inverse photoemission experiments provided estimates for the HOMO-LUMO gap of N3 films on anatase and rutile TiO_2 of 3.1–3.3 eV [192].

The solvated, optical gap includes both the electron-hole interaction and the dielectric screening of the solvent, which both tend to reduce the gap. As such 2.49 eV is a rigorous lower limit to the HOMO-LUMO gap. The values of 3.1–3.3 eV do not include the exciton and thus may be considered more reliable estimates, but are still are affected by the long and short-range interactions of the sensitizer with the substrate, discussed in detail in the next chapter.

5.4.2 ΔSCF

The previous section indicated that DFT underestimates the HOMO-LUMO gap of N3 by at least 2 eV, but in Chapter 3 it was demonstrated the ΔSCF method provided accurate values for the ionisation potentials of a range of molecules. Applying the same method to the N3 molecule yields an ionisation potential and electron affinity (I.P. and E.A.) of 6.14 and 2.71 eV respectively, and hence a

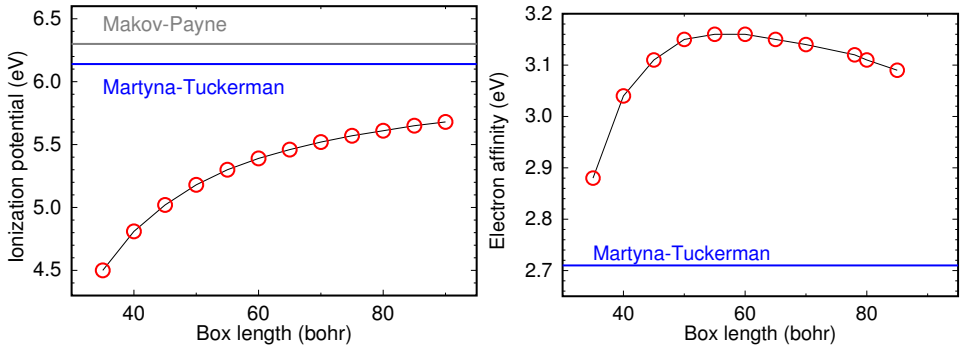

Figure 5.8: The ionisation potential and electron affinity (I.P. and E.A.) calculated without any truncation of the Coulomb interaction for different sizes of cubic simulation cell (red circles). The blue lines are the values calculated with the Martyna-Tuckerman truncation scheme [69]. The black line in the plot of the I.P gives the asymptote of the Makov-Payne expression (equation 5.3).

HOMO-LUMO gap of 3.43 eV. This value is compatible both with the photoemission/inverse photoemission measurements of 3.1–3.3 eV [192] and the optical absorption lower bound of 2.49 eV [153].

Comparing the ΔSCF I.P. and E.A to the KS HOMO and LUMO in Fig. 5.7 (all referred to vacuum) gives the quasiparticle corrections to the frontier orbital energy levels. The quasiparticle correction for the HOMO is $-6.14-(-4.64)=-1.50$ eV, and for the LUMO it is $-2.71-(-4.08)=+1.37$ eV.

5.4.3 The importance of the Coulomb truncation

This chapter ends on a technical point, which highlights the importance of the Coulomb truncation scheme when employing ΔSCF calculations to obtain the energies of frontier orbitals. Figure 5.8 shows explicit calculations of the I.P. and E.A. in cubic simulation cells of different sizes with no truncation scheme employed (circles). The I.P. converges slowly with box size, and can be fitted to

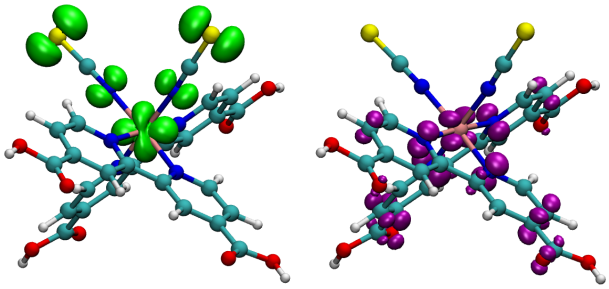

Figure 5.9: Isosurface plots of the spin density [i.e. $\rho^{\mathrm{up}}(\mathbf{r}) - \rho^{\mathrm{down}}(\mathbf{r})$] for the N3 molecule with one electron removed (left, green) or added (right, purple). The same isodensity is used as in Fig. 5.7 (0.005 electrons/bohr^3).

a Makov-Payne expansion [68]:

$$\text{I.P.} = A_0 + \frac{A_1}{L} + \frac{A_2}{L^3} + \frac{A_3}{L^5} \tag{5.3}$$

where L is the length of the simulation cell and the A_ns are coefficients. The asymptotic value A_0=6.30 eV is slightly larger than 6.14 eV, calculated when the spurious Coulomb interaction is removed via the Martyna-Tuckerman truncation scheme [69], as shown by the horizontal lines in the figure.

However the non-truncated E.A. displays strange, non-monotonic behaviour as the box size increases (right of Fig. 5.8). The E.A. initally increases, hits a peak value of 3.16 eV at a L=55 bohr, then decreases again. An explanation of this phenomenon is provided by inspecting Figure 5.9, which shows isosurfaces of the spin density for N3 with one electron added or removed when the Coulomb truncation is employed. As expected, the spin densities match the KS HOMO/LUMO isosurfaces shown in Fig. 5.7. If the truncation scheme is not used, the spin density of the molecule with an electron removed (used to determine the I.P.) has the same form as in Figs. 5.9 and 5.7. However the spin density of the molecule with an electron added shows a marked difference from the DFT LUMO, instead showing a spin-polarised state with a new concentration of charge

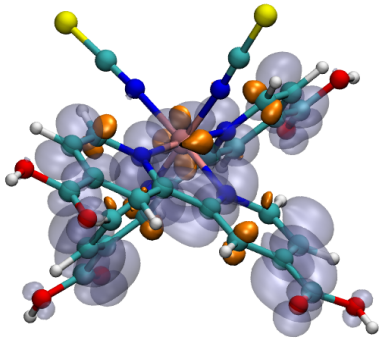

Figure 5.10: Isosurface plots of the spin density of the N3 molecule with one electron added with no truncation of the Coulomb interaction. The calculation was performed in a cubic simulation cell of side length 50 bohr. The two isosurfaces correpond to ± 0.001 electrons/bohr^3, (transparent blue for positive, orange for negative spin density). The plot shows a redistribution of charge on the Ru and C atoms.

on the Ru atom (Figure 5.10). Therefore removing the spurious Coulomb effects as a post-processing step, such as with the Makov-Payne correction, is insufficent in this case; it is essential to self-consistently remove the interaction between periodic images from the outset.

5.5 Conclusions

This chapter has dealt with the electronic structure of bulk anatase TiO_2 and of the N3 molecule in the gas phase. The band gap of the semiconductor and HOMO-LUMO gap of the molecule were found to be 2.08 and 0.56 eV in density-functional theory, which are both substantially smaller than the available experimental data, showing it necessary to go beyond DFT in order to obtain the excited-state electronic properties.

Different methods were used to tackle the two systems. For the N3 molecule, the ΔSCF method was used to obtain the quasiparticle corrections to the frontier orbital energy levels. The calculated quasiparticle gap was 3.43 eV, which is

compatible with photoemission measurements on adsorbed films [192].

The quasiparticle properties of bulk TiO_2 were investigated in the G_0W_0 approximation. The indirect gap of anatase was calculated to be 3.70 eV, somewhat larger than the gap of 3.2 eV measured in optical experiments [184]. The dominant presence of Ti 3*d* states in the conduction band prompted the idea of using a Hamiltonian which included Hubbard U corrections to obtain the starting wavefunctions and energies for GW. An optimal U parameter of 7.5 eV was determined at which the DFT+U and GW-corrected gaps were the same value of 3.27 eV. The same U parameter yielded a GWU quasiparticle gap of 2.85 eV for rutile which is slightly smaller than the experimentally-measured optical gap of 3.0 eV [184].

The importance of the starting Hamiltonian in GW calculations is an active area of research. Including U corrections [86; 188] or including exact exchange through hybrid functionals [193] has been shown to have a large effect on the GW-calculated gaps. Clearly it is desirable to have a methodology which always converges on the same result, regardless of starting point. This is the goal of self-consistent GW methods, e.g. Refs. 194 and 195.

The calculated gap for anatase is certainly closer to the experimental optical gap. It would be interesting to include excitonic effects on top of the GWU approach. The other important unresolved question is the role of electron-phonon renormalisation, which may further close the calculated gap.

Chapter 6

Energy-level alignment at the N3/TiO_2 interface

The aim of this chapter is to bring together the work on the atomistic and electronic structure of the N3/TiO_2 interface, and calculate the quasiparticle energy-level alignment. I show that standard DFT and DFT+U both fail to explain experimental measurements of the valence photoemission spectrum. Accordingly I describe a new theoretical approach which includes many-body effects, image-charge and finite slab corrections, configurational disorder and thermal broadening. Applying this approach to the N3/TiO_2 interface yields a photoemission spectrum in good agreement with experiment.

This chapter is an expansion of the results previously published in Ref. 196.

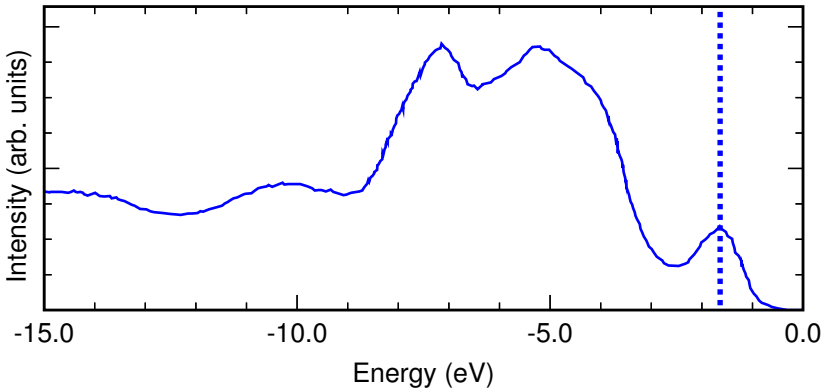

Figure 6.1: The photoemission spectrum measured for an N3-sensitized anatase TiO_2 film, as reported in Ref. 48. The incident photon beam was of energy 454 eV and generated by the synchrotron source at the Swedish National Laboratory in Lund. The energy axis is given with respect to the Fermi level of the sample. The dotted line at -1.64 eV is the peak assigned to the HOMO of the N3 molecule.

6.1 Photoemission spectroscopy at the N3/TiO_2 interface—basic considerations

6.1.1 Experimental measurements

The valence photoemission spectrum of N3-sensitized anatase TiO_2 films has been measured in a number of studies [48; 197–200]. The most recent measurement, reported in Ref. 48, is shown in Figure 6.1. The spectrum consists of a clear peak at -1.6 eV, a strong band spanning energies between -9 and -3 eV, and weaker features at higher binding energy. Generally the peak at -1.6 eV is assigned to photoemission from the N3 dye's highest occupied molecular orbital (HOMO), the wide band below -3 eV as the valence band of TiO_2, and the higher-energy features as photoemission satellites [46].

The TiO_2 valence band edge can be estimated by extrapolating the onset of the valence band feature at -3 eV. Then, comparison to the position of the HOMO peak (the dotted line in Fig. 6.1) gives the energy separation of the

HOMO and valence band top (HOMO/VBT offset). The values reported for the HOMO/VBT offset for the N3/TiO_2 interface are reasonably consistent between different experiments, being 1.6 eV [48; 197], 1.2 eV [199] and 1.4 eV [198; 200].

6.1.2 The simplest approximation to the photocurrent

The goal of this chapter is to calculate the experimental spectrum shown in Fig. 6.1 from first principles. In Chapter 3 the concept of the spectral function $A(E)$ was introduced, so that the photocurrent $I(E)$ could be written in terms of $A(E)$ and an intensity prefactor (equation 3.67). In DFT the electrons are non-interacting, so the spectral function reduces to the Kohn-Sham density-of-states (DoS) $g(E)$. Neglecting the intensity prefactor gives the following expression for the photocurrent:

$$I(E) \propto g(E) = \sum_{n \text{ occ.}} \delta(E - \varepsilon_n) \tag{6.1}$$

6.1.3 Valence photoemission spectra in DFT and DFT+U

Figure 6.2 shows the spectra calculated using equation 6.1 with and without a Hubbard U correction. The densities-of-states were calculated for the I2b model of the N3/TiO_2 interface (Chapter 4, Fig. 4.5) where two carboxylic acid groups adsorb in bidentate bridge adsorption modes. The same computational parameters were used to calculate the DoS as for the geometry relaxations in Chapter 4. A value of 7.5 eV was used for the Hubbard U parameter, derived from the GWU calculations of Chapter 5.

Some aspects of the interface model DoS agree with the experimental spectrum, for instance the 6 eV bandwidth of the TiO_2 slab states. However a serious failing of the DFT spectrum is that it predicts a finite DoS at the Fermi level

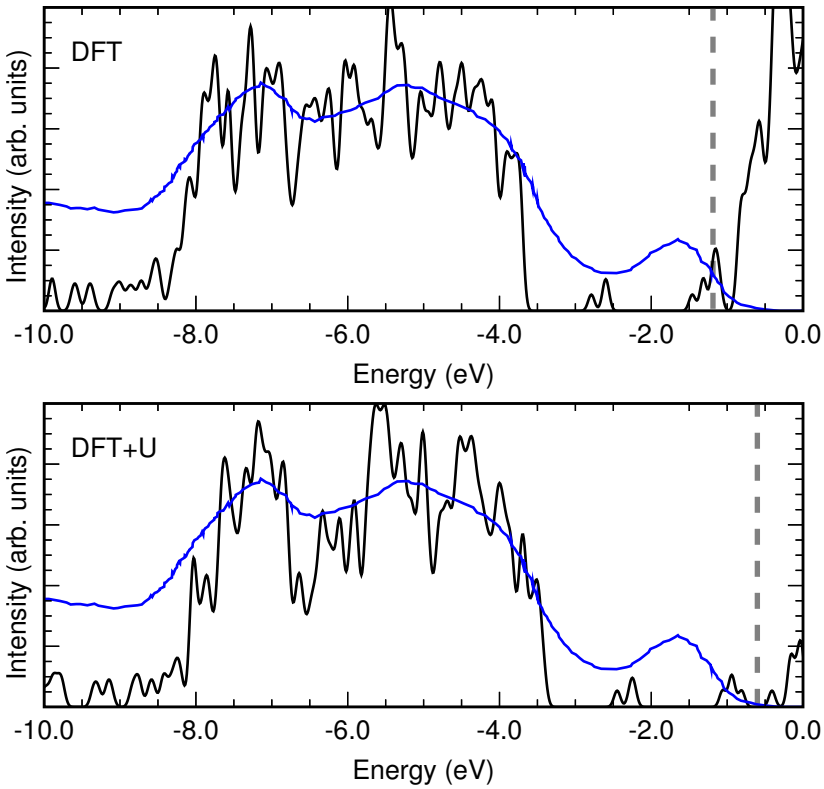

Figure 6.2: The density-of-states (DoS) calculated for the I2b interface model in (top) DFT and (bottom) DFT+U, with U=7.5 eV (black line). Gaussians of width 0.05 eV were convolved onto each KS energy to approximate the δ-function. The experimental photoemission spectrum from Ref. 48 is shown as the blue line. The calculated DoS were shifted to best match the experimental spectrum. The grey dashed line marks the calculated Fermi level, i.e. the boundary between occupied and unoccupied states.

(dashed line in Fig. 6.2), i.e. a metallic interface. Visualising the HOMO of the interface shows a leakage of charge into the conduction band Ti 3d states of the anatase slab. That is, the incorrect description of the Ti 3d states by DFT have led to them lying degenerate with the N3 HOMO, so that they have a very small fractional occupation in the ground state.

This finding is rather significant, as it shows that DFT finds an incorrect ground state density. Including a Hubbard U correction pushes the Ti 3d states up into the conduction band so that they are no longer occupied (lower half of Fig. 6.2), opening a gap of 0.4 eV between the occupied dye orbitals and the conduction band states of the slab. Therefore DFT+U recovers qualitative agreement with experiment. Quantitatively however, the energy separation of the dye HOMO and the highest-energy occupied state on the TiO_2 slab is 2.60 eV in DFT+U, 0.8 eV larger than the largest reported experimental values of the HOMO/VBT offset [48; 197]. Also, the lower-lying dye orbitals appear in the DFT+U spectrum as a new feature at -2.3 eV, at odds with experiment.

Noting that Kohn-Sham eigenvalues do not correspond to excitation energies, the lack of quantitative agreement with experiment is not surprising. In the previous chapter it was shown that TiO_2 and N3 had quasiparticle corrections to their DFT-calculated VBT and HOMO of -0.62 and-1.50 eV respectively. Applying these shifts to DFT+U alignment closes the HOMO/VBT offset to 1.72 eV, which is more reasonable compared to the experiment. However it is necessary to provide a theoretical justification for applying corrections in this manner, and also to account for additional screening of the quasiparticles from the dye/semiconductor interactions. Developing such an alignment scheme is the subject of the next section.

6.2 Theory of PES at molecule/semiconductor interfaces

6.2.1 Practical considerations

In principle, finding the photocurrent exactly requires calculating the frequency-dependent spectral function for a realistic model of the N3/TiO_2 interface. In practice, this approach is totally unfeasible; accurately calculating the spectral function for the two-atom system of bulk silicon is non-trivial [134], let alone for 299-atom models like those in Fig. 4.5. The next level of approximation would be to work in a quasiparticle picture and calculate the quasiparticle energies for the interface models using a perturbative method like GW, but there are still substantial difficulties with such an approach:

- While the GW method is being applied to increasingly more complex systems [118; 201; 202], treating interface models like I1–3 (>1000 Kohn-Sham states) is still out of reach.

- The interface is highly inhomogenous. The quasiparticle properties of semiconductors can be well described in G_0W_0 calculations with plasmon pole models, whereas GW calculations on molecules often involve some self-consistency and a more explicit treatment of the frequency dependence of the dielectric matrix (Chapter 3). It is therefore not obvious what "flavour" of GW would be best applied to interface models which contain both components.

- In fact, since more than half of the atoms in the 240-atom slabs lie at the surface, it is not obvious that even a perfect calculation of the quasiparticle

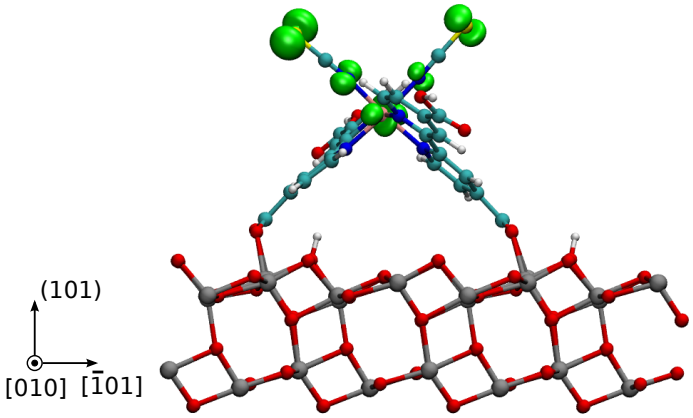

Figure 6.3: Ball-and-stick model and isodensity plot of the highest occupied state of interface model I2b. The green surface corresponds to an isodensity of $|\psi_{\mathrm{H}}(\mathbf{s})|^2$=0.005 states/bohr^3.

properties of the interface models of Fig. 4.5 would correspond to what is measured in experiment. Yet using an even thicker slab would surpass the limit of what is obtainable in standard DFT, let alone more expensive post-DFT methods.

6.2.2 Partitioning the photocurrent

There is thus a need for an alternative method of calculating the photocurrent which is both accurate and computationally efficient. To proceed, the following observations can be noted:

1. Within the energy window of interest, the molecular orbitals do not hybridise with the valence band manifold of the semiconductor. The frontier orbitals of N3, shown in Fig. 5.7 to lie on the NCS ligands and central Ru atom, are spacially separated from the substrate in the interface models of Fig. 4.5. Comparing the isodensity plot of the HOMO of interface model I2b shown in Figure 6.3 with the gas-phase HOMO (Fig. 5.7) confirms that there is no hybridisation of the frontier orbitals with the substrate. Indeed

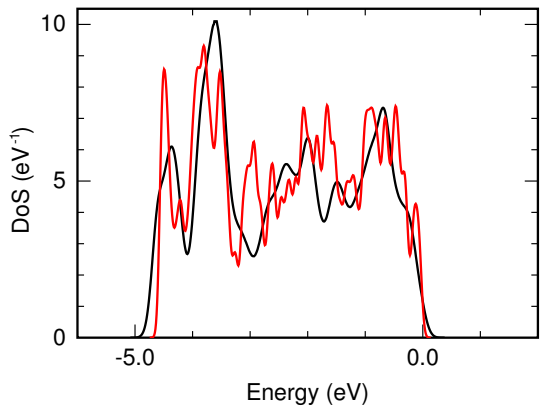

Figure 6.4: The DoS calculated for bulk TiO_2 (black line; c.f. Fig. 5.1) compared to that calculated for a 20 Å-thick anatase (1 0 1) slab (c.f. Sec. 6.4.2). The two spectra were aligned with an arbitrary energy shift.

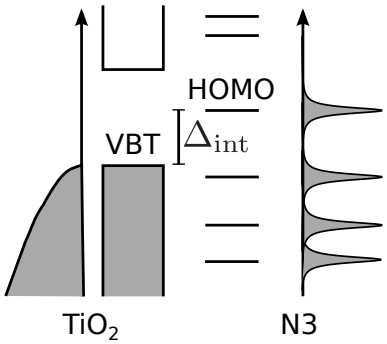

Figure 6.5: Schematic of the alignment process contained in equation 6.2. The bands of the semiconductor and energy-levels of the molecule, which give rise to spectral functions resembling those shown, are aligned through an offset Δ_{int} which is the energy separation of the highest occupied molecular orbital (HOMO) and the valence band top (VBT) of the semiconductor.

the DoS calculated for model I2b in Fig. 6.2 shows two groups of molecular orbitals, separated by 1.3 eV, precisely as seen for the gas phase molecule in Fig. 5.7. Having the HOMO well-separated from the substrate is a design goal of molecular photovoltaic devices since it will reduce recombination losses [203], and is also a characteristic of physisorbed interfaces [204].

2. In the *GWU* calculations in Chapter 5, it was found that states around the valence band edge had the same quasiparticle corrections, while overall the valence bandwidth increased by 0.3–0.4 eV (8%) compared to DFT+U (Fig. 5.5). The quasiparticle renormalisations Z were also found to be very uniform over the TiO_2 valence band, with a standard deviation of 0.01 from the mean Z=0.78. In N3, the four highest-energy orbitals have similar character (Fig. 5.7), so it is reasonable to expect these states to have similar quasiparticle shifts. Therefore a sensible approach is to apply one uniform quasiparticle correction to the states of TiO_2 and another to those of N3.

3. Figure 6.4 compares the DoS calculated for bulk TiO_2 (c.f. Fig. 5.5) with that of a 20 Å-thick anatase (1 0 1) slab. Since the two spectra match each other very well, it is reasonable to neglect the contribution to the photoemission spectrum from the anatase surface and just consider the electronic structure of the bulk.

Observation (1) motivates the partitioning of the spectral function into two separate contributions originating from the dye and the TiO_2, forming the following expression for the photocurrent $I(E)$:

$$I(E) = I_{0,\mathrm{s}} A_{\mathrm{s}}(E) + I_{0,\mathrm{m}} A_{\mathrm{m}}(E + \Delta_{\mathrm{int}}) \tag{6.2}$$

Here 'm' and 's' stand for molecule and substrate. The intensity factors $I_{0,\mathrm{s,m}}$ determine the relative strengths of the two contributions and will be discussed below. The remaining quantities in the expression are the spectral functions $A_{\mathrm{s,m}}$ and the energy offset Δ_{int}. Choosing the energy origins of A_{s} and A_{m} to be the VBT and HOMO respectively, Δ_{int} is precisely the HOMO/VBT offset. Next, observation (2) suggests that it is sufficient to replace the separate spectral functions with their DFT+U densities-of-states. Finally, observation (3) allows $A_{\mathrm{s}}(E)$ to be obtained in a calculation on bulk TiO_2. The partitioning of equation 6.2 is illustrated schematically in Figure 6.5.

6.2.3 Calculating the HOMO/VBT offset

All substrate/molecule interactions and many-body effects are included in the HOMO/VBT offset Δ_{int}, which aligns the two contributions to the photocurrent. The following expression is proposed to calculate Δ_{int}:

$$\Delta_{\mathrm{int}} = E_{\mathrm{m}} - E_{\mathrm{s}} \tag{6.3}$$

where

$$\begin{aligned} E_{\mathrm{m}} &= \varepsilon_{\mathrm{H}}^{\mathrm{KS}} + \Delta\varepsilon_{\mathrm{H}}^{\mathrm{img}} + \Delta\varepsilon_{\mathrm{H}}^{\mathrm{QP}} \\ E_{\mathrm{s}} &= \varepsilon_{\mathrm{V}}^{\mathrm{KS}} + \Delta\varepsilon_{\mathrm{V}}^{\mathrm{slab}} + \Delta\varepsilon_{\mathrm{V}}^{\mathrm{QP}} \end{aligned}$$

Here $\varepsilon_{\mathrm{V}}^{\mathrm{KS}}$ and $\varepsilon_{\mathrm{H}}^{\mathrm{KS}}$ are the standard DFT(+U) KS eigenvalues of the semiconductor and of the molecule, respectively, both obtained from a calculation on an interface model. $\Delta\varepsilon_{\mathrm{V}}^{\mathrm{slab}}$ is a correction to the VBT which removes any spurious quantum confinement effects arising from the thin semiconductor slab [205]. $\Delta\varepsilon_{\mathrm{V}}^{QP}$ is the

GW quasiparticle shift of the semiconductor VBT, as obtained in a bulk calculation, while $\Delta\varepsilon_{\mathrm{H}}^{\mathrm{QP}}$ is the quasiparticle shift of the HOMO of the molecule in the gas phase. $\Delta\varepsilon_{\mathrm{H}}^{\mathrm{img}}$ is the substrate-induced renormalization of the molecular HOMO energy, and arises from the dielectric screening by the semiconductor of the photo-hole in the molecule [201].

Some of the quantities introduced in equation 6.3 have already been obtained. $\varepsilon_{\mathrm{H}}^{\mathrm{KS}} - \varepsilon_{\mathrm{V}}^{\mathrm{KS}}$ is the DFT+U HOMO/VBT offset, which was calculated to be 2.60 eV. $\Delta\varepsilon_{\mathrm{V}}^{QP}$ and $\Delta\varepsilon_{\mathrm{H}}^{\mathrm{QP}}$ were calculated to be -0.62 eV and -1.50 eV in Chapter 5 (Table 5.1 and Section 5.4.2). The "image-charge" and finite slab corrections $\Delta\varepsilon_{\mathrm{H}}^{\mathrm{img}}$ and $\Delta\varepsilon_{\mathrm{V}}^{\mathrm{slab}}$ will now be discussed.

6.3 Image-charge corrections

6.3.1 Classical description

The image-charge correction $\Delta\varepsilon_{\mathrm{H}}^{\mathrm{img}}$ can be understood as follows: when an N3 molecule adsorbed on the TiO_2 surface is ionised in a photoemission experiment, the photo-hole will primarily be screened by the surrounding electrons on the dye. This effect is captured in the gas-phase quasiparticle correction $\Delta\varepsilon_{\mathrm{H}}^{QP}$. However the positively-charged photo-hole will also be screened by the electrons in the substrate. Classically, a point charge placed above a semi-infinite conductor sets up an electric field equivalent to that produced by a mirror image of an opposite charge, hence the label "image-charge".

If one considers an extended charge distribution instead of a point charge, and a semi-infinite dielectric instead of a conductor, the classical electrostatic energy

is [201; 206]:

$$\Delta\varepsilon_{\mathrm{H}}^{\mathrm{class.}} = \int_{z_0}^{\infty} \frac{\rho_H(z)^2 dz}{|z - z_0|} \times \frac{1}{4} \times \frac{1-\epsilon}{1+\epsilon} \tag{6.4}$$

where z_0 is the boundary between the vacuum and the medium whose dielectric constant is ϵ.

6.3.2 ΔSCF and the image-charge effect

In the quantum picture, the image-charge renormalisation is due to the additional contribution to the screened Coulomb interaction (dielectric function) of the interface from the substrate. As such, quasiparticle calculations on entire interface models will capture the image-charge effect. The ΔSCF method also provides a means of calculating the shift. Comparing the KS eigenvalue of the highest occupied state of an interface model to the ΔSCF ionisation potential of that model gives the quasiparticle shift of the interface HOMO $\Delta\varepsilon_{\mathrm{H}}^{\mathrm{nano}}$, from which the image-charge shift $\Delta\varepsilon_{\mathrm{H}}^{\mathrm{img}}$ is obtained as

$$\Delta\varepsilon_{\mathrm{H}}^{\mathrm{img}} = \Delta\varepsilon_{\mathrm{H}}^{\mathrm{nano}} - \Delta\varepsilon_{\mathrm{H}}^{\mathrm{QP}} \tag{6.5}$$

6.3.3 The nanocluster model

One of the limitations of the ΔSCF method is that it is only valid for finite (i.e. non-periodic) systems, while all the interface models considered so far employed extended TiO_2 slabs. However there is a large amount of experience in the literature of using TiO_2 nanoclusters to model anatase substrates [148; 149; 207; 208]. Figure 6.6 shows the ball-and-stick model of a new interface model, based on model I2b but with a stoichiometric anatase nanocluster used instead of a periodic slab.

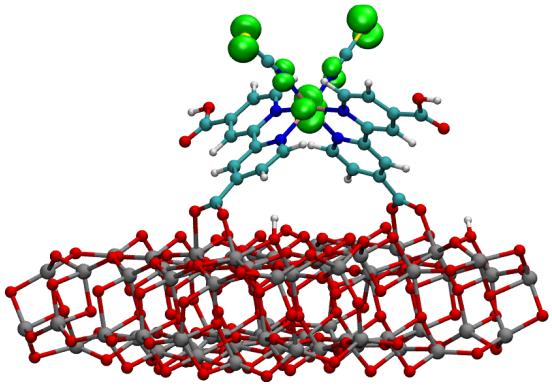

Figure 6.6: Ball-and-stick model and isodensity plot of the spin density calculated in a ΔSCF calculation on an N3 molecule adsorbed on a stoichiometric cluster of anatase TiO_2. The green surface corresponds to a spin density of 0.005 electrons/bohr^3.

The nanocluster consists of 68 TiO_2 units and was constructed in the same way as the (1 0 1) slabs, with additional cuts along the planes with normals along the $[\bar{1}\,0\,1]$ and [0 1 0] directions, such that the cluster dimensions are approximately 18×17×6 Å^3. The relaxed geometries of both the bare nanocluster and the nanocluster with the N3 molecule adsorbed were obtained in a damped Car-Parrinello MD simulations where all the atoms were allowed to move. The computational setup for the structural relaxations was identical to that described in Chapter 4 except for that simulation cells of dimensions 24.3×24.3×26.7 Å^3 and 24.3×24.3×12.2 Å^3 were used to relax the nanocluster with and without the dye, respectively.

When performing ΔSCF calculations, the Coulomb truncation scheme of Ref. 69 was employed. Accordingly it was necessary to increase the size of the simulation cell (c.f. Fig. 2.1) to 52.9×52.9×26.5 Å^3 for the bare nanocluster and to 52.9×52.9×44.5 Å^3 with the dye adsorbed. The ΔSCF calculations on the dye-sensitized nanocluster were the most computationally-demanding of all calculations presented in this entire work, due to the extremely large simulation cell

and large number of KS states.

6.3.4 Electronic structure of the bare nanocluster

The DFT-calculated electronic structure of the nanocluster (no U) finds a gap of 2.26 eV between occupied and unoccupied states. Performing ΔSCF calculations on the bare nanocluster finds an ionisation potential and electron affinity (I.P. and E.A.) of 7.89 and 3.83 eV respectively and hence a quasiparticle gap of 4.06 eV. ΔSCF calculations on much smaller nanoclusters (3–10 TiO_2 units) found a large variation in gaps, from 6.8–4.5 eV [208]. It perhaps is interesting to note that the difference between the KS gap of the nanocluster and bulk anatase is 0.2 eV (Table 5.1). Applying this same shift to the quasiparticle gap of 4.06 eV yields 3.86 eV, which lies at the high end of values found in G_0W_0 calculations on bulk anatase, e.g. 3.83 eV as reported in Ref 180.

6.3.5 ΔSCF ionisation potential of the nanocluster model

Figure 6.6 also shows the isosurface plot of the spin density of the dye/nanocluster model where one electron has been removed. The spin distribution matches the KS HOMO both of the nanocluster model itself and also of interface model I2b (shown in Fig. 6.3), confirming that there is a strong correspondence between the electronic structures of the interface models based on the anatase slab and on the nanocluster. The KS energy of the HOMO of the dye/nanocluster model is -4.94 eV with respect to vacuum, while the ΔSCF I.P. is 6.09 eV. Accordingly the quasiparticle correction to the HOMO of the dye adsorbed on the nanocluster is $\Delta\varepsilon_{\mathrm{H}}^{\mathrm{nano}}$ = -1.15 eV, which by equation 6.5 gives an image charge shift $\Delta\varepsilon_{\mathrm{H}}^{\mathrm{img}}$ = +0.35 eV.

6.3.6 Screening charge

It is interesting to consider the redistribution of charge on the nanocluster when an electron is removed for the N3 molecule. One can define a screening charge density $\delta\rho^{\rm scr}$ as:

$$\delta\rho^{\rm scr}(\mathbf{r}) = [\rho_{+}^{\rm nano}(\mathbf{r}) - \rho_{0}^{\rm nano}(\mathbf{r})] - [\rho_{+}^{\rm m}(\mathbf{r}) - \rho_{0}^{\rm m}(\mathbf{r})] \tag{6.6}$$

Here, $\rho_{+,0}^{\rm nano}(\mathbf{r})$ is the charge density of the dye/nanocluster system with an electron removed or in the charge neutral case. $\rho_{+,0}^{\rm m}(\mathbf{r})$ is the charge density of just the dye molecule, again with and without one electron removed, where the dye molecule is fixed in precisely the same position as it occupies when the nanocluster is present (with H atoms reinstated to replace the Ti–O bonds). Each of the square brackets gives the redistribution of charge on the creation of the photo-hole; taking the difference shows how the substrate affects the screening. A positive value of $\delta^{\rm scr}$ corresponds to electronic charge which is absent when the molecule is in the gas phase.

Figure 6.7 shows an isodensity plot of $\delta\rho^{\rm scr}$ within the TiO_2 nanocluster. Also shown is the planar-averaged $\delta\rho^{\rm scr}$, i.e.

$$\delta\rho^{\rm scr}(z) = \frac{1}{L_x L_y}\int_0^{L_x}\int_0^{L_y}\delta\rho^{\rm scr}(\mathbf{r})dxdy$$

where the integral is taken over the unit cell in the x and y ($[\overline{1}\,0\,1]$ and $[0\,1\,0]$) directions, and z is along the $(1\,0\,1)$ normal. The cumulative integral of $\delta\rho^{\rm scr}(z)$ gives information about charge transfer upon the creation of the photo-hole.

There are two main points to note from Fig. 6.7. The first is that the photo-hole on the dye induces a layer of screening charge on the surface O atoms of the

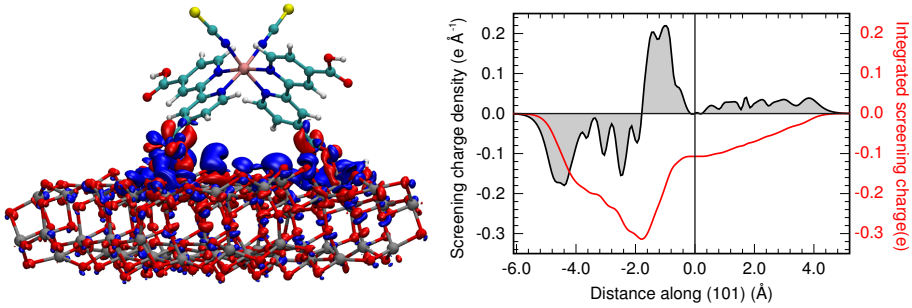

Figure 6.7: Isodensity plot (left) and planar averages (right) of the screening charge density $\delta\rho^{\mathrm{scr}}$ defined in equation 6.6 calculated for the N3/TiO_2 cluster model. The blue and red surfaces in the isodensity plot correspond to $\delta\rho^{\mathrm{scr}}$=±0.002 electrons/bohr^3, respectively, and for clarity the surfaces were truncated above the surface of the semiconductor. The red line in the right plot is the integrated planar-averaged screening charge, i.e. the cumulative integral of the black line. The distance along the (1 0 1) normal is given with respect to the plane intersecting the Ti–O bonds between the dye molecule and nanocluster.

substrate, seen as the large blue areas on the isosurface plot and the peak in the screening charge plot between z = -2.0 and 0.0 Å. The cumulative integral (red line) gives the amount of screening charge localised in this region as 0.20 electrons. This behaviour is in line with the classical interpretation given in Section 6.3.1, that the positive hole is screened by a negative charge density.

The second point is that, at 0.0 Å (which corresponds to the boundary between the nanocluster and dye) the cumulative integrated screening charge is not zero, but rather -0.11 electrons. That is, 0.11 electrons are transferred from the nanocluster to the dye upon creation of the photo-hole. This additional screening is peculiar to covalently-bonded interfaces, where the chemical bonds between the molecule and substrate (here the Ti–O bonds) provide a pathway for charge transfer.

6.3.7 Comparison with the classical model

Given that the previous section found image-charge screening to occur both through long-range electrostatics and direct charge transfer, it seems unrealistic to expect the classical expression (equation 6.4) to provide a quantitative description of the image-charge shift. Evaluating equation 6.4 requires a value for the dielectric constant ϵ and the choice of the height of the virtual image plane z_0.

The experimentally-measured high frequency dielectric constant of anatase is 6.6 [138], while the static dielectric constant is around ∼100; the former is more appropriate, since the static constant includes ionic screening which occurs on longer timescales than photoemission [46]. Taking the HOMO calculated for interface model I2b as the charge distribution (i.e. $\rho_H(\mathbf{r}) = |\psi_{\mathrm{H}}(\mathbf{r})|^2$) and choosing the image plane to lie midway between the Ti–O bonds yields a classical image charge shift of $\Delta\varepsilon_{\mathrm{H}}^{\mathrm{class.}} = 0.34$ eV, in remarkably good agreement with the ΔSCF-calculated value of 0.35 eV. The classical model is thus an attractive alternative to the very expensive ΔSCF calculation of the image charge shift.

6.4 Finite slab correction

6.4.1 Choosing a reference level

The remaining term in equation 6.3 is the correction for using a finite slab $\Delta\varepsilon_{\mathrm{V}}^{\mathrm{slab}}$. This quantity is the difference in energy between the bulk valence band top (as obtained in the calculations of Chapter 5) and the highest-energy occupied state localised on the anatase slab for an N3/TiO_2 interface model like I2b. As such it is necessary to establish a common reference energy level to which the bulk and

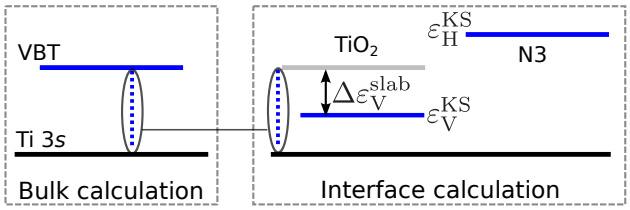

Figure 6.8: Schematic illustration of the concept of aligning the TiO_2 energy levels to the deep-valence Ti 3*s* states. A bulk calculation (left) gives the position of the valence band top (VBT) with respect to the 3*s* band (blue dotted line). Identifying the same 3*s* band in an interface calculation (right) allows the identification of the bulk VBT on the same energy scale (grey line). Also in the interface calculation the VBT of the slab can be identified as the highest-energy KS state which comprises of O 2*p* states on the slab (ε_V^{KS}). The energy difference between the bulk VBT and ε_V^{KS} is precisely the finite slab correction $\Delta\varepsilon_V^{slab}$.

interface calculations can be aligned.

There are different choices available for the reference level. For instance one could average the local electronic potential $V(\mathbf{r})$ in the bulk unit cell and compare it to the planar-averaged local potential in the middle of the slab [205]. However the anatase slab used in the interface models is rather thin, and the presence of the vacuum and dye molecule introduce structural deformations which cause fluctations in the local potential.

A more attractive option is to align to the so-called 'deep-valence' or semicore states [209]. The Ti pseudopotential used in all the calculations above contains 3*s* electrons in the valence. These states are very tightly bound, lying 24 eV below the next highest-energy band (3*p*) and 58 eV lower than the valence band top. As such (like the O 1*s* electrons in Chapter 4) the Ti 3*s* energies depend mainly on their local chemical environment and are less sensitive to large-scale structural deformations. The alignment approach is illustrated schematically in Figure 6.8.

Considering first bulk anatase TiO_2, a DFT+U calculation finds the Ti 3*s* band to be essentially dispersionless, with an average energy of -51.15 eV and a

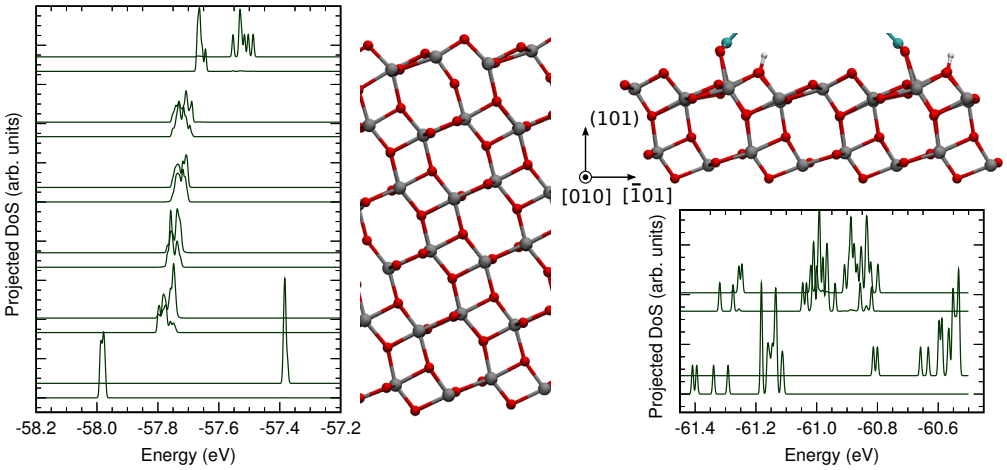

Figure 6.9: Ball-and-stick models and Ti 3*s* projections calculated from equation 6.7 for a clean 12-layer slab (left) and for interface model I2b (right).

standard deviation of 0.01 eV. The top of the valence band at the X point is at 6.98 eV in the same calculation, so the separation between the 3*s* level and VBT (blue dotted line in Fig. 6.8) is 58.13 eV.

6.4.2 The 12-layer anatase slab

To determine $\Delta\varepsilon_{\mathrm{V}}^{\mathrm{slab}}$ it is necessary to find the same 3*s* reference level in the interface calculation. First it is useful to consider a thick, clean anatase slab, illustrated in Figure 6.9. The slab has a hexagonal surface cell of area 138 Å and consists of 12 TiO_2 layers (20 Å thick), with a vacuum region of 20 Å between periodic slabs. The bottom three atomic layers were fixed in their bulklike positions. After relaxing this slab (so that the force on each atom was below 0.07 eV/Å) the KS eigenvalues were calculated in a DFT+U calculation at the Γ point.

Like in the bulk case the Ti 3*s* band is clearly identifiable in the slab calculation as the lowest-energy KS states. However, although most of the values are clustered around -57.74 eV, there are some outliers at -58.0 and -57.4 eV.

Understanding the origin of these shifts is possible by projecting each KS state onto the layer-resolved Ti 3s pseudo-atomic orbitals, i.e. compute

$$g^{3s}(z_i, E) = \sum_n \sum_{I_i} \langle \phi_{I_i 3s} | \psi_n \rangle \delta(E - \varepsilon_n) \tag{6.7}$$

where the sum is taken over all KS states and energies ψ_n and ε_n and over all the pseudo-atomic orbitals $\phi_{I_i 3s}$ which belong to Ti atoms located in layer i [whose height with respect to the (1 0 1) surface is z_i]. This layer-resolved PDoS is shown in Fig. 6.9; each of the 12 lines corresponds to a different Ti layer.

From Fig. 6.9 it can be seen that the outliers in the $3s$ energies originate from the two lowest planes of Ti atoms, which are either bonded to underco-ordinated O atoms or are themselves underco-ordinated. The top two layers show deviations for the same reason, although the effect is smaller since these atoms are allowed to relax and compensate the missing charge (c.f. autocompensation, introduced in Section 4.1.3). The remaining eight layers show very little variation as a function of layer height from an average value of -57.74 eV (0.02 eV standard deviation). Equating this value with the 3s level determined in the bulk calculation finds the bulk VBT to be at 0.39 eV on this scale. Meanwhile the highest occupied state in the slab calculation (i.e. $\varepsilon_{\mathrm{V}}^{\mathrm{KS}}$) is 0.18 eV, which gives a value of $\Delta\varepsilon_{\mathrm{V}}^{\mathrm{slab}}$=+0.21 eV for the 12-layer slab.

6.4.3 The slab correction for interface models

While the behaviour of the 12-layer slab is a useful guide, all the interface models involving the N3 molecule used a four layer slab, which presumably will have different confinement effects. As such $\Delta\varepsilon_{\mathrm{V}}^{\mathrm{slab}}$ must be recalculated for the interface models.

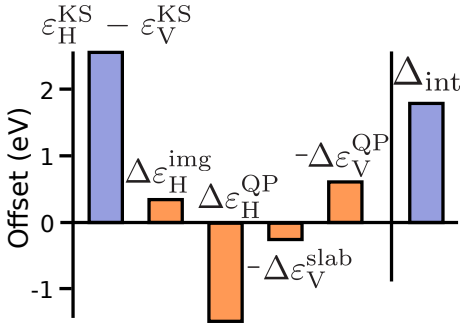

Figure 6.10: Bar chart showing the different contributions to the HOMO/VBT offset Δ_{int}, as calculated for interface model I2b. The total offset is obtained by adding all the bars together.

Fig. 6.9 shows the layer-resolved PDoS calculated with equation 6.7 for the I2b interface model. The data exhibits far more noise in this case, since a larger proportion of the atoms are affected by the vacuum and adsorbate. Nonetheless the 3*s* levels of the interface model show the same underlying behaviour as found for the 12-layer slab. The two lowest layers exhibit peaks separated by ∼0.6 eV, and the highest layers also exhibit two strong features, separated by ∼0.2 eV.

Computing the projections for all the interface models I1–I3 finds the bottom two Ti layers to always show the same two-peak structure. Therefore these two peaks can be used to align the interface model energies to the 12-layer slab, which in turn can be aligned to bulk. For I2b, the two peaks are at -61.14 and-60.54 eV. In the 12-layer slab the corresponding peaks are at -57.98 and-57.38 eV, suggesting that all energies in I2b are shifted down by 3.16 eV in comparison. Accordingly the bulk Ti 3*s* level is at -60.90 eV, and the bulk VBT therefore at -2.77 eV. Comparing to the value of $\varepsilon_{\mathrm{V}}^{\mathrm{KS}}$=-3.02 eV found for I2b gives $\Delta\varepsilon_{\mathrm{V}}^{\mathrm{slab}}$=+0.25 eV.

6.5 Δ_{int} for I2b

Figure 6.10 collates all of the corrections obtained for interface model I2b. The total offset Δ_{int} is found as

$$\begin{aligned}\Delta_{\mathrm{int}} &= (\varepsilon_{\mathrm{H}}^{\mathrm{KS}} - \varepsilon_{\mathrm{V}}^{\mathrm{KS}}) + \Delta\varepsilon_{\mathrm{H}}^{\mathrm{img}} + \Delta\varepsilon_{\mathrm{H}}^{\mathrm{QP}} - \Delta\varepsilon_{\mathrm{V}}^{\mathrm{slab}} - \Delta\varepsilon_{\mathrm{V}}^{\mathrm{QP}} \\ &= (2.60 + 0.35 - 1.50 - 0.25 + 0.62)\ \mathrm{eV} \\ &= 1.82\ \mathrm{eV}\end{aligned}$$

that is, the quasiparticle, image charge and finite slab corrections reduce the DFT+U HOMO/VBT offset of 2.60 eV by 0.78 eV.

Since the image charge and finite slab corrections have the same sign and similar magnitude, there is a cancellation of errors in standard DFT. The main origin of the 0.78 eV correction to the DFT+U alignment is the asymmetric quasiparticle corrections of the dye and the semiconductor; since $|\Delta\varepsilon_{\mathrm{H}}^{\mathrm{QP}}| > |\Delta\varepsilon_{\mathrm{V}}^{\mathrm{QP}}|$, the overall effect is to reduce Δ_{int}.

Returning to equation 6.2 for the photocurrent, there remain two questions. First, the densities-of-states are technically sums of δ-functions, but in real experiments there will be broadening of the peaks. The broadening mechanisms are investigated in the next section. Second, the relative intensity of the contributions from the dye and semiconductor has not yet been determined, and is the subject of the final section.

6.6 Broadening of the photoemission spectrum

There are several mechanisms which may account for broadening in a photoemission spectrum. First, the absorption of a photon and emission of an electron

leaves the system in an excited state, which has a finite lifetime and therefore results in a spread of energies; however this source of broadening vanishes at the frontier orbitals (since there are no lower-energy states for the system to decay into). Another source of broadening is the thermal motion of the ions, which may shift the quasiparticle energies. Furthermore if the N3 molecules on the TiO_2 surface are adsorbed in a number of different modes with different HOMO/VBT offsets, there will be broadening due to this configurational disorder.

6.6.1 Thermal motion

All of the calculations described so far were performed with the ions frozen in their equilibrium positions, and therefore neglect ionic motion. The experiments of Ref. 48 were performed at room temperature, so classically one expects the ions to have a statistical distribution of kinetic energies. As the ions' positions evolve, so does the potential experienced by the electrons, and therefore the electronic eigenvalues may display a time dependence.

Actually, given that the ions also obey the laws of quantum mechanics, the picture of pointlike ions frozen in space is not valid even at zero temperature. To properly incorporate this zero-point motion it would be necessary to consider the joint electron-nuclear wavefunction, which is the subject of ongoing research [185; 186; 210]. However here the assumption is made that the zero-point effects are weak enough to be neglected at room temperature.

In order to estimate the thermal broadening, a finite-temperature Car-Parrinello molecular dynamics (MD) simulation was performed on the dye/nanocluster interface shown in Fig. 6.6. The temperature was controlled with a Nosè-Hoover thermostat [79; 80] set at 300 K with a frequency of 20 THz. The simulation consisted of a 3 ps equilibration stage followed by 6 ps of data collection. The

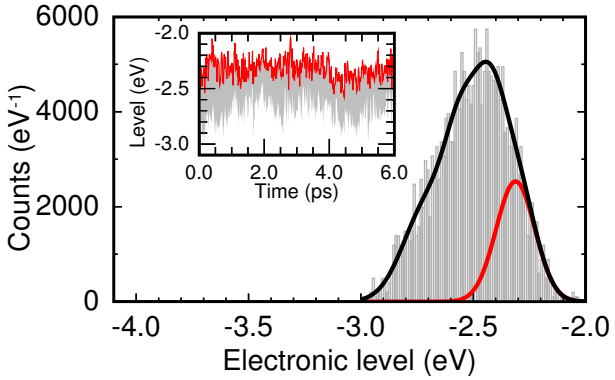

Figure 6.11: Distribution of the four highest electronic eigenvalues obtained in the 6 ps MD simulation of the N3 dye on the TiO_2 nanocluster. The eigenvalues were sampled at 0.01 ps intervals and sorted into 0.01 eV bins, and the resulting histogram is shown as the grey lines. The black line is a fit to the data based on the sum of four gaussians; the highest-energy gaussian is shown as the red line. The inset shows the same data in the time domain, with the highest-energy eigenvalue shown in red.

MD timestep was 2×10^{-4} ps and the electronic eigenvalues were sampled every 50 steps (0.01 ps). The same simulation cell was used as for the initial relaxation of the nanocluster, and no truncation scheme was employed.

It should be noted that the Car-Parrinello eigenvalues, which are the quantities sampled here, only coincide with the KS energies when the electric degrees of freedom are at equilibrium [66]. To check the difference, five geometries were selected from the MD trajectory and their KS eigenvalues computed in a fixed point calculation. The KS eigenvalues tracked the behaviour of the MD eigenvalues, and the deviation between the two was 0.05 eV in the worst case. As such the fact that the MD eigenvalues include a contribution from the fictitious electron dynamics is ignored in the following.

Figure 6.11 is a histogram of the four highest MD eigenvalues obtained in the 6 ps run, corresponding to the HOMO–HOMO-3 of the adsorbed dye. The inset shows the time evolution of these eigenvalues. The black line in Fig. 6.11 is a fit

of the histogram data based on the sum of four gaussians, one of which is shown as a red line (FWHM of 0.18 eV).

It is clear that the thermal broadening of these four states, which lie within 0.3 eV of each other in the gas phase at equilibrium (c.f. Fig. 5.7), causes them merge into a single peak. Therefore the feature that is generally assigned in experiments as the HOMO is in reality a composite peak of four states. The centre of this peak is redshifted by 0.19 eV with respect to the 'actual' HOMO (centre of the red gaussian).

Taking the 0.18 eV width of the fitted red line as an order-of-magnitude estimate, thermal broadening can be included in the calculated photoemission spectrum by replacing the δ-functions in the DoS with gaussian curves of this width.

6.6.2 Configurational disorder

Of the quantities shown in Fig. 6.10 which make up Δ_{int}, $(\varepsilon_{\text{H}}^{\text{KS}} - \varepsilon_{\text{V}}^{\text{KS}})$, $\Delta\varepsilon_{\text{H}}^{\text{img}}$ and $\Delta\varepsilon_{\text{V}}^{\text{slab}}$ depend on the adsorption geometry of the dye molecule. To quantify the effect of adsorption geometries, these quantities were calculated for the six isolated dye interface models I1–I3. $(\varepsilon_{\text{H}}^{\text{KS}} - \varepsilon_{\text{V}}^{\text{KS}})$ and $\Delta\varepsilon_{\text{V}}^{\text{slab}}$ can be obtained in a single DFT+U calculation on the interface model. Computing $\Delta\varepsilon_{\text{H}}^{\text{img}}$ explicitly would require five very expensive ΔSCF calculations on new models based on TiO_2 nanoclusters. However noting the good agreement of the classical image-charge expression with the explicit calculation, equation 6.4 can be used to estimate $\Delta\varepsilon_{\text{H}}^{\text{img}}$ instead.

Figure 6.12 shows the values of Δ_{int} calculated for the six models. There is a substantial 0.70 eV variation in the HOMO/VBT offset across adsorption models; assessing the different contributions to Δ_{int} in Table 6.1 attributes this

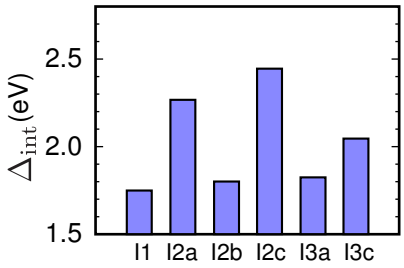

Figure 6.12: HOMO/VBT offset Δ_{int} calculated for interface models I1–I3 (c.f. Table 6.1, Fig. 4.5).

Model	I1	I2a	I2b	I2c	I3a	I3b
$\varepsilon_{\mathrm{H}}^{\mathrm{KS}} - \varepsilon_{\mathrm{V}}^{\mathrm{KS}} - \Delta\varepsilon_{\mathrm{V}}^{\mathrm{slab}}$	2.33	2.82	2.35	2.99	2.34	2.57
$\Delta\varepsilon_{\mathrm{H}}^{\mathrm{img}}$	0.31	0.34	0.35	0.35	0.38	0.37
Δ_{int}	1.76	2.28	1.82	2.46	1.84	2.06

Table 6.1: Contributions to Δ_{int} as calculated for the six interface models I1–3. The image charge corrections were calculated with equation 6.4 except for I2b (0.01 eV difference in this case). All values are given in eV.

variation to changes in the KS offset $\varepsilon_{\mathrm{H}}^{\mathrm{KS}} - \varepsilon_{\mathrm{V}}^{\mathrm{KS}}$. One interesting result is the large variation in the I2 models. For instance, adsorbing via two bidentate bridges on the same bipyridine (I2a) causes a 0.46 eV upshift of the HOMO compared to I2b, where the bridges are on different bipyridines. A hybrid functional study on the N719 molecule had previously found the same trend [148]. Yet exchanging a bidentante bridge for a monodentate ester-type bond (I2c) shifts the HOMO further up still, by 0.18 eV w.r.t. I2a.

6.7 Relative intensities

The final ingredient in equation 6.2 is the relative intensity of the dye and semiconductor contributions to the spectrum, $\frac{I_{0,\mathrm{s}}}{I_{0,\mathrm{m}}}$. In replacing the spectral function with a DoS, it was assumed that matrix element effects, that is, the coupling between initial and final states mediated by an interaction which appears in Fermi's golden

rule, can be neglected. Actually this is a sensible approximation for this system: for high-energy (X-ray) incident photons, the magnitude of the matrix element is largely determined by the symmetry of the underlying atomic orbitals [46], and for organic and metal-organic sensitizers on metal-oxide surfaces, both the HOMO and VBT have significant p character [211]. Factors that determine the intensity other than the matrix elements are (i) losses due to the photoelectron being scattered before escaping the oxide, or being reflected at the interface with the vacuum (transport/transmission losses) and (ii) the areal density of the dye molecules.

A sophisticated treatment of point (i) (and also matrix element effects) is a considerable challenge and the subject of current research [212; 213]. A simpler approach is to invoke the phenomenological electron escape model first introduced for the O 1s spectra of Chapter 4. The anatase (1 0 1) slab can be divided into layers coplanar to the surface. The spacing between layers is 3.6 Å, and each layer contributes 60.9 states/nm^2 to the valence band. The dye HOMO is assigned an "average height" z_D=9.32 Å, obtained as the mean displacement along the normal to the (1 0 1) plane for the four highest occupied states, with the highest TiO_2 layer taken as the origin of z. Each dye molecule contributes 109 states. Then, in the phenomenological model of electron escape depth λ, assuming an areal dye density of σ the relative intensity satisfies

$$\frac{I_{0,\mathrm{s}}}{I_{0,\mathrm{m}}} = \frac{60.9\ \mathrm{nm}^{-2}}{109\sigma} \times \frac{e^{\frac{-z_D}{\lambda}}}{(1 - e^{\frac{-0.36\mathrm{nm}}{\lambda}})} \tag{6.8}$$

Equation 6.8 is obtained by weighting the contribution of each layer by $\exp(-z/\lambda)$ and summing the TiO_2 layers to infinity, given that the valence band and DoS

of the isolated N3 molecule are normalised to unity. For monolayer coverage a reasonable value of σ is 0.5 molecules/nm^2, while a value if 5 Å for λ is appropriate for electrons with kinetic energies of ∼450 eV [48; 169]. With these values, $\frac{I_{0,\mathrm{s}}}{I_{0,\mathrm{m}}} = 0.34$.

6.8 The quasiparticle spectrum

6.8.1 Computational details

Finally having considered all the terms in equations 6.2 and 6.3, it is possible to present the quasiparticle spectrum calculated for the N3/TiO_2 interface. To incorporate configurational disorder into the final photoemission spectrum, the total photocurrent is written as a sum of contributions from the six interface models, each with its associated Δ_{int} given in Table 6.1. This procedure can be thought of as providing a maximum broadening attributable to configurational disorder. The TiO_2 DoS was aligned to best match the experimental photoemission spectrum, with Δ_{int} fixing the alignment of the dye's contribution. Similarly $I_{0,\mathrm{s}}$ was set to match the experimental intensity.

6.8.2 Comparison with experiment

Figure 6.13 shows the quasiparticle spectrum calculated with equation 6.2 as the light blue shaded area, compared to the experimental spectrum of Ref. 48, shown as the dark blue line. The calculated spectrum shows a marked improvement compared to the DFT and DFT+U calculations of Fig. 6.2. In particular, the "HOMO" feature (which is actually HOMO–HOMO-3) now coincides with experiment. The structure seen in this calculated peak arises from the configurational

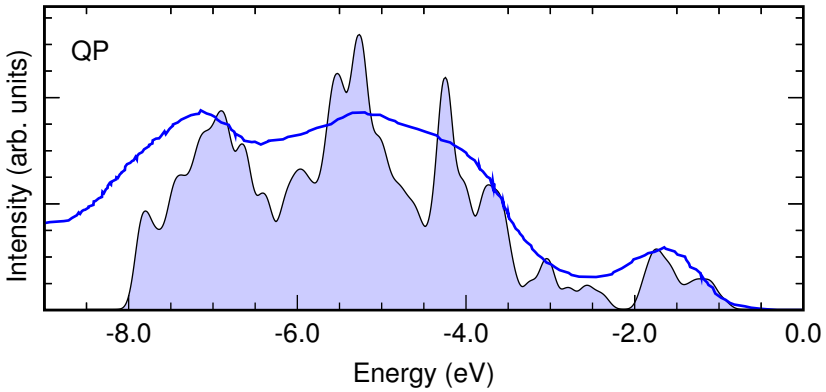

Figure 6.13: Valence photoemission spectrum of the N3/TiO_2 interface, calculated with equation 6.2 (light blue shaded area) compared to the experimental spectrum of Ref. 48 (blue line). The energy axis is given with respect to the Fermi level of the experimental sample.

disorder; models I1, I2b and I3a all have similar Δ_{int} so they contribute to a large peak, with the other configurations contributing to a shoulder at lower binding energy.

It is interesting to note the presence of the lower lying dye-orbitals at -3.0 eV, which are Ru 4*d* orbitals. The calculated energies of these states should be treated with some caution, as the use of the common quasiparticle correction for these orbitals and the HOMO states is not well-justified. However it does appear likely that the experimental spectrum contains contributions from these orbitals at energies around the valence band onset.

In terms of the broadening, the calculations underestimate the width of the features compared to experiment, indicating that additional factors— possibly the quantum motion of the ions—play an equally important role. However the calculated relative intensity agrees remarkably well with experiment.

6.9 Conclusions

This chapter has focused on calculating the photoemission spectrum of the interface formed between the N3 molecule and anatase TiO_2. First, it was shown that just taking the DoS calculated for an interface model in DFT or DFT+U did not produce a spectrum in agreement with experiment. In fact, the DFT spectrum exhibited a finite DoS at the Fermi level, due to the HOMO lying degenerate in energy with the TiO_2 conduction band. However it was noted that applying the quasiparticle corrections calculated in the previous chapter to the DFT+U spectrum improved the agreement with experiment.

This observation was developed into an expression for the photocurrent, equation 6.2, where the spectrum was decomposed into separate contributions from the dye and semiconductor aligned by an offset Δ_{int}. Δ_{int} was expressed in terms of a number of quantities: the DFT+U alignment, calculated for an interface model; quasiparticle corrections, calculated for the dye and semiconductor in isolation; an image-charge shift, which took into account additional screening of the excited dye by the substrate; and a correction for the finite slab used in the interface models.

Each of these terms was discussed and calculated. The image-charge shift was computed for a dye adsorbed on a TiO_2 nanocluster using the ΔSCF method, where it was found that both long-range electrostatics and direct charge transfer contributed to screening the photo-hole. However a classical expression for the image-charge shift performed rather well. The correction for the finite slab was determined by aligning slab and bulk calculations to a common Ti 3s reference level.

Two broadening mechanisms were also considered. Temperature effects were

quantified assuming that the ions' motion could be treated classically with a Car-Parrinello molecular dynamics simulation. The energies of the top four dye states were sufficiently blurred by the ionic motion that they were no longer resolvable at 300 K. Configurational disorder was also investigated by considering the HOMO/VBT alignment for six different interfaces. There it was found that different geometries could yield variations up to 0.7 eV. Finally a simple escape depth model was used to estimate the relative intensities of the dye and semiconductor contributions to the photoemission spectrum.

The work presented in this chapter is the first calculation of a photoemission spectrum from first principles of such a complex interface. Carefully accounting for the above factors corrected the deficiencies of the DFT and DFT+U spectra and showed that quantitative agreement with experiment can be obtained. The work has also opened doors to new investigations: (i) For the purposes of device optimisation it would be desirable to further investigate the atomistic origin of shifts in HOMO/VBT alignment shown in Fig. 6.12. (ii) Since the classical temperature simulation apparently underestimates the broadening, it would be interesting to evaluate the zero-point renormalisation of the quasiparticle energies at the interface. (iii) The charge-transfer screening of covalently-bonded molecules is an interesting phenomenon which deserves further investigation. (iv) Going beyond scissor shifts, i.e. using full quasiparticle DoS instead of the DFT DoS for the molecule and semiconductor, would further elucidate the contribution to the spectrum of the low-lying Ru 4d states.

Chapter 7

Core-level shifts beyond N3/TiO_2

In Chapter 4 I presented calculations of O 1*s spectra of interface models where the analysis focused solely on the two peaks originating from the adsorbed species. The third peak, arising from the O atoms of the* TiO_2 *substrate, was not included because the* TiO_2 *slab used in the interface model was not sufficiently thick. In this chapter I return to this substrate peak. First I examine the fine structure of the O* 1*s spectrum of the anatase* (1 0 1) *slab. Then I propose an alignment scheme which allows the substrate peak to be included in O* 1*s spectra. The scheme is demonstrated for the interfaces between anatase* (1 0 1) *and two molecular monolayers:* H_2O *and bi-isonicotinic acid.*

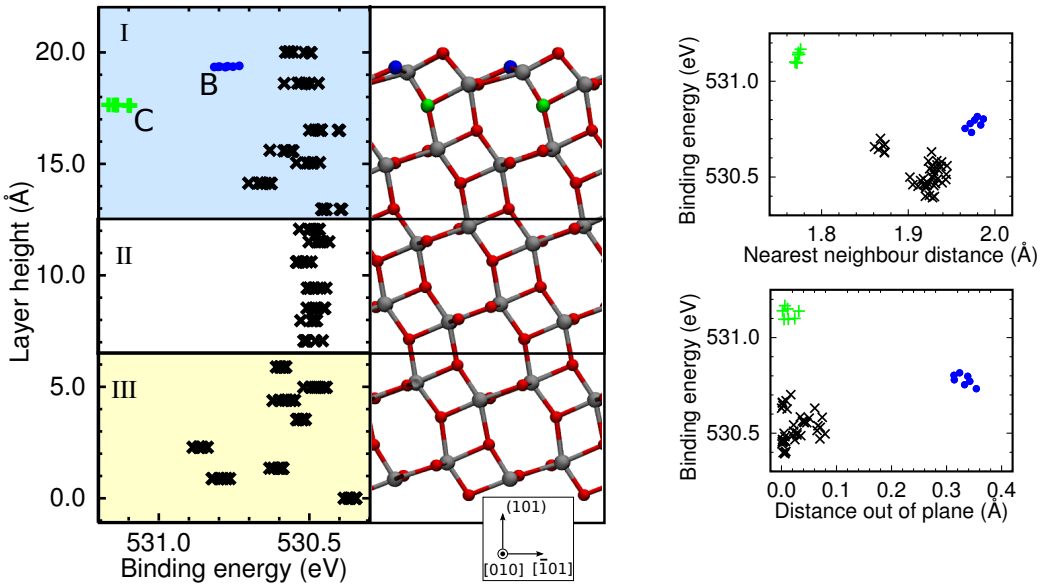

Figure 7.1: (a) O 1*s* binding energies calculated for the 20 Å-thick anatase TiO_2 slab as a function of height of the O atoms. A ball-and-stick representation of the slab, scaled so that its dimensions along the normal to the (1 0 1) plane matches the scale of the plot, is also shown. The coloured atoms labelled 'B' and 'C' display unusual binding energies due to geometrical distortions, discussed in the text. (b) Correlation of O 1*s* binding energies of the atoms in Region I with bond length to their nearest Ti neighbour (top) or the deviation from the ideal (1 0 0) or (0 1 0) geometry (bottom) as explained in the text. The twofold co-ordinated O atoms are not included.

7.1 The clean anatase (101) slab

In Chapter 6, a thick (20 Å) anatase slab was introduced as a means of aligning the energy levels of interface models to the band edges of bulk TiO_2 via the Ti 3*s* semicore states. The O 1*s* binding energies can be calculated for exactly the same slab, using the ΔSCF method introduced in Chapter 2. The same simulation cell, pseudopotentials and plane wave cutoffs were used as for the Ti 3*s* alignment in Chapter 6.

7.1.1 O 1s binding energies

Figure 7.1(a) shows the O 1s binding energy calculated for each O atom in the anatase slab. The energies are offset according to the height of the layer to which the O atom belongs. A ball-and-stick representation of the slab is also shown on the same scale.

The slab has been divided into three regions, labelled in Fig. 7.1(a) as I, II and III. Region III contains the unphysical lower surface of the slab; the bottom three layers are fixed in their bulklike positions, but the lowest O and Ti layers are not fully co-ordinated. The O 1s energies in this region are thus discarded. Region II is the middle of the slab, and it can be seen that the O 1s energies display very small variation with respect to their average value (standard deviation 0.03 eV). The arbitrary constant which sets the absolute value of the binding energy was chosen so that the average 1s energy of the O atoms in Region II was 530.5 eV.

In Region I, the effects of the relaxation of the surface on the O 1s energies are evident. The two plots in Fig. 7.1(b) show the correlation between geometrical parameters and calculated binding energies in Region I. The first considers the distance between each O atom and its nearest Ti neighbour. When the (1 0 1) surface is formed, the fivefold co-ordinated Ti atoms relax into the substrate, contracting one of the Ti–O bonds by 0.1 Å. The 1s energies of these O atoms, labelled 'C' and coloured green in the figure, are shifted by 0.5 eV to higher binding energy.

Generally all the O atoms follow a linear correlation between bond length and 1s shift, except for the atoms labelled 'B' and coloured blue. These atoms are also bonded to the fivefold co-ordinated Ti atoms, and when the latter relax into the substrate, the bonds to 'B' atoms are distorted. This distortion can be quantified by noting that in the ideal structure, each O atom lies coplanar with

its three Ti neighbours, either in the (1 0 0) or (0 1 0) plane. The distance out of this ideal plane is shown in the lower plot of Fig. 7.1(b), where it is clear that there is a 0.3 Å displacement out of the (1 0 0) plane for Ti and 'B' atoms. The distortion results in an increase the 1s binding energy, albeit by a smaller amount than for 'C'.

7.1.2 The infinite slab

In Region II, the O 1s binding energies are effectively independent of layer height. It is reasonable therefore to suppose that adding further layers of Ti and O atoms to the anatase slab would increase the size of Region II compared to I and III, but not produce any new information. Accordingly one can construct the spectrum of a semi-infinite slab by combining the explicit calculations of Region I with layers of "ghost atoms". The ghost atoms all have the same O 1s binding energy E_{bulk} which is that calculated for Region II, and their positions are determined by the crystal structure of anatase. Then the simple escape depth model first used in Chapter 4 is employed, weighting the contribution of each real and ghost atom by the prefactor $\exp(z_i/\lambda)$, where λ is the electron escape depth. The mathematical expression for the procedure is:

$$I(E) \propto \sum_{z_i > z_{\mathrm{bulk}}} \exp(z_i/\lambda) \times \delta(E - E_i) + w_{\mathrm{bulk}}(\lambda) \times \delta(E - E_{\mathrm{bulk}}) \qquad (7.1)$$

The first term is a sum over the O 1s binding energies E_i calculated for each atom whose displacement in the normal to the (1 0 1) plane z_i is greater than some cutoff value z_{bulk}. z_{bulk} marks the start of the bulk region, where all O atoms are assumed to have a constant O 1s binding energy E_{bulk}. The intensity weight of the bulk-like contribution w_{bulk} is determined by summing over an

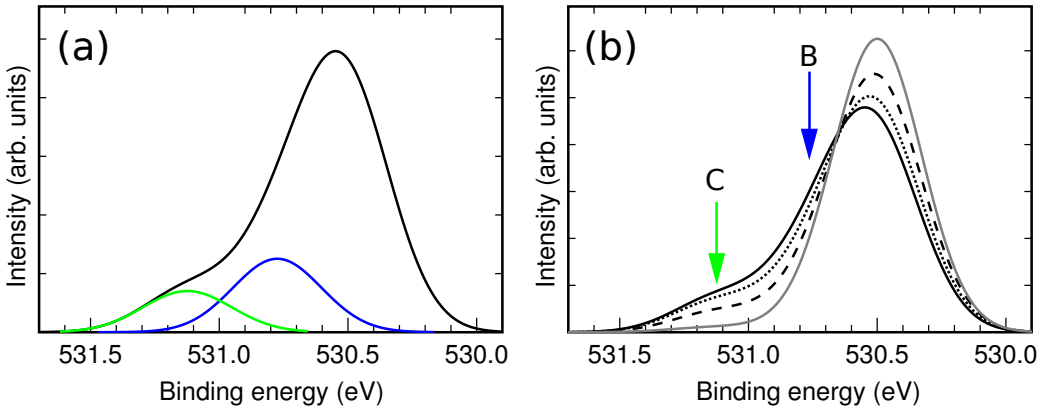

Figure 7.2: O 1*s* spectra calculated for the clean anatase (1 0 1) slab using equation 7.1. In (a) the electron escape depth λ is set to 3 Å. The contributions to the spectrum from the groups of atoms 'B' and 'C' are shown as blue and green lines, respectively. In (b) λ is varied between 3 Å (black solid line), 5 Å (dotted), 10 Å (dashed) and 50 Å (grey solid line). The blue and green arrows correspond to the centres of the contributions of 'B' and 'C' shown in (a).

infinite number of ghost O layers:

$$w_{\mathrm{bulk}}(\lambda) = N \times \frac{\exp(z_{\mathrm{bulk}}/\lambda)}{1-\exp(-3.53\text{Å}/\lambda)} \times \Big(1+\exp(-0.91\text{Å}/\lambda) + \exp(-1.49\text{Å}/\lambda) + \exp(-2.35\text{Å}/\lambda)\Big) \quad (7.2)$$

There are four distinct layers in the bulk cell periodically repeated along a distance of 3.35 Å. N is the number of O atoms per layer in the anatase slab; in this case, N=7.

Figure 7.2 shows the O 1*s* spectra of the clean anatase (1 0 1) surface calculated using equation 7.1 for different values of the escape depth λ. The δ-functions are replaced with gaussians of width 0.4 eV. In Fig. 7.2(a) λ is set to 3 Å. The black line is the total spectrum, while the two underlying curves show the contributions to the spectrum from the groups of atoms 'B' (blue) and 'C' (green). These atoms are responsible for a shoulder at high binding energy. The other atoms in Region I shift the main peak slightly to a higher energy than its bulk

value of 530.5 eV. In Fig. 7.2(b) λ is varied between 3, 5, 10 and 50 Å. As the escape depth increases (corresponding to higher-energy incident photons) more spectral weight gets shifted to the bulk peak.

The 0.4 eV width is rather small when compared to the experimental XPS spectra presented below and in Chapter 4. Consequently it is questionable whether the shoulder due to groups 'B' and 'C' could be observed experimentally. However a careful study of the evolution of the spectrum with λ (incident photon energy) may reveal the small shift in the peak. The practical difficulty with such an approach is that the experimental spectra themselves are calibrated to a reference peak, e.g. the Ti $2p$, which may itself be subject to variations with photon energy.

7.2 Obtaining the bulk peak in the presence of adsorbates

Equation 7.1 was introduced for a clean TiO_2 slab, but it could equally well be applied to interface models by including the adsorbate O atoms in the first sum. The difficulty is that using the 20-Å thick slab for every new interface model greatly increases the computational expense of relaxing the geometry and calculating core binding energies. An attractive alternative approach would be to consider two different systems—the thick, clean slab and a thin slab with molecules adsorbed—and combine the calculated $1s$ binding energies as a post-processing step. Then, only one set of calculations need be performed on the large slab, while all geometry relaxations for adsorbed molecules are performed on smaller systems. The viability of this approach relies on there being a suitable reference common to all systems which can be used to align binding energies calculated

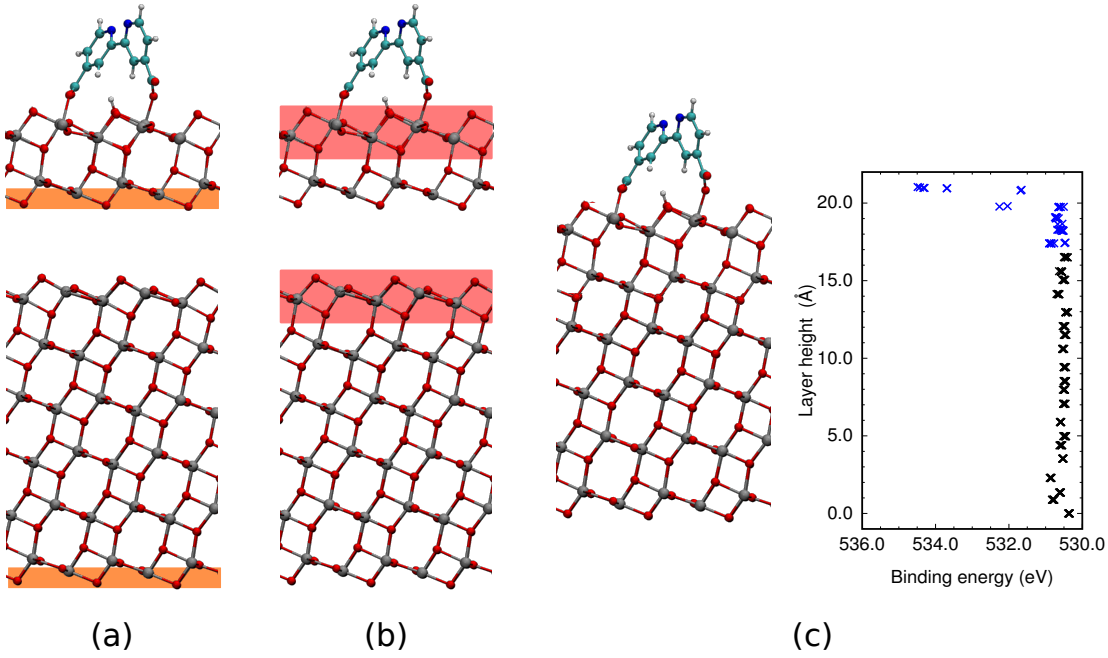

Figure 7.3: Schematic of the procedure used to align the O 1*s* energies calculated for a thin slab with adsorbates (top) and the thick clean slab (bottom). The alignment proceeds as follows: (a) A constant energy shift is applied to the thin slab model so that the 1*s* energies of the bottom two O layers (highlighted) coincide with the thick slab. (b) A constant shift is also applied to the z values [i.e. displacement along the (1 0 1) normal] of each O atom in the thin slab model, so that the highest four O layers (highlighted in red) coincide with the thick slab. Then the highlighted atoms of the thick slab and non-highlighted atoms of the thin slab are discarded. (c) The remaining core-level binding energies are merged together to make a single set, demonstrated pictorially with the ball-and-stick model and with an actual dataset. The blue crosses were obtained from calculations on a thin slab with adsorbed molecules.

for different simulation cells. The bottom three layers of the slab models, always fixed to their bulk geometry, provide this reference (c.f. Chapter 6).

This alignment approach is illustrated in Figure 7.3, and proceeds in steps. The O 1*s* binding energies are calculated for two systems: one based on the thin slab (top) and the other with the thick, clean slab (bottom). The calculations are not aligned either in energy or along the (1 0 1) (i.e. z) direction. Then, all the binding energies of the thin-slab model are shifted by a constant such that the

binding energies of the lowest two O layers now coincide with those of the thick slab [highlighted in Fig. 7.3(a)]. Similarly all the z values of the thin-slab model are shifted so that the highest four O layers of both slabs overlap [Fig. 7.3(b)]. Then the highest and lowest four O layers of the thick and thin slab models respectively are deleted, and the datasets merged together [Fig. 7.3(c)]. The result of the procedure is a single set of data which contains both the adsorbate shifts and a well-defined bulk region. These shifts can then be fed into equation 7.1, producing a spectrum which includes both the contribution from the adsorbates and from bulk TiO_2, the latter previously having been neglected in Chapter 4.

Having established a framework for calculating complete O 1s spectra for adsorbates on the anatase (1 0 1) surface, in the rest of this chapter the method is put into practice for two interesting systems: H_2O and bi-isonicotinic acid (BINA).

7.3 The adsorption of water on anatase (1 0 1)

7.3.1 Introduction

Developing an understanding of the microscopic behaviour of water at anatase TiO_2 surfaces is an important challenge, given the material's high photocatalytic activity [184]. A fundamental question is whether, upon adsorption on the anatase surface, the H_2O molecules remain intact (molecular adsorption) or dissociate, forming hydroxyl (OH) groups. A DFT study of H_2O molecules on the anatase (1 0 1) surface found molecular adsorption to be energetically favourable [146], by 0.3–0.5 eV per molecule depending on surface coverage. The conclusion of this work, and most subsequent computational and experimental studies [214–216] was that water adsorbs molecularly on the anatase surface.

However, a high-resolution XPS study [217] of hydrated anatase films showed signatures of two different oxygen species over a range of temperatures, raising the possibility that there is a mix of dissociatively and molecularly adsorbed water at the surface. A similar pattern has been followed for the rutile (1 1 0) surface, with improved experimental techniques detecting signatures of dissociative adsorption at odds with previous theoretical predictions [218; 219]. Seeing that there are no calculations of O 1*s* spectra at the H_2O/TiO_2 interface in the literature, it would clearly be useful to calculate the different spectroscopic signatures of dissociative and molecular adsorption and compare the results to experiment.

7.3.2 Constructing interface models

The experiments of Ref. 217 were carried out on an anatase (1 0 1) single crystal. Accordingly the TiO_2 substrate was modelled as a 5.8 Å-thick slab of anatase cut along the (1 0 1) plane (c.f. Chapter 4) of lateral dimensions 10.4×15.2 Å^2 with a vacuum region of at least 14 Å separating periodic slabs. Otherwise precisely the same computational methodology was used as for Chapter 4, i.e. DFT using the PBE functional for exchange-correlation [54], plane wave expansions of the wavefunctions and density up to 35 and 200 Ry respectively, and ultrasoft pseudopotentials [65].

Each surface cell contains eight fivefold co-ordinated Ti atoms which act as adsorption sites for H_2O molecules. Five different interface models were considered, all assuming monolayer coverage i.e. eight H_2O molecules per unit cell. The fraction of molecularly adsorbed H_2O in the monolayer was varied as 1.0 (pure molecular), 0.75, 0.50, 0.25 and 0.0 (pure dissociative). The geometries of molecularly or dissociatively adsorbed H_2O molecules follow those introduced in Ref. 146. For each model the molecules were placed in the desired position, then

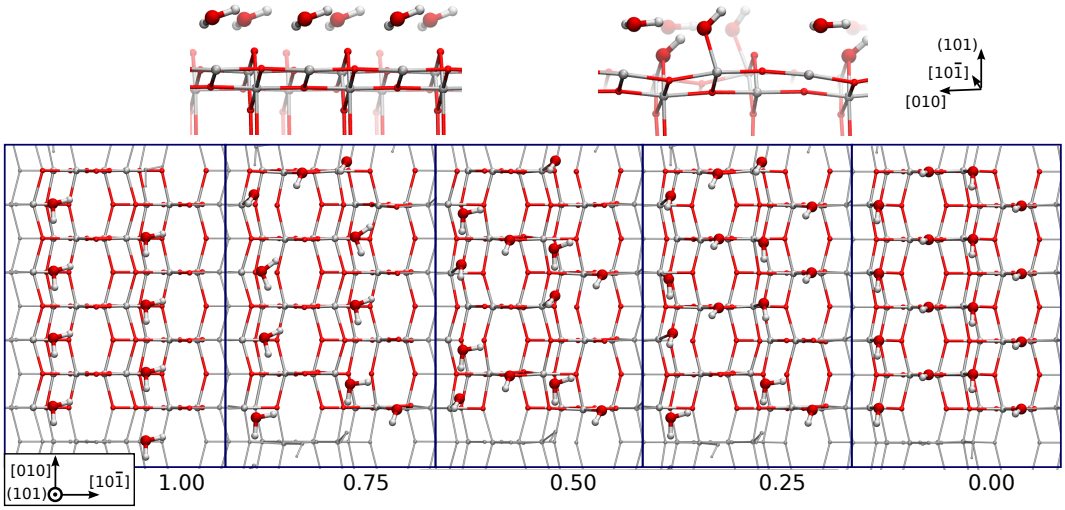

Figure 7.4: Ball-and-stick models of interface models of monolayers of H_2O on the anatase (1 0 1) surface. The top pictures demonstrate the role of H-bonding in ordering the molecules. In the pure molecular monolayer (top left) the H_2O molecules minimize their mutual interactions by rotating so that one H atom points out of the monolayer. When there is a mix of molecular and dissociated H_2O (top right) this rotation is unnecessary; in fact favourable H-bonds can be formed between the H_2O and the surface OH groups. The lower pictures give the view along the (1 0 1) normal of monolayers which have different proportions of molecular H_2O, going from 1.00 (pure molecular) to 0.00 (pure dissociated).

all atoms (except the lowest three layers of the slab) were relaxed with the BFGS algorithm until the force on each atom was below 0.03 eV/Å. Sampling different arrangements of molecular/dissociative molecules having the same coverage led to negligible differences in calculated total energies.

7.3.3 Geometries and energetics of interface models

Figure 7.4 shows the ball-and-stick representations of the five interface models viewed along different perspectives. The top part of the figure illustrates the importance of intermolecular interactions in determining the structure of the monolayer. In the case of pure molecular H_2O (left) all molecules rotate to minimise the unfavourable proton-proton interaction, so that one of the H atoms of

each molecule points out of the monolayer. The introduction of dissociated H_2O breaks this order and allows the formation of H-bonds between H_2O and the OH groups (right)

Considering the DFT total energy shows that the interface model with a 1.0 coverage of molecular H_2O is the most stable, with an adsorption energy per H_2O molecule of -0.64 eV, while the least stable is the pure dissociated monolayer with an adsorption energy of -0.45 eV. As the fraction of molecularly adsorbed water decreases, so does the stability, with the stability for coverages 0.75→0.50→0.25→0.0 going as -0.61 eV→-0.55 eV→-0.49 eV→-0.45 eV per molecule. Accordingly there is an energy cost of around 200 meV to dissociate one H_2O molecule in the presence of intermolecular interactions, leading to the same conclusion as previous calculations [146] that, on the basis of energetics, H_2O is expected to adsorb molecularly on anatase (1 0 1).

7.3.4 Calculation of O 1*s* spectra

Having obtained the structures it is now possible to use the methodology described in Section 7.2 and Figure 7.3 to construct the full O 1*s* spectrum. The O 1*s* binding energies were calculated for each interface model using the ΔSCF method first introduced in Chapter 2. The bulk O 1*s* binding energy E_{bulk} was set to 530.5 eV to match the experimental spectrum reported in Ref. 217. The δ-functions in equation 7.1 were replaced with gaussians of width 1.2 eV, and a value of 3 Å was used for the electron escape depth.

Figure 7.5(a) shows the calculated O 1*s* spectra for the five different fractions of molecular H_2O in the monolayer. The first general trend to note is that the O atoms in molecular H_2O have 1*s* binding energies around 4 eV higher than those of O atoms in bulk TiO_2, giving rise to a clearly visible peak in the spectrum at

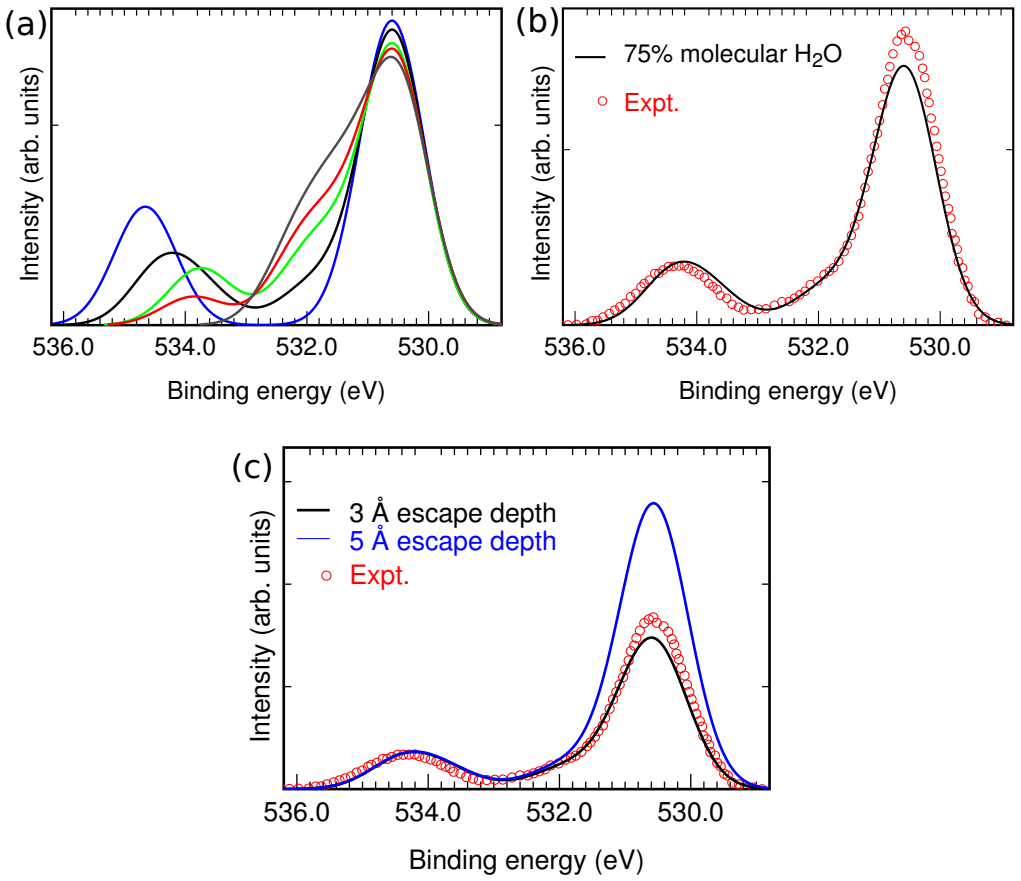

Figure 7.5: O 1*s* spectra calculated for interface models of H_2O monolayers on the anatase (1 0 1) surface. (a) Spectra for different proportions of molecular H_2O going from 1.00 (pure molecular, blue), 0.75 (black), 0.50 (green), 0.25 (red) and 0.00 (pure dissociated, grey). (b) O 1*s* spectrum calculated for a 3:1 ratio of molecular:dissociated water (i.e. 0.75, black line) compared to the experimentally-measured spectrum reported in Ref. 217 obtained at 230 K (red circles). Here the escape depth λ is set to 3 Å. (c) The spectrum calculated for the 3:1 model with different escape depths of 3 and 5 Å.

high binding energy. The surface OH groups have O 1s binding energies 1–1.7 eV higher than bulk TiO_2, thus appearing in the spectrum as a shoulder to the bulk peak. On moving from the pure molecular monolayer (blue line in Fig. 7.5) to the pure dissociated monolayer (grey line) the spectral weight is transferred from the distinct molecular peak to the shoulder.

The other trend is that, as the fraction of dissociated H_2O increases and H-bonded assemblies like that shown in Fig. 7.4 occur, the 1s binding energy of pure H_2O is reduced. As previously observed for the COOH groups of N3, the H-bonding has a dramatic effect on the 1s binding energy, shifting the high energy peak by 1.0 eV on going from the pure molecular monolayer to the 0.50 mix (green line). Interestingly the shift to lower binding energy does not continue with the 0.25 molecular coverage (red line), perhaps indicating that the optimum H-bonded geometry has already been reached at the 0.50 mix.

Fig. 7.5(b) compares the 75% molecular H_2O monolayer interface model to the experimental spectrum of Ref. 217 measured at 230 K. This temperature was chosen because it was the closest available match to 220 K, which according to the authors of Ref. 217 is the estimated temperature at which monolayer coverage was achieved. There is strong agreement between the calculated and experimental spectra, both in terms of peak positions and intensities. By contrast, in the spectrum of the pure molecular monolayer the separation of the H_2O and substrate peaks is overestimated by 0.6 eV, and no shoulder to the substrate peak is observed. The calculated spectra therefore strongly support the idea that there is a mix of molecular and dissociated H_2O on the anatase TiO_2 substrate.

In the analysis of Ref. 217 it was suggested that the shoulder to the substrate peak actually contained contributions from two different O species. The calculated binding energes confirm this suggestion, with the contributions at

531.6 eV from the OH groups bonded to the fivefold co-ordinated surface Ti, and at 532.0 eV/532.2 eV from the protonated substrate O atoms.

The value of 3 Å for the electron escape depth was chosen to match the experimental data, but falls into the acceptable range of 2–12 Å specified by the universal curve [169] for the photon energy of 610 eV used in Ref. 217 and a binding energy of around 530 eV. Fig. 7.5(c) shows the spectrum calculated with a larger escape depth of 5 Å. Increasing the escape depth increases the strength of the substrate peak, but the relative intensity of the H_2O contributions remains the same. Therefore the optimal matching of the 3:1 mix to experiment does not critically rely on the escape depth model.

7.3.5 Calculated stabilities vs. spectroscopy

There is clearly a puzzle concerning H_2O and anatase (1 0 1): according to calculations of the adsorption energy, there is a high cost associated with dissociating a H_2O molecule($\sim 10 \times k_B T$ at room temperature) yet the experimental O 1s spectrum shows the presence of dissociated H_2O. In fact, the same puzzle exists for rutile [218]. One possibility is that surface defects affect the energetics of adsorption [220; 221], so it would be interesting to calculate the O 1s spectrum in the presence of surface and subsurface O vacancies and Ti interstitials. Alternatively, there may be H-bonded supramolecular assemblies based on molecular and dissociated H_2O which are more elaborate than those considered here that may have a higher stability [222]. Either way, more work is essential to understand this important system.

7.4 Bi-isonicotinic acid on anatase (1 0 1)

7.4.1 Introduction

The second system considered here is the bi-isonicotinic acid (BINA) ligand $C_{12}N_2O_4H_2$, which consists of a bipyridine with two carboxylic acid groups. The N3 molecule carries two of these ligands, and as such it is an important model system in both experimental [159; 223; 224] and theoretical [225; 226] DSC research.

Early work on the BINA/TiO_2 interface focused on its adsorption on the rutile (1 1 0) surface [223]. The O 1*s* spectrum of the BINA-sensitized rutile surface reported in Ref. 223 shows two peaks. One peak is assigned to the substrate and the other to the adsorbate. The authors of Ref. 223 concluded that, since there was only one adsorbate peak, all four O atoms in the adsorbed BINA molecule must be chemically equivalent, i.e. all were bonded in the same way. Going back to the picture of carboxylic acid adsorption introduced in Chapter 4, this observation is consistent with both COOH groups binding in a bidentate bridge configuration (c.f. model I2a in Chapter 4).

Subsequent experiments on BINA-sensitized anatase films [159; 224] also showed two peaks in the O 1*s*, leading to the same assignment of binding proceeding through two bidentate bridges. However, first-principles calculations of the BINA molecule on the anatase (1 0 1) surface [226] identified a potential problem with the assignment, namely that one of the four Ti–O bonds formed between the molecule and the substrate was much longer than all the others—3.1 Å vs. 1.9–2.2 Å. In Chapter 4 the analogous interface model for the N3 dye, I2a, was also shown to have this elongated bond. The authors of Ref. 226 pointed out that it is questionable whether all four O atoms of BINA really are chemically equivalent

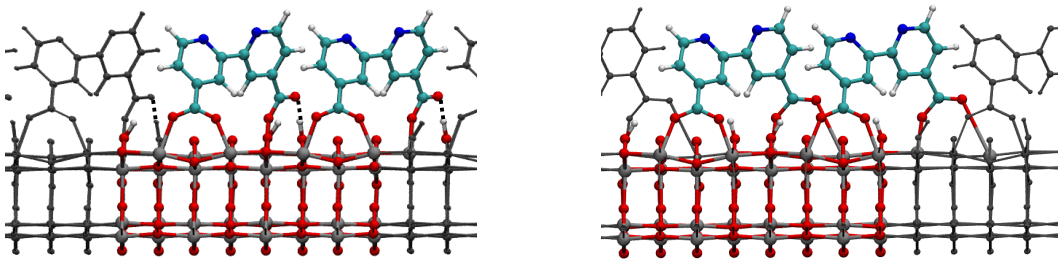

Figure 7.6: Ball-and-stick representations of two interface models of BINA on the anatase (1 0 1) surface. The generally accepted geometry [159], where both COOH groups adsorb as bidentate bridges, is shown on the right (note the elongated bond). The interface model on the left has one bidentate bridge and one ester-type mode; the H-bonds are shown as dashed lines.

when the molecule is adsorbed through two bidentate bridges.

It was however shown in Chapter 4 that large changes in structural parameters do not necessarily have large effects on the O 1*s* spectrum. The motivation of the work presented in the following sections is to check this statement for the case of BINA and thus seek to reconcile the experimental and theoretical data.

7.4.2 Construction of interface models

Interface models of the BINA/TiO_2 interface were constructed using the same anatase slab and computational parameters as for the H_2O adsorption models introduced in Section 7.3.2. Each model contains two BINA molecules per unit cell, amounting to monolayer coverage.

The ball-and-stick representations of the two interface models considered here are shown in Figure 7.6. The interface model based on two bidentate bridges proposed in Ref. 159 and investigated in Ref. 226 is shown on the right. The elongated bond (3.3 Å) can be clearly seen. The model on the left of Fig. 7.6 has one COOH group adsorbed as a bidentate bridge, and the other group in an ester-type mode. The O atom which previously had the elongated Ti–O bond instead

now forms a H-bond with a surface OH group. In the following this ester-type interface model will be referred to as the 'H-bonded' configuration.

7.4.3 Energetics of interface models

In Ref. 226 the interface model with two bidentate bridges was found to be the most stable out of the three configurations considered. However the H-bonded configuration considered here is significantly more stable again, by 0.51 eV per BINA molecule. In the H-bonded configuration the two pyridine rings twist, allowing the second COOH group to simultaneously form a strong Ti–O bond and a H-bond.

Of course, throughout this thesis it has repeatedly been stressed that the use of energetics alone to assign adsorption geometries is not sufficient. Indeed it might be expected that, since the four O atoms are even more strongly inequivalent in the H-bonded configurations this geometry might produce an O 1*s* spectrum in poor agreement with the experimental data. The next section shows this not to be the case.

7.4.4 O 1*s* spectra of interface models

Figure 7.7 shows the O 1*s* spectra calculated for the two interface models of BINA on the anatase (1 0 1) surface. Also shown is the experimental spectrum reported in Ref. 159 for BINA-sensitized anatase films, measured at a photon energy of 600 eV. The spectra were calculated through the procedure shown in Fig. 7.3 and equation 7.1. The δ-functions were replaced with gaussians of width 1.2 eV and the escape depth λ was set to 3.5 Å. As for H_2O these values were chosen to best fit the experimental data. λ=3.5 Å lies in the acceptable range of 1.5–10 Å given

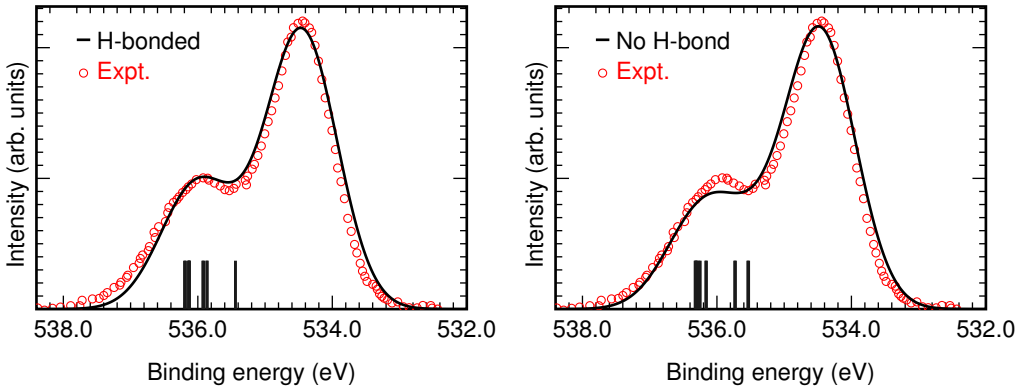

Figure 7.7: O 1s spectra calculated for the two interface models shown in Fig. 7.6 (black lines) compared to the experimental spectrum of Ref. 159 (red circles). The bare (i.e. without gaussians convolved on top) 1s binding energies of the O atoms of the COOH and surface OH groups are also shown, as vertical lines.

in Ref. 169 at a photon energy of 65 eV. E_{bulk} was set to 534.3 eV.

The principal result of the current calculations is that both models account well for the experimental spectrum. There is an adsorbate peak and a substrate peak; any fine structure of the adsorbate peak cannot be resolved when the 1.2 eV gaussians are applied. The adsorbate peak is formed from the four O atoms of BINA and the two surface OH groups.

For the H-bonded model, the four contributions from BINA show remarkably little deviation, with binding energies clustering in the interval 535.8–536.2 eV. The OH group which does not participate in the H-bonding also appears in this region, at 536.1 eV. The H-bonded OH group contributes at 535.4 eV.

In the calculated spectrum of the non-H-bonded model, the adsorbate peak is slightly less well-resolved due to a larger variation in the 1s binding energies of the O atoms in the COOH groups. The O atoms on the regular bidentate bridge have 1s energies of 536.3 eV. On the other COOH group, the O atom with the elongated Ti–O bond has a 1s energy of 535.5 eV, and the other O atom belonging to the same group has an energy of 535.7 eV. The two surface OH

groups, neither of which participate in any H-bonding, both appear at 536.2 eV in the spectrum, overlapping with the bidentate bridging O atoms.

7.4.5 BINA on TiO_2—outlook

The original aim of this section was to ascertain whether the "standard" atomistic model of the BINA/anatase interface, based on both COOH groups adsorbing in bidentate bridge modes, produced an O 1*s* spectrum consistent with XPS data. According to Fig. 7.7 the answer to this question is yes. However in the course of constructing the interface model another geometry was found which had a 0.51 eV higher stability and whose O 1*s* spectrum displayed equal, if not superior, agreement with experiment. A logical next step would be to perform a systematic investigation of other possible binding modes, as performed in Chapter 4 for N3. Although the HOMO-LUMO gap of BINA is too large to make it a viable sensitizer in DSCs [159], its ubiquitous use as a binding ligand in larger molecules marks the importance of understanding its interaction with TiO_2 surfaces.

7.5 Conclusions

In this chapter a method of calculating O 1*s* spectra of molecules adsorbed on the anatase (1 0 1) surface was presented which, in contrast to the calculations of Chapter 4, allowed access to the 1*s* binding energies of all O atoms, whether located at the surface or deep within the TiO_2 substrate. The approach takes separate calculations—one on a thick, clean slab, the others on thin slabs with molecules adsorbed on the surface—and combines them to produce a full spectrum. Escape depth effects are also included in the approach.

The methodology was applied to three systems involving the anatase (1 0 1)

surface. First the clean substrate was considered, where it was shown that the O 1*s* spectrum might be expected to show some fine structure in very high resolution experiments. Next, the important system of H_2O and anatase was treated where it was shown that, despite not being the most stable interface model, a 3:1 mix of molecular and dissociated H_2O molecules had the O 1*s* spectrum in closest agreement with experiment. The final system was the prototype DSC ligand of bi-isonicotinic acid (BINA), where the two interface models considered both showed good agreement with the experimental O 1*s* spectrum. An interface model where one COOH group forms H-bonds with a surface OH group was found to have higher stability that the conventional model, where both COOH groups form bidentate bridges.

In the case of H_2O the calculations confirmed the experimental claim that dissociated water was present at the interface, and that two different OH species were present. For BINA, the 1*s* binding energies are only weakly affected by large changes in geometrical parameters which is not in line with intuition. Both systems demonstrate the valuable contribution that first-principles calculations can make to interpreting and assigning experiments on complex interfaces.

Chapter 8

Semiconductor-sensitized solar cells

In this chapter, I take some of the methods and techniques used to study the behaviour of dye-sensitized solar cells in previous chapters and apply them to a novel design of photovoltaic device, the so-called semiconductor-sensitized solar cell (SSC). In particular, I consider devices based on TiO_2 films sensitized with the compound Sb_2S_3, called stibnite. Compared to DSCs, SSCs are in their infancy and have not been characterised to the same extent. As such the spirit of this chapter is to take physical approximations and semi-empirical corrections to construct a plausible working model of the interface, which can serve as a base for future work. In particular the investigation extends to two other materials, bismuthinite and antimonselite, which are isostructural to stibnite. There, antimonselite is identified as a potentially strong candidate material for future photovoltaic devices.

The work presented in this chapter was previously published in Ref. 227.

8.1 Introduction

The original designs of dye-sensitized solar cells employed mesoporous TiO_2 films, Ru-based dyes like N3, and a liquid electrolyte to regenerate the oxidised dye [15]. One important design goal is to replace the liquid electrolyte with a solid-state hole transporter, which does not suffer from the problem of solvent leakage [40; 43; 228]. Another is to replace metal-organic dye sensitizers based on rare and expensive metals with cheaper light absorbers such as organic dyes [229–231] or semiconductor quantum dots [232–234]. An advantage of quantum dots is that their optical gap can be tuned by varying the size of the dot [235].

In 2009–2010 a new device concept was illustrated based on mesoporous anatase TiO_2 films sensitised with nanocrystals of the semiconductor stibnite (Sb_2S_3). Employing either the polymer poly(3-hexylthiophene) (P3HT) [236] or the inorganic *p*-type semiconductor CuSCN [237] as a hole-transporter yielded all-solid-state devices with power conversion efficiencies of 5.1% and 3.4% respectively. These encouraging numbers triggered an expansion in research efforts devoted to further understanding and optimising these "semiconductor-sensitized solar cells" (SSCs) [17].

In the devices of Ref. 236 charge injection occurs at the Sb_2S_3/TiO_2 interface. Due to its low optical absorption onset (1.7 eV in bulk [238]) and its high absorption coefficient in the visible (7.5×10^4 cm^{-1} [239]), stibnite is a very promising material for thin film photovoltaics. However only a small number of computational studies have been performed on stibnite [240–243], none of which have focused on the formation of interfaces. The purpose of this chapter is to develop an atomistic model of the Sb_2S_3/TiO_2 interface and study its electronic properties.

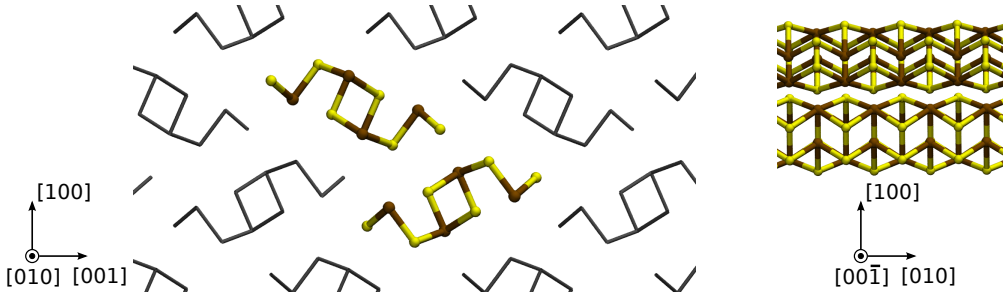

Figure 8.1: Ball-and-stick model of the crystal structure of stibnite (Sb_2S_3) viewed along the **b** and **c** directions. The two $(Sb_4S_6)_n$ ribbons which make up the orthorhombic unit cell are highlighted. Colour code: Sb, brown; S, yellow.

8.2 Atomistic and electronic structure of bulk stibnite

8.2.1 The X_2Y_3 compounds

Stibnite belongs to a wider class of metal chalcogenides with the formula X_2Y_3 where X = Sb or Bi and Y = S or Se. In their mineral form the compounds crystallise in the unusual crystal structure (belonging to the space group *Pnma*) shown in Figure 8.1 [244]. The orthorhombic unit cell consists of two covalently-bonded $(X_4Y_6)_n$ ribbons running along the [0 1 0] direction, which interact with each other through van der Waals forces. The 20-atom unit cell is completely specified by the co-ordinates of one X_2Y_3 unit [240].

The lattice parameters, atomic positions and compressibilities of bulk stibnite were measured over a range of pressures in Ref 244. The lattice constants at ambient pressure were measured to be a=11.32 Å, b=3.84 Å and c=11.23 Å. The compressibility along the **b** direction was found to be much lower than along **a** or **c**, (26 GPa and 92 GPa, respectively) confirming that the inter-ribbon van der Waals interactions are far easier to overcome than the covalent bonds along the ribbon axis.

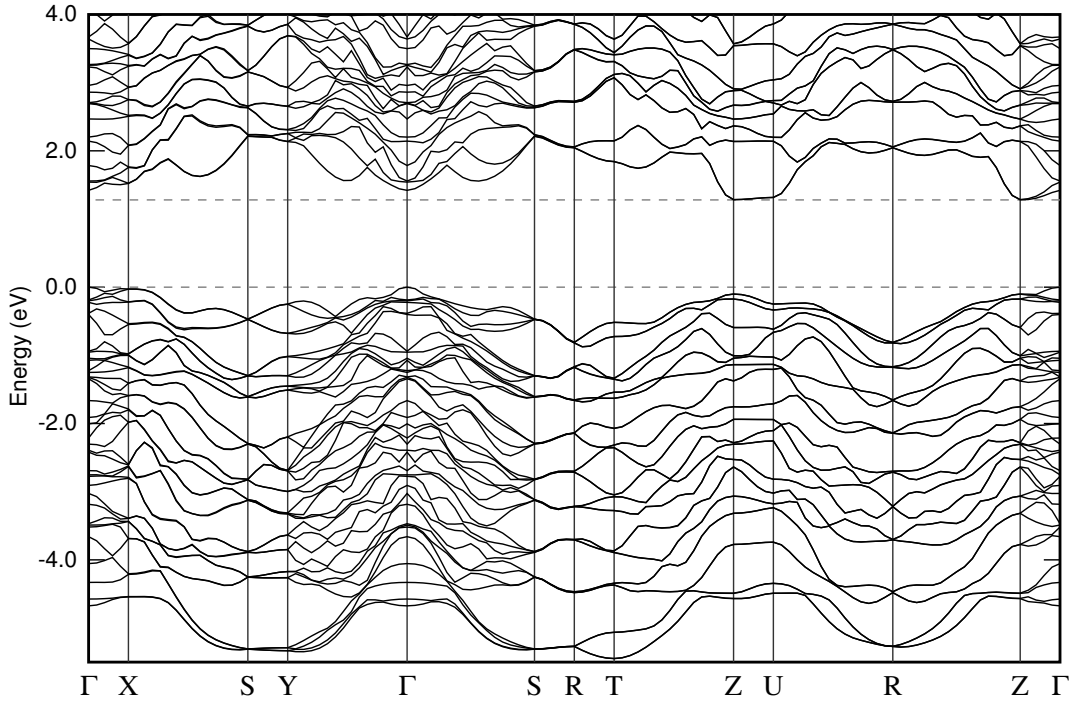

Figure 8.2: Band structure of stibnite plotted along high-symmetry directions. The energy zero is set as the top of the valence band at Γ. The dashed lines mark the energies of the band edges. In units of reciprocal lattice vectors, the co-ordinates of the special k-points [240] are $X = \frac{1}{2}\ 0\ 0$, $S = \frac{1}{2}\ \frac{1}{2}\ 0$, $Y = 0\ \frac{1}{2}\ 0$, $R = \frac{1}{2}\ \frac{1}{2}\ \frac{1}{2}$, $T = 0\ \frac{1}{2}\ \frac{1}{2}$, $Z = 0\ 0\ \frac{1}{2}$ and $U = \frac{1}{2}\ 0\ \frac{1}{2}$.

8.2.2 Electronic structure

Figure 8.2 shows the DFT band structure obtained for stibnite using the experimental atomic positions and lattice constants reported in Ref. 244. Exchange-correlation was treated with the PBE functional [54] and the core-valence interaction described by norm-conserving [64] and ultrasoft [65] pseudopotentials for Sb and S atoms, respectively. The Sb 4*d* semicore states were not included in the valence. The wavefunctions and densities were expanded in plane waves as implemented in `Quantum ESPRESSO` [141]. The band gap was found to be converged with plane wave cutoffs of 35 and 200 Ry for the wavefunctions and density. Increasing the plane-wave cutoff to 40 Ry found a change in total energy of 1 meV

per atom. The Brillouin zone was sampled on a 2×4×2 Monkhorst-Pack grid.

The large unit cell results in a rather complicated band structure. The valence band is dominated by S 3*p* states while the conduction band contains sizeable contributions from both Sb 5*p* and S 3*p* states [240; 241]. According to Fig. 8.2 stibnite is an indirect gap semiconductor, with a minimum gap of 1.28 eV between the Γ and *Z* points. The minimum direct gap is 1.38 eV at the *Z* point. Strangely, previous computational studies either neglect to specify whether their calculated band gap is indirect or direct [240] or do not consider the *Z* point in their calculations [241; 242]. However recent LDA calculations employing the same methodology also find the minimum gap to be indirect (at 1.20 eV) with the direct gap 0.09 eV higher [245].

There is also some confusion in the literature regarding the experimental band gap of stibnite, but it is generally quoted to be direct with a value of 1.7–1.8 eV [236; 238; 239; 246]. The fact that experiments find a direct gap is not necessarily incompatible with the DFT predictions, since the 0.1 eV difference is rather small. For instance, thermal motion could shift the band edges such that ordering changes, while experimentally it may not even be possible to resolve a weak indirect onset preceeding the direct absorption edge.

8.3 Interface model of the Sb_2S_3/TiO_2 interface

8.3.1 Constructing an interface model

To model the Sb_2S_3 interfaces found in the devices of Refs. 236 and 237, it is necessary to move from the bulk picture to a surface, as performed in Chapter 4 for TiO_2. The difference here however is that the surface science of stibnite has been far less thoroughly investigated compared to anatase TiO_2. Furthermore

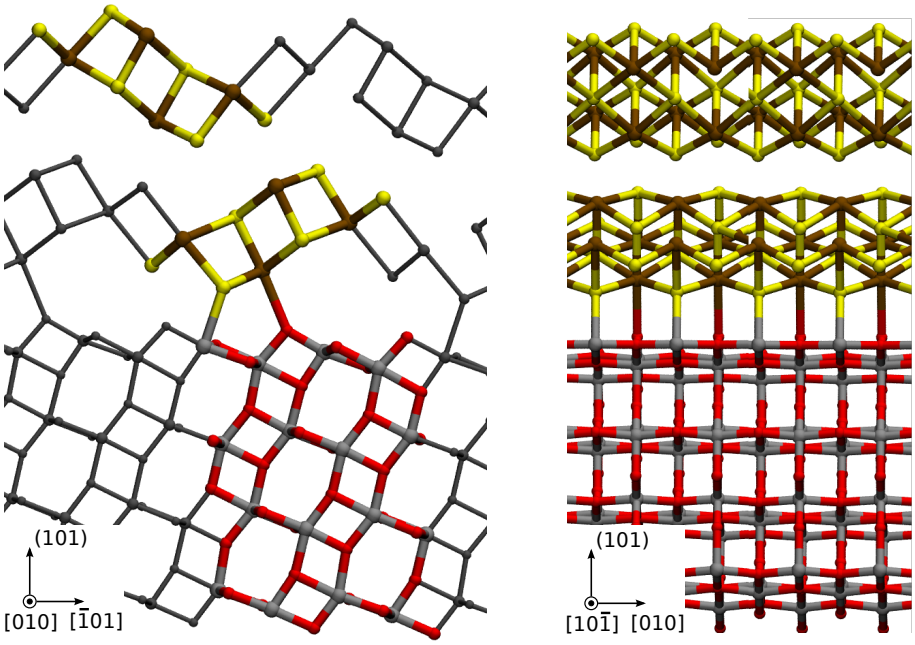

Figure 8.3: Structurally-relaxed model of the Sb_2S_3/TiO_2 interface constructed as discussed in the text, viewed along the [0 1 0] and [1 0 $\bar{1}$] directions. The axes refer to the anatase TiO_2 crystal co-ordinate system.

the morphology of the interface has not been characterised by XPS or infrared experiments. Instead it is necessary to invoke physical intuition to construct a plausible interface model, which is shown in Figure 8.3.

The interface model was generated based on the following considerations:

- Since the devices of Refs. 236 and 237 both employ mesoporous TiO_2 films like DSCs, the same arguments as given in Section 4.1.3 for modelling the TiO_2 substrate as an anatase (1 0 1) slab apply here.

- Stibnite cleaves along the approximate [0 0 1] direction, i.e. between the ribbons. It is therefore likely that Sb_2S_3 nanocrystals will adsorb on the TiO_2 substrate with the $(Sb_4S_6)_n$ ribbons running parallel to the (1 0 1) surface. This adsorption mode does not require the breaking of any covalent bonds and therefore should be energetically favourable.

- TiO_2 and Sb_2S_3 are lattice-matched along the direction of the $(Sb_4S_6)_n$ ribbons. In fact the repeat unit of TiO_2 (1 0 1) along the [0 1 0] direction is 3.79 Å [139], and the stibnite lattice parameter is 3.84 Å [244], yielding a compressive strain on Sb_2S_3 below 1%. The lattice parameter of the TiO_2 surface cell in the $[1\,0\,\bar{1}]$ direction is 10.24 Å compared to the stibnite c parameter of 11.23 Å. This results in a 9% strain of stibnite in the direction perpendicular to the ribbons, which can easily be accommodated since Sb_2S_3 is very compressible along this direction (c.f. Section 8.2.1). Such compressive strain results in very small changes of the bulk band structure of stibnite (the gap at the Z point of the Brillouin zone changes by less than 0.2 eV, and the gap at Γ changes by only 0.03 eV).

- Considering the formation of bonds between TiO_2 and Sb_2S_3, based on the formal charges of the atoms [138; 247], it can be expected that the Ti^{4+} and O^{2-} atoms in the substrate will tend to form bonds with the S^{2-}/S^{3-} and Sb^{3+} in the stibnite, respectively. Therefore the most energetically-favourable adsorption model should maximise the likelihood of Ti–S and/or O–Sb bond formation.

8.3.2 Relaxing the structure

The relaxed structure of the proposed interface model was first calculated in DFT-PBE [54]. The TiO_2 surface was modelled as a rectangular anatase slab of area 10.4×11.4 $Å^2$ and of thickness 12.8 Å (eight TiO_2 layers), constructed from the lattice parameters obtained in the bulk relaxations described in Section 4.1.3. The stibnite was modelled as two $(Sb_4S_6)_3$ ribbons per unit cell. A vacuum region of 8 Å was inserted between periodic replicas and the self-consistent electrostatic

dipole correction of Ref. 71 employed to remove spurious interactions. The structure was relaxed in a damped Car-Parrinello molecular dynamics simulation with the bottom three atomic layers of the TiO_2 slab fixed in their bulklike positions, and structural relaxations were carried out until the force on each atom was below 0.07 eV/Å.

The ball-and-stick model shown in Fig. 8.3 is the relaxed structure. As can be seen, there is one Ti–S and one O–Sb bond per Sb_4S_6 unit, which have lengths 2.67 and 2.81 Å. These values are comparable of the bond lengths within the stibnite ribbons (2.5–2.9 Å).

8.3.3 Adsorption energetics

The stability of the proposed interface model can be checked by calculating the adsorption energy similar to Section 4.3, except that in this case when the energies of the isolated components were calculated only the electrons were allowed to relax. This procedure directly gives the energy of the bonds without the additional contribution from the relaxation of the ultrathin stibnite nanoribbons. The energy per bond was calculated with the PBE functional to be 0.19 eV for the relaxed interface model.

One additional complication at this interface is that van der Waals (vdW) forces, which play an important role in stibnite, are not described in local-density or generalised-gradient approximations (LDA/GGA) to exchange and correlation (e.g. Ref. 248). Although a number of density-functionals exist which include vdW corrections, these have not yet been tested on interfaces like that in Fig. 8.3. On the other hand, noting the GGA and LDA underestimate and overestimate the binding energies respectively, repeating the structure construction and relaxation in the LDA gives an upper limit to the adsorption energy of 0.43 eV per

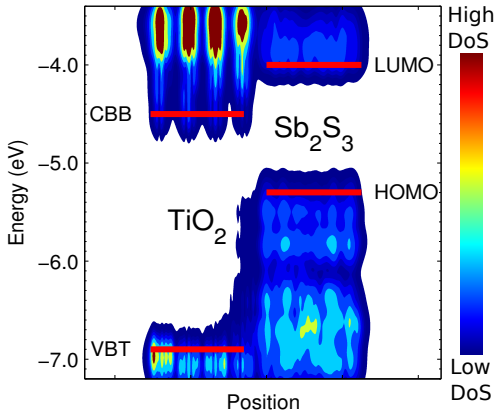

Figure 8.4: The local DoS (defined in equation 8.1) calculated for the Sb_2S_3/TiO_2 interface. "High" and "low" DoS equate to 0.05 and 0.01 states $eV^{-1}Å^{-3}$, respectively. The highest occupied/lowest unoccupied states of the TiO_2 and Sb_2S_3 slabs are marked as horizontal red lines. A constant shift was added to all energies to match the measured 6.9 eV ionization potential for TiO_2 with respect to the vacuum level [249].

bond. For this calculation the LDA-relaxed anatase lattice parameters presented in Table 4.2 were used to construct the anatase slab, and new pseudopotentials were used that were consistent with the parameterisation of the LDA of Ref. 53. Having confirmed that the interface model is stable in both the GGA and LDA, the next step is to consider its electronic properties.

8.4 Electronic structure of the interface

8.4.1 Local and projected densities-of-states

Given the better description of TiO_2 provided by the PBE functional (c.f. Table 4.2) in the following the PBE-relaxed structural model will be used. Moving to the electronic structure, a direct means of visualising the energy levels of TiO_2 and Sb_2S_3 is to consider the local planar-averaged density of states, shown in

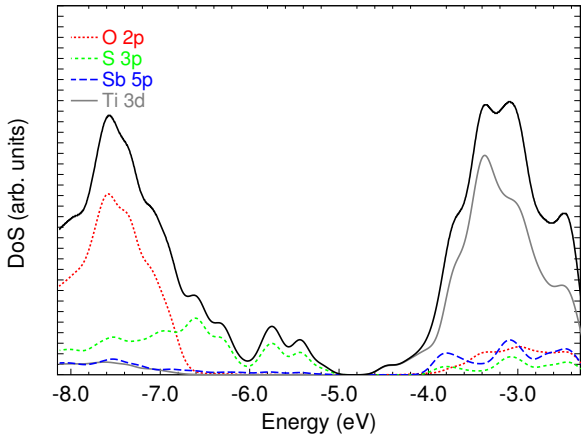

Figure 8.5: The total DoS of the Sb_2S_3/TiO_2 interface (black line) and its projections onto pseudo-atomic orbitals. The same energy shift was applied as in Fig. 8.4. The energy gap of the entire interface lies between -5.0 and -4.6 eV.

Figure 8.4. This 2D function is obtained as

$$g^{\mathrm{LDoS}}(E,z) = \sum_n \frac{1}{L_x L_y} \int_0^{L_x} \int_0^{L_y} |\psi_n(\mathbf{r})|^2 dx dy \; \delta(E-\varepsilon_n) \tag{8.1}$$

where the position co-ordinate z is taken along the normal to the (1 0 1) plane. Peaks in $g^{\mathrm{LDoS}}(E,z)$ correspond to the presence of states with energy E within the layer at z.

The contour plot of $g^{\mathrm{LDoS}}(E,z)$ nicely mirrors traditional band alignment diagrams. In particular the HOMO and LUMO of stibnite lie above the TiO_2 valence and conduction band edges, forming a type-II (staggered gap) heterostructure, as is desired for photovoltaic applications.

An alternative analysis leading to the same conclusion is to consider the projected density-of-states introduced in equation 5.1. Figure 8.5 shows the projections of the total DoS (black line) onto the O $2p$, Ti $3d$, Sb $5p$ and S $3p$ orbitals. The tailing off of the O $2p$ projection (red line) while the S $3p$ contribution (green line) remains large highlights the presence of the Sb_2S_3 valence band in the TiO_2

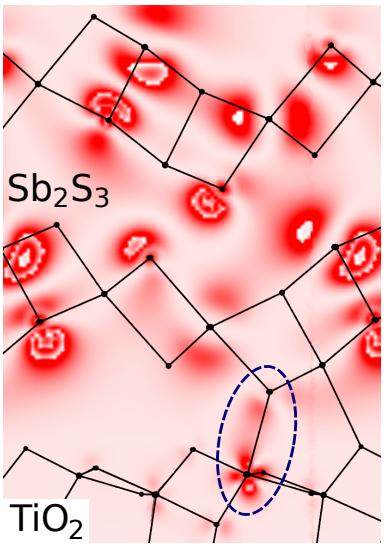

Figure 8.6: Isovalue plot of $|\psi(x, y_0, z)|^2$ for the Sb_2S_3 LUMO, where y_0 belongs in a plane whose normal points along the [0 1 0] direction and contains a Ti–S bond. Connected regions of the same colour correspond to isovalues of $|\psi|^2$. The lobes of the S and Sb p orbitals can be clearly distinguished, as can a coupling to a Ti 3d orbital (circled).

gap; similarly the Ti 3d projection (grey line) appears 0.5 eV lower in energy than the stibnite conduction band.

8.4.2 Structure of KS orbitals

In nanostructured photovoltaics, the photocurrent is generated through electron injection from the photoexcited adsorbate to the conduction band of the substrate. The rate of injection depends on the magnitude of the coupling matrix element between the localised excited state and the conduction band manifold [150; 250; 251]. Supposing that the lowest unoccupied Kohn-Sham (KS) state on the stibnite is a good approximation to the quasiparticle wavefunction of the photoexcited electron, it is interesting to consider its spatial distribution.

Figure 8.6 shows the stibnite LUMO plotted in a plane which contains a Ti–S bond. Connected regions of the same colour correspond to isovalues of the KS

wavefunction. The strongest features in the plot are the lobes of the S and Sb p orbitals. However there is also a direct coupling between the S $3p$ states and Ti $3d$ orbital, circled in the figure. Therefore there is possibly a direct pathway for carrier injection through the Ti–S bond.

8.4.3 Energy-level alignment

Figure 8.4 also has the band edges of TiO_2 and the HOMO/LUMO of Sb_2S_3 marked as horizontal lines. The DFT-calculated gaps of the anatase slab and the stibnite layer are 2.38 and 1.30 eV, respectively. It is interesting to note that the gap of the ultrathin Sb_2S_3 layer is only 0.02 eV larger than that calculated for bulk in Section 8.2.2, i.e. there is a neglible quantum confinement effect in this case. The HOMO/VBT offset for the interface model is found to be 1.64 eV in DFT.

Now, in order to calculate a quasiparticle energy-level alignment, one could follow the procedure of Chapter 6, and calculate the quasiparticle and image-charge corrections at the Sb_2S_3/TiO_2 interface. However thanks to the relative novelty of these devices, the valence photoemission spectrum of the interface has not yet been reported in the literature. This, together with the uncharacterised morphology of the interface and the significant computational expense of determining the quasiparticle corrections of Sb_2S_3 [245] places such an effort outside the scope of the current work. Instead the DFT alignment and experimental band gaps will be used to compare the potential application of other members of the X_2Y_3 family to SSCs.

8.5 Extending to other X_2Y_3 sensitizers

8.5.1 Introduction

As pointed out in Section 8.2.1 replacing Sb with Bi and/or S with Se forms stable compounds with the same structure. The variation of the lattice parameter along the $(X_4Y_6)_n$ ribbon direction is less than 0.3 Å across the family, so there exists the same lattice-matching with anatase TiO_2 along the [0 1 0] direction. Therefore the arguments made for forming the stibnite/TiO_2 interface in Section 8.3.1 may be applied to antimonselite (Sb_2Se_3), bismuthinite (Bi_2S_3) and guanajuatite (Bi_2Se_3). However it is the rhombohedral, topologically-insulating phase of Bi_2Se_3 [252] which is more stable in ambient conditions. As such, guanajuatite shall not be considered in the following.

8.5.2 Relaxing new interface models

A straightforward computational approach was employed to construct interface models employing new sensitizers. The relaxed structure of the stibnite/TiO_2 interface was used as a starting point for a damped Car-Parrinello relaxation (with the same computational parameters as in Section 8.3.2, with the PBE functional used to treat exchange-correlation), where the pseudopotentials of Sb (S) were replaced with Bi (Se). A norm-conserving pseudopotential was used for Bi (6*s* and 6*p* states in the valence) while an ultrasoft pseudopotential was used for Se (4*s* and 4*p* states in the valence). The Ti–Y/O–X bonds exhibit small variations across structures, with lengths of 2.67/2.83 Å for Sb_2Se_3 and 2.68/2.88 Å for Bi_2S_3, compared to 2.67/2.81 Å for Sb_2S_3.

8.5.3 Electronic structure and energy-level alignments

The electronic structure of the interface models employing the new sensitizers obey the same trends as for stibnite and TiO_2. As for stibnite, the energy-levels form type-II heterojunctions, so that according to DFT all of these sensitizers should be suitable for photovoltaic applications. The DFT-calculated HOMO/VBT offsets are 2.13 eV for Sb_2Se_3 and 1.51 eV for Bi_2S_3. The calculated gaps of the slabs of Sb_2Se_3 and Bi_2S_3 are 0.77 eV and 1.22 eV.

8.5.4 Device performance—open-circuit voltage

Under a number of assumptions (Chapter 1), the difference between the conduction band bottom (CBB) of TiO_2 and the HOMO of the sensitizer provides an idealised maximum open-circuit voltage. Taking the difference between the DFT-calculated CBB and HOMO would find values of 0.74 eV for Sb_2S_3, 0.25 eV for Sb_2Se_3 and 0.87 eV for Bi_2S_3.

However these values do not include corrections for the band-gap problem. The simplest, semi-empirical correction scheme is to estimate the position of the sensitizer LUMO by taking the reported (optical) gaps from Ref. 238 of 1.7, 1.2 and 1.3 eV for Sb_2S_3, Sb_2Se_3 and Bi_2S_3 and add these to the DFT HOMO positions. Similarly the TiO_2 CBB is estimated by adding the experimental gap of 3.2 eV [184] to the DFT VBT. The band edges obtained with this procedure for the three semiconductor sensitizers are shown in Fig. 8.7.

Once these corrections have been applied there is a qualitative change in the energy-level alignments at the interface. Stibnite and antimonselite (Sb_2S_3 and Sb_2Se_3) still have type-II character, with their LUMOs sitting above the corrected TiO_2 CBB (red dashed line). In fact their LUMOs lie at very similar

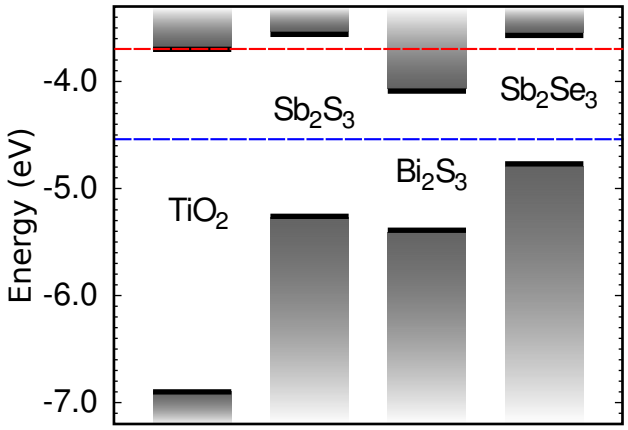

Figure 8.7: Energy-level alignments calculated for different semiconductor sensitizers. The edges of the lower grey bars are the highest-energy occupied states calculated in DFT. The higher grey bars are the lowest unoccupied states which have been shifted so that the gaps match those reported in Refs. 238 and 184. The blue dashed line is the position of the TiO_2 conduction band bottom in DFT, and the red dashed line is with the scissor correction. Note that the conduction band edge of bismuthinite Bi_2S_3 lies above and below the blue and red lines, respectively.

energies, indicating that they should display similar charge-injection properties. However the LUMO of bismuthinite (Bi_2S_3) now lies below the TiO_2 CBB, which means charge injection from this state into the CBB conduction band manifold is energetically forbidden.

8.5.5 Comparison to experiment

Given the rather extreme approximations made in the correction scheme— using optical gaps instead of quasiparticle gaps; assuming that the HOMO/VBT offset is calculated correctly in DFT; taking the simplest model interface—it is important to question whether the alignments presented in Fig. 8.7 have any experimental support. In a study of Bi_2S_3-sensitized TiO_2 films [253] it was observed that electron injection into the substrate only occurred for the smallest Bi_2S_3 nanoparticles, whose band gaps were enlargened by quantum confinement. Furthermore,

subsequent studies [254; 255] (performed after the results of this chapter were published) found that efficient electron injection occurred for Sb_2Se_3-sensitized TiO_2, but not for Bi_2S_3. Therefore the qualitative results of Fig. 8.7 have indeed been verified experimentally.

8.6 Conclusions and outlook

This short chapter has, albeit superficially, applied the approach described in Chapters 4–6 for N3-sensitized TiO_2 to SSC interfaces of deriving a structural model, considering the electronic structure of the sensitizer in isolation, then aligning energy-levels at the interface. In contrast to N3/TiO_2 there is a lack of experimental characterisation data of the Sb_2S_3/TiO_2 interface, preventing a systematic and quantitative comparison between theory and experiment. Indeed the spirit of this work is more to identify new and interesting systems, rather than trying to advance the fundamental understanding of a well-established interface.

Two key results were presented in this chapter. First, antimonselite-sensitized solar cells (Sb_2Se_3/TiO_2) should have similar charge-injection behaviour to those based on stibnite. The fabrication of such devices is the subject of current research [254]. The 1.2 eV optical gap of antimonselite is closer to the ideal Shockley-Queisser value [256] than stibnite which should lead to superior cell performance. In fact, using the method of estimating solar cell efficiency presented in Ref. 228, the experimental gaps and calculated band offsets yield a relative efficiency increase of $\sim$20% for Sb_2Se_3 sensitization compared to Sb_2S_3, showing that this a design concept worth pursuing.

The second result concerns the magnitude of the ideal open-circuit voltage for stibnite-sensitized solar cells. According to the calculated difference in the

energies of the TiO_2 CBB and the Sb_2S_3 HOMO, the ideal maximum is 1.6 V, which far exceeds the values of 0.42–0.56 V obtained in Ref. 236. The calculated open-circuit voltage does not take into account the loss-in-potentials associated with the hole-transporter, the electrodes, the quasi-Fermi level of the substrate, and the resistive losses in the device [228]. It should also be noted that recombination in the hole-transporter can affect the open-circuit voltage of the complete solar cell [17; 257; 258]. Nonetheless the calculations indicate that there is room for further optimisation of the devices of Refs. 236 and 237.

From the theoretical point of view, there are some more avenues for exploration. The first is the quasiparticle properties of the X_2Y_3 compounds, which are under current investigation [245]. The unusual crystal structure and the presence of heavy metals should present an interesting test of the *GW* approximation, and given the increasing importance of these materials for photovoltaics (and also thermoelectrics [259]) a thorough theoretical analysis is called for. In terms of the interface, the effect of van der Waals corrections on adsorption energetics and electronic structure should be investigated. Furthermore, if SSCs rise to the same level of importance as DSCs, it is reasonable to expect that there will be experimental attempts to characterise the interface, which could be paired with theoretical calculations of spectra.

A final, important point that has not been given much attention in this chapter is the role of the poly(3-hexylthiophene) (P3HT) layer in the devices of Ref. 236. This nominally acts as a hole transporter, but its 1.9 eV optical gap leads to P3HT being used as a light-absorber in hybrid organic/inorganic solar cells [260]. Therefore in SSCs it is likely that the P3HT plays a dual role as a hole transporter and a light-absorber. As such the P3HT/Sb_2S_3 interface would also be an interesting system to study.

Chapter 9

Conclusions

9.1 General overview

As a final chapter to this thesis, it is appropriate to summarise the principal results and to consider how the work might influence future research directions. The basic unifying theme of the research presented here is to use first-principles calculations to investigate the basic physics of interfaces relevant to the development of novel solar cells. A particular emphasis has been placed on photoemission (PES) experiments as a probe of the atomistic and electronic structure of dye-sensitized solar cell (DSC) interfaces. In these devices photocurrent generation occurs on the nanoscale, so any theoretical description must be grounded in quantum mechanics. Indeed, understanding the experimentally-measured spectra requires sophisticated theoretical approaches which tackle the many-electron problem, both in the ground state and for excitations. Employing these methods to describe complex interface models lies at the frontier of what is achievable with current computational capabilities, and tests our fundamental understanding of nanoscale phenomena.

9.2 Core-level PES and atomistic structure

Bombarding a sample with high-energy photons and measuring the kinetic energy of emitted photoelectrons allows the binding energy of the most tightly bound electronic states to be determined. Calculating these binding energies from first principles and comparing to the experimental spectra gives information about the chemical bonding at the interface. The main part of this thesis focused on the prototype DSC interface between the N3 dye and anatase TiO_2. Calculations on a number of candidate interface models showed a rather weak dependence of core-level spectra on geometrical parameters. Furthermore a quantitative discrepancy was identified between experiment and theory for models based on dye molecules isolated on the surface. Introducing contaminant molecules in the form of H_2O showed that H-bonding of carboxylic acid groups induced a notable change in spectra. Based on this observation, new interface models were constructed which included intermolecular interactions between dyes. The agreement between theory and experiment was greatly improved, particularly for a configuration where N3 formed H-bonded dimers on the surface.

The idea that intermolecular interactions may play an important role in the DSC deserves further consideration. The COOH groups in N3 are generally acknowledged to bind the molecule to the substrate, but the calculations here show that they can also stabilise adsorption by forming H-bonds between molecules. A sensible next step would be to understand whether H-bonded configurations remain stable in the presence of a liquid electrolyte. Furthermore it would be interesting to consider how the formation of supramolecular assemblies might affect the charge injection process at the interface.

9.3 Valence PES and electronic structure

Instead of focusing on the core electrons one can use PES to probe the frontier orbitals of molecules or the valence band edge of semiconductors. The energy-level alignment at the interface has a direct bearing on the performance of a solar cell through the open-circuit voltage. In terms of electronic structure research, TiO_2 is relatively novel, and its excited-state properties have only been investigated in the last few years. In particular, the presence of Ti $3d$ states in the conduction band raise the question of whether standard local-density/generalised gradient approximations to exchange-correlation are a good starting point for the perturbative GW method. Here it has been shown that introducing a Hubbard U parameter into the initial calculation reduces the GW band gap from 3.7 to 3.3 eV. Meanwhile the HOMO-LUMO gap of the N3 molecule was found to be 3.4 eV, almost 3 eV larger than that calculated in DFT.

Calculating the energy-level alignment of the N3/TiO_2 system is an immense computational challenge due to the size of the interface model. The alignment calculated in standard DFT is qualitatively incorrect. However, employing the approach to calculating the energy-levels presented in this thesis recovers agreement between theory and experiment. The calculations demonstrate the interplay of quasiparticle corrections, image charge/charge transfer effects, configurational disorder and thermal broadening at the interface.

An obvious future project would be to take the general alignment approach demonstrated for N3 and apply it to new sensitizers, facilitating comparison of the electronic properties of different molecules. In particular one could consider organic dyes or semiconductor sensitizers. An equally interesting direction would be to further investigate the thermal effects at these interfaces. The finite tem-

perature MD gave rise to a substantial broadening of energy levels; it is not clear whether all molecules would display the same behaviour. Of course there is also the question of how the energy-level alignment might be affected when neighbouring dye molecules interact on the surface.

9.4 Beyond dye-sensitized solar cells

The experience in modelling the anatase TiO_2 surface extends to other systems of practical interest to photovoltaics. In particular, applying the technique of calculating core-level binding energies demonstrates interesting results both for water and bi-isonicotinic acid (BINA) adsorption. In the case of H_2O, adsorption energy calculations support the idea that the molecules remain intact on the anatase surface. Yet comparison of calculated and experimental core-level spectra strongly indicates the presence of OH groups, produced upon H_2O dissociation. The question remains as to whether the discrepancy is due to a shortcoming of the model interface (e.g. by not including defects) or a more fundamental problem of the theory. For BINA, structural calculations find that the "standard" model of the interface with TiO_2 features an elongated Ti–O bond. Intuition might yield the expectation that such a bond would produce an anomalous signal in the core-level spectra, but no such signal is observed experimentally. In fact, calculating the spectrum for that interface model also does not show any feature from the elongated bond. An additional discovery was the existence of a lower-energy interface model which forms H-bonds with a surface hydroxyl and also has a core-level spectrum consistent with experiment.

Returning to practical photovoltaics, one can consider replacing dye molecules with semiconductor sensitizers like stibnite (Sb_2S_3), bismuthinite (Bi_2S_3) or anti-

monselite (Sb_2Se_3). Similar in concept to DSCs, as a technology semiconductor-sensitized solar cells (SSCs) are in their infancy by comparison, with much less spectroscopic data available in the literature. Here first-principles calculations can assume a different role to suggest useful directions for experimentalists. A simplified scheme to calculate energy-level alignments at these interfaces identified antimonselite as a potentially viable sensitizer in new SSCs, while excluding bismuthinite. Here, it would be interesting to calculate the alignments using a more sophisticated method. Furthermore, the inclusion of the hole-transporting P3HT (which also acts as a light absorber) would be a challenging and ambitious step.

As computers continue to grow in power and theoretical methods in sophistication, it is not difficult to envisage higher accuracy, first-principles calculations of larger and larger systems. Yet no matter how beautiful a theory may seem, "Experiment is the sole judge of scientific truth" [261]. It is hoped that the ability of experiments and calculations to complement, challenge or surprise each other—as demonstrated in this thesis–will remain a sensible and durable philosophy in future research.

Bibliography

[1] Archer, D. *Global Warming—Understanding the Forecast* (John Wiley & Sons, 2007).

[2] Meinshausen, M. *et al. Nature* **458**, 1158 (2009).

[3] Peters, G. P. *et al. Nature Clim. Change* **3**, 4 (2013).

[4] *UK Energy in Brief 2012.* Published by the Office for National Statistics and the Department for Energy and Climate Change. `www.decc.gov.uk/en/content/cms/statistics/publications/`.

[5] MacKay, D. J. C. *Sustainable Energy—without the hot air* (UIT, 2008).

[6] "Solar subsidies to be cut by half". Article in The Guardian, Oct. 2011.

[7] SunShot Initiative website `www1.eere.energy.gov/solar/sunshot/`.

[8] *SunShot Vision study.* Published by U.S. Department of Energy. `www1.eere.energy.gov/solar/sunshot/vision_study.html`.

[9] Editorial. *Nature* **490**, 5 (2012).

[10] Sze, S. M. & Ng, K. K. *Physics of semiconductor devices* (John Wiley & Sons, 2007).

[11] Green, M. A., Emery, K., Hishikawa, Y., Warta, W. & Dunlop, E. D. *Prog. Photovolt.: Res. Appl.* **21**, 1 (2012).

[12] Repins, I. *et al. Prog. Photovolt.: Res. Appl.* **16**, 235 (2008).

[13] Nelson, J. The physics of solar cells (2003).

[14] Brabec, C. J., Sariciftci, N. S. & Hummelen, J. C. *Adv. Funct. Mater.* **11**, 15 (2001).

[15] O'Regan, B. & Grätzel, M. *Nature* **353**, 737 (1991).

[16] Kamat, P. V., Tvrdy, K., Baker, D. R. & Radich, J. G. *Chem. Rev.* **110**, 6664 (2010).

[17] Mora-Seró, I. & Bisquert, J. *J. Phys. Chem. Lett.* **1**, 3046 (2010).

[18] Huynh, W. U., Dittmer, J. J. & Alivisatos, A. P. *Science* **295**, 2425 (2002).

[19] Snaith, H. J. *Nature Photon.* **6**, 337 (2012).

[20] Osterwald, C. R. Standards, calibration, and testing of PV modules and solar cells. In *Practical Handbook of Photovoltaics* (Academic Press, 2012), second edn.

[21] Hagfeldt, A., Boschloo, G., Sun, L., Kloo, L. & Pettersson, H. *Chem. Rev.* **110**, 6595 (2010).

[22] Baxter, J. B. *J. Vac. Sci. Technol., A* **30**, 020801 (2012).

[23] Krebs, F. C., Gevorgyan, S. A. & Alstrup, J. *J. Mater. Chem.* **19**, 5442 (2009).

[24] Hardin, B. E., Snaith, H. J. & McGehee, M. D. *Nature Photon.* **6**, 162 (2012).

[25] Fujishima, A. & Honda, K. *Nature* **238**, 37 (1972).

[26] Deng, D., Kim, M. G., Lee, J. Y. & Cho, J. *Energy Environ. Sci.* **2**, 818 (2009).

[27] Yin, Z., Wu, L., Yang, H. & Su, Y. *Phys. Chem. Chem. Phys.* (2013). In press.

[28] Chen, X. & Mao, S. S. *Chem. Rev.* **107**, 2891 (2007).

[29] Tao, J., Luttrell, T. & Batzill, M. *Nature Chem.* **3**, 296 (2011).

[30] Feng, X. *et al. Nano Lett.* **8**, 3781 (2008).

[31] Tan, B. & Wu, Y. *J. Phys. Chem. B* **110**, 15932 (2006).

[32] Anta, J. A., Guillén, E. & Tena-Zaera, R. *J. Phys. Chem. C* **116**, 11413 (2012).

[33] Birkel, A. *et al. Energy Environ. Sci.* **5**, 5392 (2012).

[34] Memarian, N. *et al. Ang. Chem. Int. Ed.* **50**, 12321 (2011).

[35] Nazeeruddin, M. K. *et al. Inorg. Chem.* **38**, 6298 (1999).

[36] Nazeeruddin, M. K. *et al. J. Am. Chem. Soc.* **115**, 6382 (1993).

[37] Nazeeruddin, M. K. *et al. J. Am. Chem. Soc.* **123**, 1613 (2001).

[38] Calogero, G. *et al. Energy Environ. Sci.* **2**, 1162 (2009).

[39] Yella, A. *et al. Science* **334**, 629 (2011).

[40] Snaith, H. J. & Schmidt-Mende, L. *Adv. Mater.* **19**, 3187 (2007).

[41] Papageorgiou, N. *et al. J. Electrochem. Soc.* **143**, 3099 (1996).

[42] Yum, J.-H., Chen, P., Grätzel, M. & Nazeeruddin, M. K. *ChemSusChem* **1**, 699 (2008).

[43] Bach, U. *et al. Nature* **395**, 583 (1998).

[44] Tennakone, K., Kumara, G. R. R. A., Kottegoda, I. R. M., Wijayantha, K. G. U. & Perera, V. P. S. *J. Phys. D: Appl. Phys.* **31**, 1492 (1998).

[45] Nazeeruddin, M. K. *et al. J. Am. Chem. Soc.* **127**, 16835 (2005).

[46] Hüfner, S. *Photoelectron Spectroscopy* (Springer, 1996), second edn.

[47] Johansson, E. M. J., Hedlund, M., Siegbahn, H. & Rensmo, H. *J. Phys. Chem. B* **109**, 22256 (2005).

[48] Hahlin, M., Johansson, E. M. J., Schölin, R., Siegbahn, H. & Rensmo, H. *J. Phys. Chem. C* **115**, 11996 (2011).

[49] Mayor, L. C. *et al. J. Chem. Phys.* **129**, 114701 (2008).

[50] Hohenberg, P. & Kohn, W. *Phys. Rev.* **136**, B864 (1964).

[51] Kohn, W. & Sham, L. J. *Phys. Rev.* **140**, A1133 (1965).

[52] Ceperley, D. M. & Alder, B. J. *Phys. Rev. Lett.* **45**, 566 (1980).

[53] Perdew, J. P. & Zunger, A. *Phys. Rev. B* **23**, 5048 (1981).

[54] Perdew, J. P., Burke, K. & Ernzerhof, M. *Phys. Rev. Lett.* **77**, 3865 (1996).

[55] Perdew, J. P. *et al. Phys. Rev. B* **46**, 6671 (1992).

[56] Becke, A. D. *Phys. Rev. A* **38**, 3098 (1988).

[57] Lee, C., Yang, W. & Parr, R. G. *Phys. Rev. B* **37**, 785 (1988).

[58] Lundqvist, S. & March, N. H. *Theory of the Inhomogeneous Electron Gas* (Plenum Press, 1983).

[59] Gunnarsson, O. & Lundqvist, B. I. *Phys. Rev. B* **13**, 4274 (1976).

[60] Hamann, D. R., Schlüter, M. & Chiang, C. *Phys. Rev. Lett.* **43**, 1494 (1979).

[61] Hamann, D. R. *Phys. Rev. B* **40**, 2980 (1989).

[62] Troullier, N. & Martins, J. L. *Phys. Rev. B* **43**, 1993 (1991).

[63] Kleinman, L. & Bylander, D. M. *Phys. Rev. Lett.* **48**, 1425 (1982).

[64] Fuchs, M. & Scheffler, M. *Comput. Phys. Commun.* **119**, 67 (1999).

[65] Vanderbilt, D. *Phys. Rev. B* **41**, 7892 (1990).

[66] Laasonen, K., Pasquarello, A., Car, R., Lee, C. & Vanderbilt, D. *Phys. Rev. B* **47**, 10142 (1993).

[67] Ihm, J., Zunger, A. & Cohen, M. L. *J. Phys. C: Solid State* **12**, 4409 (1979).

[68] G. Makov, G. & Payne, M. C. *Phys. Rev. B* **51**, 4014 (1995).

[69] Martyna, G. J. & Tuckerman, M. E. *J. Chem. Phys.* **110**, 2810 (1999).

[70] Ismail Beigi, S. *Phys. Rev. B* **73**, 233103 (2006).

[71] Bengtsson, L. *Phys. Rev. B* **59**, 12301 (1999).

[72] Martin, R. M. *Electronic Structure* (Cambridge University Press, 2004).

[73] Frenkel, D. & Smit, B. *Understanding molecular simulation : from algorithms to applications* (Academic Press, 2002), second edn.

[74] Car, R. & Parrinello, M. *Phys. Rev. Lett.* **55**, 2471 (1985).

[75] Pastore, G., Smargiassi, E. & Buda, F. *Phys. Rev. A* **44**, 6334 (1991).

[76] Tangney, P. *J. Chem. Phys.* **124**, 044111 (2006).

[77] Blundell, S. J. & Blundell, K. M. *Concepts in Thermal Physics* (Oxford University Press, 2006).

[78] Andersen, H. C. *J. Chem. Phys.* **72**, 2384 (1980).

[79] Nosé, S. *J. Chem. Phys.* **81**, 511 (1984).

[80] Hoover, W. G. *Phys. Rev. A* **31**, 1695 (1985).

[81] Anisimov, V. I., Aryasetiawan, F. & Lichtenstein, A. I. *J. Phys. Condens. Matter* **9**, 767 (1997).

[82] Cramer, C. J. & Truhlar, D. G. *Phys. Chem. Chem. Phys.* **11**, 10757 (2009).

[83] Terakura, K., Oguchi, T., Williams, A. R. & Kübler, J. *Phys. Rev. B* **30**, 4734 (1984).

[84] Anisimov, V. I., Zaanen, J. & Andersen, O. K. *Phys. Rev. B* **44**, 943 (1991).

[85] Cococcioni, M. & De Gironcoli, S. *Phys. Rev. B* **71**, 035105 (2005).

[86] Jiang, H., Gomez-Abal, R. I., Rinke, P. & Scheffler, M. *Phys. Rev. B* **82**, 045108 (2010).

[87] Liechtenstein, A. I., Anisimov, V. I. & Zaanen, J. *Phys. Rev. B* **52**, R5467 (1995).

[88] Dudarev, S. L., Botton, G. A., Savrasov, S. Y., Humphreys, C. J. & Sutton, A. P. *Phys. Rev. B* **57**, 1505 (1998).

[89] Jones, R. O. & Gunnarsson, O. *Rev. Mod. Phys.* **61**, 689 (1989).

[90] Schaffry, M. *et al. Phys. Rev. Lett.* **104**, 200501 (2010).

[91] Blase, X., Attaccalite, C. & Olevano, V. *Phys. Rev. B* **83**, 115103 (2011).

[92] Rostgaard, C., Jacobsen, K. W. & Thygesen, K. S. *Phys. Rev. B* **81**, 085103 (2010).

[93] Gavnholt, J., Olsen, T., Engelund, M. & Schiøtz, J. *Phys. Rev. B* **78**, 075441 (2008).

[94] Hedin, L. & Johansson, A. *J. Phys. B: At. Mol. Phys.* **2**, 1336 (1969).

[95] Pehlke, E. & Scheffler, M. *Phys. Rev. Lett.* **71**, 2338 (1993).

[96] Pasquarello, A., Hybertsen, M. S. & Car, R. *Phys. Rev. B* **53**, 10942 (1996).

[97] Jolly, W. L., Bomben, K. D. & Eyermann, C. J. *At. Data Nucl. Data Tables* **31**, 433 (1984).

[98] McQuaide, B. H. & Banna, M. *Can. J. Chem.* **66**, 1919 (1988).

[99] Binder, J. F., Broqvist, P., Komsa, H.-P. & Pasquarello, A. *Phys. Rev. B* **85**, 245305 (2012).

[100] Janak, J. F. *Phys. Rev. B* **18**, 7165 (1978).

[101] Perdew, J. P. & Levy, M. *Phys. Rev. Lett.* **51**, 1884 (1983).

[102] Sham, L. J. & Schlüter, M. *Phys. Rev. Lett.* **51**, 1888 (1983).

[103] Godby, R. W., Schlüter, M. & Sham, L. J. *Phys. Rev. Lett.* **56**, 2415 (1986).

[104] Öğüt, S., Chelikowsky, J. & Louie, S. G. *Phys. Rev. Lett.* **79**, 1770 (1997).

[105] Godby, R. W. & White, I. D. *Phys. Rev. Lett.* **80**, 3161 (1998).

[106] Bruus, H. & Flensberg, K. *Many-Body Quantum Theory in Condensed Matter Physics* (Oxford University Press, 2004).

[107] Inkson, J. C. *Many-body Theory of Solids, An Introduction* (Plenum Press, 1983).

[108] Mahan, G. D. *Many-Particle Physics* (Springer, 2000).

[109] Hedin, L. & Lundqvist, S. vol. 23 of *Solid State Physics*, 1 (Academic Press, 1970).

[110] Aulbur, W. G., Jönsson, L. & Wilkins, J. W. vol. 54 of *Solid State Physics*, 1 (Academic Press, 1999).

[111] Onida, G., Reining, L. & Rubio, A. *Rev. Mod. Phys.* **74**, 601 (2002).

[112] Aryasetiawan, F. & Gunnarsson, O. *Rep. Prog. Phys.* **61**, 237 (1998).

[113] Hedin, L. *J. Phys. Condens. Matter* **11**, R489 (1999).

[114] Martin-Samos, L. & Bussi, G. *Comput. Phys. Commun.* **180**, 1416 (2009).

[115] Freysoldt, C. *et al. Comput. Phys. Commun.* **176**, 1 (2007).

[116] Adolph, B., Gavrilenko, V. I., Tenelsen, K., Bechstedt, F. & Del Sole, R. *Phys. Rev. B* **53**, 9797 (1996).

[117] Hedin, L. *Phys. Rev.* **139**, A796 (1965).

[118] Hybertsen, M. S. & Louie, S. G. *Phys. Rev. B* **34**, 5390 (1986).

[119] Farid, B., Daling, R., Lenstra, D. & van Haeringen, W. *Phys. Rev. B* **38**, 7530 (1988).

[120] Jin, Y.-G. & Chang, K. J. *Phys. Rev. B* **59**, 14841 (1999).

[121] Giustino, F., Cohen, M. L. & Louie, S. G. *Phys. Rev. B* **81**, 115105 (2010).

[122] Lebègue, S., Arnaud, B., Alouani, M. & Bloechl, P. E. *Phys. Rev. B* **67**, 155208 (2003).

[123] Rojas, H. N., Godby, R. W. & Needs, R. J. *Phys. Rev. Lett.* **74**, 1827 (1995).

[124] von der Linden, W. & Horsch, P. *Phys. Rev. B* **37**, 8351 (1988).

[125] Godby, R. W. & Needs, R. J. *Phys. Rev. Lett.* **62**, 1169 (1989).

[126] Stankovski, M. *et al. Phys. Rev. B* **84**, 241201 (2011).

[127] Shih, B.-C., Xue, Y., Zhang, P., Cohen, M. L. & Louie, S. G. *Phys. Rev. Lett.* **105**, 146401 (2010).

[128] Umari, P., Stenuit, G. & Baroni, S. *Phys. Rev. B* **81**, 115104 (2010).

[129] Berger, J. A., Reining, L. & Sottile, F. *Phys. Rev. B* **85**, 085126 (2012).

[130] Nguyen, H.-V., Pham, T. A., Rocca, D. & Galli, G. *Phys. Rev. B* **85**, 081101 (2012).

[131] Hübener, H., Pérez-Osorio, M. A., Ordejón, P. & Giustino, F. *Eur. Phys. J. B* **85**, 1 (2012).

[132] Rehr, J. J. *Phys. Scripta* **2005**, 19 (2005).

[133] Bardyszewski, W. & Hedin, L. *Phys. Scripta* **32**, 439 (1985).

[134] Guzzo, M. *et al. Eur. Phys. J. B* **85**, 1 (2012).

[135] Kheifets, A. S., Sashin, V. A., Vos, M., Weigold, E. & Aryasetiawan, F. *Phys. Rev. B* **68**, 233205 (2003).

[136] Patrick, C. E. & Giustino, F. *Phys. Rev. B* **84**, 085330 (2011).

[137] Muscat, J., Swamy, V. & Harrison, N. M. *Phys. Rev. B* **65**, 224112 (2002).

[138] Diebold, U. *Surf. Sci. Rep.* **48**, 53 (2003).

[139] Horn, M., Schwerdtfeger, C. F. & Meagher, E. P. *Z. Kristallogr.* **136**, 273 (1972).

[140] Abrahams, S. C. & Bernstein, J. L. *J. Chem. Phys.* **55**, 3206 (1971).

[141] Giannozzi, P. *et al. J. Phys. Condens. Matter* **21**, 395502 (2009).

[142] Lazzeri, M., Vittadini, A. & Selloni, A. *Phys. Rev. B* **63**, 155409 (2001).

[143] Zoroddu, A., Bernardini, F., Ruggerone, P. & Fiorentini, V. *Phys. Rev. B* **64**, 045208 (2001).

[144] Persson, P. & Lundqvist, M. J. *J. Phys. Chem. B* **109**, 11918 (2005).

[145] Schiffmann, F. *et al. J. Phys. Chem. C* **114**, 8398 (2010).

[146] Vittadini, A., Selloni, A., Rotzinger, F. P. & Grätzel, M. *Phys. Rev. Lett.* **81**, 2954 (1998).

[147] Vittadini, A., Selloni, A., Rotzinger, F. P. & Grätzel, M. *J. Phys. Chem. B* **104**, 1300 (2000).

[148] De Angelis, F., Fantacci, S., Selloni, A., Grätzel, M. & Nazeeruddin, M. K. *Nano Lett.* **7**, 3189 (2007).

[149] De Angelis, F., Fantacci, S., Selloni, A., Nazeeruddin, M. K. & Grätzel, M. *J. Phys. Chem. C* **114**, 6054 (2010).

[150] Jones, D. R. & Troisi, A. *Phys. Chem. Chem. Phys.* **12**, 4625 (2010).

[151] Maggio, E., Martsinovich, N. & Troisi, A. *J. Phys. Chem. C* **116**, 7638 (2012).

[152] Jakubikova, E., Snoeberger III, R. C., Batista, V. S., Martin, R. L. & Batista, E. R. *J. Phys. Chem. A* **113**, 12532 (2009).

[153] Shklover, V. *et al. Chem. Mater.* **9**, 430 (1997).

[154] Noguera, C. *Physics and chemistry at oxide surfaces* (Cambridge University Press, 1996).

[155] Shklover, V., Ovchinnikov, Y. E., Braginsky, L. S., Zakeeruddin, S. M. & Grätzel, M. *Chem. Mater.* **10**, 2533 (1998).

[156] Rensmo, H. *et al. J. Chem. Phys.* **111**, 2744 (1999).

[157] Nazeeruddin, M. K., Humphry-Baker, R., Liska, P. & Grätzel, M. *J. Phys. Chem. B* **107**, 8981 (2003).

[158] Lee, K. E., Gomez, M. A., Elouatik, S. & Demopoulos, G. P. *Langmuir* **26**, 9575 (2010).

[159] Schnadt, J. *et al. J. Phys. Chem. B* **108**, 3114 (2004).

[160] Islam, M. M., Calatayud, M. & Pacchioni, G. *J. Phys. Chem. C* **115**, 6809 (2011).

[161] Ikeda, M. *et al. J. Photoch. Photobio. A* **202**, 185 (2009).

[162] Sasahara, A., Fujio, K., Koide, N., Han, L. & Onishi, H. *Surf. Sci* **604**, 106 (2010).

[163] Meyer, T. J. *et al. Inorg. Chem.* **33**, 3952 (1994).

[164] Murakoshi, K. *et al. J. Electroanal. Chem.* **396**, 27 (1995).

[165] Finnie, K. S., Bartlett, J. R. & Woolfrey, J. L. *Langmuir* **14**, 2744 (1998).

[166] Anselmi, C., Mosconi, E., Pastore, M., Ronca, E. & De Angelis, F. *Phys. Chem. Chem. Phys.* **14**, 15963 (2012).

[167] Westermark, K. *et al. J. Phys. Chem. B* **106**, 10102 (2002).

[168] Patrocinio, A. O. T., Paniago, E. B., Paniago, R. M. & Murakami Iha, N. Y. *Appl. Surf. Sci.* **254**, 1874 (2008).

[169] Shimada, K. In Hüfner, S. (ed.) *Very High Resolution Photoelectron Spectroscopy* (Springer, Berlin Heidelberg, 2007).

[170] Joyner, R. W. & Roberts, M. W. *P. Roy. Soc. Lond. A Mat.* **350**, 107 (1976).

[171] Aplincourt, P., Bureau, C., Anthoine, J. & Chong, D. P. *J. Phys. Chem. A* **105**, 7364 (2001).

[172] Tsuzuki, S. & Lüthi, H. P. *J. Chem. Phys.* **114**, 3949 (2001).

[173] Dulub, O. & Diebold, U. *J. Phys. Condens. Matter* **22**, 084014 (2010).

[174] Rauschenbach, S. *et al. ACS Nano* **3**, 2901 (2009).

[175] Wenger, B., Grätzel, M. & Moser, J.-E. *J. Am. Chem. Soc.* **127**, 12150 (2005).

[176] Patrick, C. E. & Giustino, F. *J. Phys. Condens. Matter* **24**, 202201 (2012).

[177] Asahi, R., Taga, Y., Mannstadt, W. & Freeman, A. J. *Phys. Rev. B* **61**, 7459 (2000).

[178] Bertel, E., Stockbauer, R. & Madey, T. E. *Surf. Sci* **141**, 355 (1984).

[179] Kang, W. & Hybertsen, M. S. *Phys. Rev. B* **82**, 085203 (2010).

[180] Chiodo, L. *et al. Phys. Rev. B* **82**, 045207 (2010).

[181] Mowbray, D. J., Martinez, J. I., Lastra, J. M. G., Thygesen, K. S. & Jacobsen, K. W. *J. Phys. Chem. C* **113**, 12301 (2009).

[182] Landmann, M., Rauls, E. & Schmidt, W. G. *J. Phys. Condens. Matter* **24**, 195503 (2012).

[183] Thulin, L. & Guerra, J. *Phys. Rev. B* **77**, 195112 (2008).

[184] Kavan, L., Grätzel, M., Gilbert, S. E., Klemenz, C. & Scheel, H. J. *J. Am. Chem. Soc.* **118**, 6716 (1996).

[185] Giustino, F., Louie, S. G. & Cohen, M. L. *Phys. Rev. Lett.* **105**, 265501 (2010).

[186] Cannuccia, E. & Marini, A. *Eur. Phys. J. B* **85**, 1 (2012).

[187] Nolan, M. *et al. Phys. Rev. B* **77**, 235424 (2008).

[188] Kioupakis, E., Zhang, P., Cohen, M. L. & Louie, S. G. *Phys. Rev. B* **77**, 155114 (2008).

[189] Arroyo-de Dompablo, M. E., Morales-García, A. & Taravillo, M. *J. Chem. Phys.* **135**, 054503 (2011).

[190] Tezuka, Y. *et al. J. Phys. Soc. Jpn.* **63**, 347 (1994).

[191] Fantacci, S., De Angelis, F. & Selloni, A. *J. Am. Chem. Soc.* **125**, 4381 (2003).

[192] Theisen, J.-P. *Electronic energy level alignment of dye molecules on TiO_2 and ZnO surfaces for photovoltaic applications.* Master's thesis, Rutgers, The State University of New Jersey (2008).

[193] Isseroff, L. Y. & Carter, E. A. *Phys. Rev. B* **85**, 235142 (2012).

[194] van Schilfgaarde, M., Kotani, T. & Faleev, S. *Phys. Rev. Lett.* **96**, 226402 (2006).

[195] Caruso, F., Rinke, P., Ren, X., Scheffler, M. & Rubio, A. *Phys. Rev. B* **86**, 081102 (2012).

[196] Patrick, C. E. & Giustino, F. *Phys. Rev. Lett.* **109**, 116801 (2012).

[197] Schwanitz, K., Weiler, U., Hunger, R., T, M. & Jaegermann, W. *J. Phys. Chem. C* **111**, 849 (2007).

[198] Westermark, K. *et al. Chem. Phys.* **285**, 157 (2002).

[199] Hagfeldt, A. & Grätzel, M. *Accounts Chem. Res.* **33**, 269 (2000).

[200] Rensmo, H. *et al. Chem. Phys. Lett.* **274**, 51 (1997).

[201] Neaton, J. B., Hybertsen, M. S. & Louie, S. G. *Phys. Rev. Lett.* **97**, 216405 (2006).

[202] Marom, N., Moussa, J. E., Ren, X., Tkatchenko, A. & Chelikowsky, J. R. *Phys. Rev. B* **84**, 245115 (2011).

[203] Martsinovich, N. & Troisi, A. *Energy Environ. Sci.* **4**, 4473 (2011).

[204] Kanai, Y., Wu, Z. & Grossman, J. C. *J. Mater. Chem.* **20**, 1053 (2010).

[205] Van de Walle, C. G. & Martin, R. M. *Phys. Rev. B* **35**, 8154 (1987).

[206] Garcia-Lastra, J. M., Rostgaard, C., Rubio, A. & Thygesen, K. S. *Phys. Rev. B* **80**, 245427 (2009).

[207] Lundqvist, M. J., Nilsing, M., Persson, P. & Lunell, S. *Int. J. Quantum Chem.* **106**, 3214 (2006).

[208] Chiodo, L. *et al. J. Chem. Phys.* **135**, 244704 (2011).

[209] Alkauskas, A., Broqvist, P., Devynck, F. & Pasquarello, A. *Phys. Rev. Lett.* **101**, 106802 (2008).

[210] Gonze, X., Boulanger, P. & Côté, M. *Ann. Phys. (Berlin)* **523**, 168 (2011).

[211] Greiner, M. T. *et al. Nature Mater.* **11**, 76 (2012).

[212] Stojić, N., Dal Corso, A., Zhou, B. & Baroni, S. *Phys. Rev. B* **77**, 195116 (2008).

[213] Husser, H., van Heys, J. & Pehlke, E. *Phys. Rev. B* **84**, 235135 (2011).

[214] He, Y., Tilocca, A., Dulub, O., Selloni, A. & Diebold, U. *Nature Mater.* **8**, 585 (2009).

[215] Tilocca, A. & Selloni, A. *Langmuir* **20**, 8379 (2004).

[216] Herman, G. S., Dohnálek, Z., Ruzycki, N. & Diebold, U. *J. Phys. Chem. B* **107**, 2788 (2003).

[217] Walle, L. E. *et al. J. Phys. Chem. C* **115**, 9545 (2011).

[218] Duncan, D. A., Allegretti, F. & Woodruff, D. P. *Phys. Rev. B* **86**, 045411 (2012).

[219] Walle, L. E., Borg, A., Uvdal, P. & Sandell, A. *Phys. Rev. B* **80**, 235436 (2009).

[220] Tilocca, A. & Selloni, A. *J. Chem. Phys.* **119**, 7445 (2003).

[221] Aschauer, U. *et al. J. Phys. Chem. C* **114**, 1278 (2010).

[222] Zhao, Z., Li, Z. & Zou, Z. *J. Phys. Chem. C* **116**, 11054 (2012).

[223] Patthey, L. *et al. J. Chem. Phys.* **110**, 5913 (1999).

[224] Thomas, A. *et al. Surf. Sci* **592**, 159 (2005).

[225] Persson, P. & Lunell, S. *Sol. Energ. Mat. Sol. C.* **63**, 139 (2000).

[226] Labat, F. & Adamo, C. *J. Phys. Chem. C* **111**, 15034 (2007).

[227] Patrick, C. E. & Giustino, F. *Adv. Func. Mater.* **21**, 4663 (2011).

[228] Snaith, H. J. *Adv. Funct. Mater.* **20**, 13 (2010).

[229] Horiuchi, T., Miura, H., Sumioka, K. & Uchida, S. *J. Am. Chem. Soc.* **126**, 12218 (2004).

[230] Kim, S. *et al. J. Am. Chem. Soc.* **128**, 16701 (2006).

[231] Hagberg, D. P. *et al. Chem. Commun.* 2245 (2006).

[232] Lee, Y.-L., Huang, B.-M. & Chien, H.-T. *Chem. Mater.* **20**, 6903 (2008).

[233] Niitsoo, O. *et al. J. Photoch. Photobio. A* **181**, 306 (2006).

[234] Salant, A. *et al. ACS Nano* **4**, 5962 (2010).

[235] Gao, J. *et al. Nano Lett.* **11**, 1002 (2011).

[236] Chang, J. A. *et al. Nano Lett.* **10**, 2609 (2010).

[237] Itzhaik, Y., Niitsoo, O., Page, M. & Hodes, G. *J. Phys. Chem. C* **113**, 4254 (2009).

[238] Black, J., Conwell, E. M., Seigle, L. & Spencer, C. W. *J. Phys. Chem. Solids* **2**, 240 (1957).

[239] Versavel, M. Y. & Haber, J. A. *Thin Solid Films* **515**, 7171 (2007).

[240] Caracas, R. & Gonze, X. *Phys. Chem. Miner.* **32**, 295 (2005).

[241] Ben Nasr, T., Maghraoui-Meherzi, H., Abdallah, H. B. & Bennaceur, R. *Physica B* **406**, 287 (2011).

[242] Koc, H., Mamedov, A. M., Deligoz, E. & Ozisik, H. *Solid State Sciences* **14**, 1211 (2012).

[243] Vadapoo, R., Krishnan, S., Yilmaz, H. & Marin, C. *Nanotechnology* **22**, 175705 (2011).

[244] Lundegaard, L. F., Miletich, R., Balic-Zunic, T. & Makovicky, E. *Phys. Chem. Miner.* **30**, 463 (2003).

[245] Filip, M. R., Patrick, C. E. & Giustino, F. *Phys. Rev. B* **87**, 205125 (2013).

[246] Mane, R. S., Sankapal, B. R. & Lokhande, C. D. *Thin Solid Films* **353**, 29 (1999).

[247] Zakaznova-Herzog, V. *et al. Surf. Sci.* **600**, 348 (2006).

[248] Gerber, I. C. & Ángyán, J. G. *J. Chem. Phys.* **126**, 044103 (2007).

[249] Snook, J. H., Samuelson, L. A., Kumar, J., Kim, Y.-G. & Whitten, J. E. *Org. Electron.* **6**, 55 (2005).

[250] Duncan, W. R. & Prezhdo, O. V. *Annu. Rev. Phys. Chem.* **58**, 143 (2007).

[251] Nitzan, A. *Chemical dynamics in condensed phases* (Oxford University Press, 2006), first edn.

[252] Zhang, H. *et al. Nature Phys.* **5**, 438 (2009).

[253] Peter, L. M., Wijayantha, K. G. U., Riley, D. J. & Waggett, J. P. *J. Phys. Chem. B* **107**, 8378 (2003).

[254] Guijarro, N. *et al. J. Phys. Chem. Lett.* **3**, 1351 (2012).

[255] Lutz, T. *et al. Phys. Chem. Chem. Phys.* **14**, 16192 (2012).

[256] Shockley, W. & Queisser, H. J. *J. Appl. Phys.* **32**, 510 (1961).

[257] Barea, E. M. *et al. J. Am. Chem. Soc.* **132**, 6834 (2010).

[258] González-Pedro, V., Xu, X., Mora-Seró, I. & Bisquert, J. *ACS Nano* **4**, 5783 (2010).

[259] Mehta, R. J. *et al. Nano Lett.* **10**, 4417 (2010).

[260] Noori, K. & Giustino, F. *Adv. Func. Mater.* **22**, 5089 (2012).

[261] Feynman, R. P. *The Feynman lectures in physics, vol. 1*, chap. 1 (Addison-Wesley, 1964).

Acknowledgements

My foremost thanks go to my supervisor, Feliciano Giustino. Throughout the years spent performing this research he has been a constant source of ideas, enthusiasm and general good sense. I have benefited massively from his generosity with his time, attention to detail and patience in explaining both new and old physics. Above all he has encouraged me not to be afraid to try new ideas and ask new questions.

In day-to-day work I particularly thank my office-mates Harry, Henry, Keian and Tim, who have livened up the days no end, whether through Friday afternoon "Only Connect" or a robust exchange of ideas concerning the air conditioning. I have also enjoyed many conversations with our genial office neighbour Hannes and with Marina, whose constant, friendly enthusiasm is always appreciated! I am grateful for advice received from Ben, Dan and Jonathan over the course of my DPhil, and also for the efforts of Paul in managing the clusters.

It has been a great privilege to have lived and worked for eight years in Oxford. What my undergraduate college St. Anne's lacks in architectural splendour it makes up for with the friendliness of its members: my good friends Allan, Ed and John; my "college son" and daughter-in-law Johannes and Charlie; and my tutors, Pat Irwin and Neville Harnew, who have kept me involved in the college through teaching in my graduate years.

In the times when physics got a bit too much, I am lucky to have been able to turn to the many acronyms of music groups: OMO, SASJO, CSO, MSB, OSE... Special mention to Alex and Nat, the grumpy old SASJOnians David, David, Martin and Rob, my choir pal Anne and of course the lovely Harriet.

Thinking of my family, my brother Tom and very soon-to-be sister-in-law Jo have generously provided me with many perfect escapes from Oxford through excursions to visit them, whether involving good food, cricket matches or wine-tasting. Thanks!

Finally I thank my parents for their remarkable, generous and unswerving support. They have shared the highs and lows of my time here, and have always been on the end of the phone to offer patient, honest and sensible advice, or to simply listen. Without a doubt their help and guidance has got me through these eight years, and for that I am extremely grateful.

List of papers

[1] C. E. Patrick and F. Giustino, *O 1s core-level shifts at the anatase TiO_2(101)/N3 photovoltaic interface: Signature of H-bonded supramolecular assembly*, Phys. Rev. B **84**, 085330 (2011).

[2] C. E. Patrick and F. Giustino, *Structural and Electronic Properties of Semiconductor-Sensitized Solar-Cell Interfaces*, Adv. Funct. Mater. **21**, 4663 (2011)

[3] C. E. Patrick and F. Giustino, *GW quasiparticle bandgaps of anatase TiO_2 starting from DFT+U*, J. Phys. Condens. Matter **24**, 202201 (2012)

[4] C. E. Patrick and F. Giustino, *Quantitative Analysis of Valence Photoemission Spectra and Quasiparticle Excitations at Chromophore-Semiconductor Interfaces*, Phys. Rev. Lett. **109**, 116801 (2012)